Hall measurement-based study of ferromagnetic thin films stimulated by the idea of spin-orbit torque

by

Mukesh Aryal
B.Sc., Tampere University, 2019

A Thesis Submitted in Partial Fulfillment of the
Requirements for the Degree of

MASTER OF SCIENCE

in the Department of Physics and Astronomy

We acknowledge and respect the Lək̓ʷəŋən peoples on whose territory the university stands, and the Songhees, Esquimalt and WSÁNEĆ peoples whose historical relationships with the land continue to this day.

Hall measurement-based study of ferromagnetic thin films stimulated by the idea of spin-orbit torque

by

Mukesh Aryal
B.Sc., Tampere University, 2019

Supervisory Committee

Dr. Byoung-Chul Choi, Supervisor
(Department of Physics and Astronomy)

Dr. Geoff Steeves, Departmental Member
(Department of Physics and Astronomy)

ABSTRACT

This study is motivated by the idea of spin-orbit torque (SOT). The research attempts to study SOT effects in ferromagnetic systems through numerical and experimental approaches. The numerical simulation segment employs an object-oriented framework tool (OOMMF) to model magnetic systems with a focus on understanding critical parameters. The first part of the simulation incorporates thermal effects into a nanometer-sized CoFeB Hall structure, revealing a significant reduction in critical parameters for magnetization switching due to the inclusion of thermal effects. Subsequently, a micrometer-sized CoFeB Hall structure is simulated, although with compromises in accuracy due to discretization changes and the exclusion of thermal effects. The simulations predict current amplitude requirements for magnetization reversal and highlight the transient nature of magnetization changes under a short current pulse. The experimental facet involves the fabrication and assessment of tungsten films for their viability in SOT applications. Employing sheet resistance measurements via Van der Pauw's 4-point method, tungsten films exhibit varying resistivity based on thickness, suggesting the presence of distinct phases. The investigation then shifts to the study of magnetization in fabricated Hall structures through current-based Hall measurement techniques. Initial attempts utilizing cobalt films uncover in-plane anisotropy, motivating a shift to the use of $Co_{20}Fe_{60}B_{20}$ films, a recognized ferromagnetic material in spintronics. Careful fabrication and annealing of CoFeB films appeared to improve film quality, yielding promising Hall signals; however, the expected out-of-plane anisotropy required for the targeted SOT experiment could not be achieved. Furthermore, attempts to measure SOT-induced effects encountered challenges, highlighting the need for superior film quality and a more sensitive measurement setup. Despite facing setbacks in detecting SOT-induced effects, the research includes a comparative study of Hall signals across different thicknesses in ferromagnetic devices. The study collectively contributes valuable insights into the complex interplay of spin-orbit torque effects, film quality, and magnetization characteristics within the realm of ferromagnetic systems. This work can serve as a reference for future endeavors in the exploration of spin-orbit torque-driven phenomena and their potential applications.

Contents

List of Tables

List of Figures

ACKNOWLEDGEMENTS

I would like to extend my sincere gratitude and appreciation to:

Dr. Byoung-Chul Choi, for his guidance, unwavering support, and supervision throughout this research journey. His insightful mentorship and guidance have been instrumental in shaping the direction of the project and the completion of the task.

Dr. Milton Wang, for his invaluable guidance in the intricate field of nanofabrication. His expertise and patient mentorship have been pivotal in the successful realization of experimental components of the research outcomes.

Nicolas Braam, for his technical expertise, generous assistance, and valuable suggestions that have greatly enriched the depth and breadth of this study. His willingness to share his knowledge and provide assistance at critical junctures has been indispensable.

Gratitude is a quality similar to electricity: it must be produced and discharged and used up in order to exist at all.
William Faulkner

Chapter 1

Theoretical Background

Electrons, as subatomic particles carrying an electric charge and a spin, are at the heart of modern electronics. The study of electric charge has had a profound effect on shaping the landscape of modern technological advancements. Many prevalent technologies are the products of electronics, which exploits the manipulation of electric charge component of electrons in materials. Traditionally, the field of electronics only dealt with one aspect of the properties of the electrons, i.e., charge; however, the fascinating spin property of the electrons has captured a lot of interest in the field of electronics lately. Spintronics, short for "spin transport electronics", is an emerging field that extends the principles of electronics by incorporating the spin property of electrons in devices.

Spintronics, a field at the intersection of quantum mechanics and electronics, has seen remarkable developments since its inception. The advancements in spintronics have the potential to revolutionize various technological sectors, from data storage to energy-efficient computing. Some key developments in spintronics include topics such as giant magnetoresistance (GMR), spin-transfer torque (STT), spin-orbit torque (SOT), topological insulators, and racetrack memory. Although all of the topics in spintronics appear equally fascinating, this thesis is stimulated by the idea of spin-orbit torque.

Our project aims to study the SOT effects in ferromagnetic/heavy metal bi-layers through the use of a Hall-based measurement technique. Some of the important concepts and principles encountered in our project are discussed in the following sections to familiarize ourselves with the topic at hand.

1.1 Introduction to Hall Effects

Spin-orbit torque and spin-transfer torque are the consequences of the effect of spin currents. Spin currents can best be understood by studying the underlying phenomena like the spin Hall effect (SHE) and the Rashba effect. The spin Hall effect belongs to a family of Hall effects which deals with the effect of magnetic fields when electric current flows through a thin strip. The family of Hall effects comprises ordinary Hall effect (OHE), anomalous Hall effect (AHE), and spin Hall effect. These Hall effects are discussed briefly in the following section before proceeding forward.

1.1.1 Ordinary Hall Effect

Edwin Hall discovered the ordinary Hall effect when doing an experiment on a non-magnetic metal strip [1]. When a non-magnetic metal strip was placed on a magnetic field perpendicular to the plane of the strip while applying an electric current longitudinally through the strip, he found an emergence of a transversal voltage difference across the strip. This potential difference, arising due to the Lorentz force experienced by the electrons flowing through the conductor, was later called the Hall voltage. The Hall voltage is directly proportional to the applied field and its relationship is given by [2][1]

$$\rho_H = \frac{V_H * d}{I} = R_H B, \tag{1.1}$$

where ρ_H is the Hall resistivity, V_H is the Hall voltage, R_H is the Hall coefficient, d is the thickness of the strip, and B is the magnitude of the applied magnetic field perpendicular to the plane of the strip. Schematic of the OHE is given in figure (1.1.1).

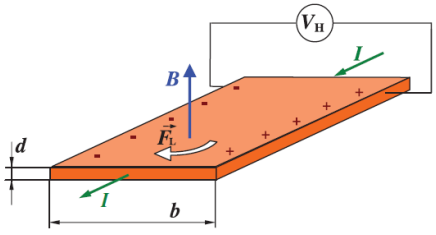

[2]

Figure 1.1.1: Schematics of the ordinary Hall effect.

In the figure (1.1.1), the negative charge can be seen accumulated to one side of the conductor when the electron experiences the Lorentz force due to the applied magnetic field. The presence of excess electrons on one side and the deficiency of electrons on the other side of the conductor creates a net potential difference across the conductor giving rise to a Hall voltage, which can be measured using a Voltmeter.

1.1.2 Anomalous Hall Effect

In ferromagnetic materials, the same kind of effect–as in the case of non-magnetic metal strips–can be observed without applying any external magnetic field. Since ferromagnetic materials consist of domains and have internal magnetization, a similar transversal voltage can be detected even without applying any external magnetic field. AHE experiments are usually performed to study the magnetization of the magnetic material; in such experiments, external field is used to influence the magnetization of the material. Empirically, the Hall resistivity in ferromagnetic materials can be written as [2][3]

$$\rho_{xy} = R_0 B + R_s \mu_0 M_z, \tag{1.2}$$

where, R_0 and R_s are the material-dependent coefficients of the normal and AHE contributions, and M_z is the out-of-plan magnetization component of the ferromagnetic material. Here the first term is proportional to the applied field, which corresponds to the OHE. On the other hand, the second term, pure anomalous Hall component, is proportional to the inherent magnetization of the material with a proportionality constant R_s, the anomalous Hall coefficient. Schematic of the AHE is given in figure (1.1.2).

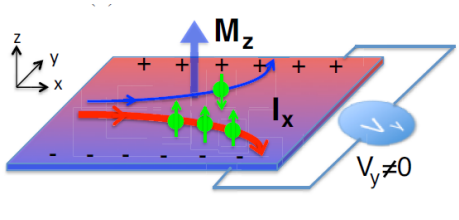

[4]

Figure 1.1.2: Schematics of the anomalous Hall effect.

In the figure(1.1.2), the unequal number of electrons scattered along the different directions, due to the presence of net magnetization in the strip, can be seen producing

a potential difference across the strip; this potential difference can be measured using a voltmeter that enables us to study the magnetization component of the strip. The AHE is a consequence of the spin-dependent transport. As electrons move through a ferromagnetic conductor, they gain a transverse velocity. Since electrons have two spin states, spin-up and spin-down, the traversal velocity of these spin states is opposite to each other due to spin-orbit interactions. As a result, spin-up electrons are pushed along one side of the material whereas spin-down electrons are pushed toward the other side. In a ferromagnetic material, the population of the majority spin electrons, sharing the direction of magnetization of the ferromagnet, is greater than that of minority spin electrons. This unequal number of spin-up and spin-down electrons causes more electrons to accumulate on one side of the ferromagnetic strip than on the other side. The unequal charge distribution along the traverse direction gives rise to a measurable potential difference, this voltage is called the anomalous Hall voltage.

1.1.3 Spin Hall Effect

The spin-dependent transverse velocity is present in every kind of conductor, whether magnetic or non-magnetic. In a non-magnetic material, there are an equal number of spin-up and spin-down electrons as there is no net magnetization present within the material. Even though there are the same number of spin-up and spin-down electrons, the spin-dependent transverse velocity still causes the two different spin states to accumulate on different sides of the conductor. The tendency for opposite spins to accumulate on different sides of the conductor, without developing a potential difference between the sides, is known as the spin Hall effect. It is a purely spin-based phenomenon, and it does not require the magnetic field to be applied to the conductor. A very simplified schematic of the SHE is shown in figure (1.1.3).

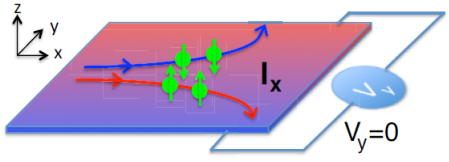

[4]

Figure 1.1.3: Simplified schematic of the spin Hall effect.

In the figure (1.1.3), electrons with different spin components can be seen to accumulate on opposite sides of a non-magnetic conductor when an electric current flows through it. Since the number of spin-up and spin-down electrons is the same in the

non-magnetic conductor, no potential difference is generated across the strip despite the accumulation of different spin-states. The segregation of different spin states in a conductor is the result of spin-orbit interactions which will be discussed in the sections to come.

1.2 Spin Current

The density of state (DOS) at the Fermi level of spin-up electrons $n_\uparrow$ and spin-down electrons $n_\downarrow$ in a nonmagnetic metal (NM) is equal; hence, the number of electrons as it passes through nonmagnetic metal has an equal number of spin-up and spin-down electrons. The same is not true in the case of ferromagnetic metal (FM). In FM, the DOS of majority-spin electrons—sharing the direction of magnetization ($\mathbf{M}$)—at the Fermi level is larger than the minority-spin electrons; consequently, the number of spin-up and spin-down electrons passing through FM is different. [1]

If a stack of NM/FM/NM layer is formed and an electric current is passed through it, an interesting phenomenon can be observed. As the minority-spin electrons arrive at the NM/FM interface of the stack, the smaller number of DOS at the fermi level of FM causes the electrons to either flip their spin to enter the more ample majority-spin DOS in the FM or they are reflected back from the interface. Upon reflection, minority-spin electrons accumulate along the interface of NM. Furthermore, the scattering rate of the minority-spin electrons inside the FM is greater than the majority-spin electrons. The scattering causes the minority-spin electrons to flip as they pass through the FM giving rise to a phenomenon known as the spin-filtering effect. Due to these effects, the electrons transmitting through an FM are principally major-spin electrons, parallel to the $\mathbf{M}$ of the FM. The spin polarization process described here is illustrated in figure (1.2.1).

In figure (1.2.1), near the FM/NM interface, the number of spin-up electrons is not equal to the number of spin-down electrons ($n_\uparrow \neq n_\downarrow$) within the spin diffusion length. In this type of arrangement, a concept of spin current vector is often used to explain the transport of spin angular momentum. The spin current vector is defined as

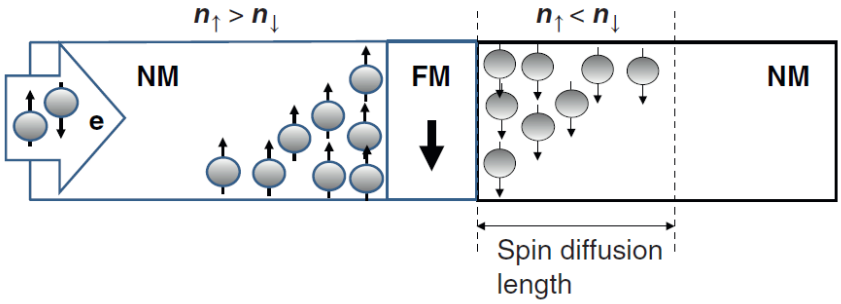

[1]

Figure 1.2.1: The accumulation of minority-spin electrons on the left and majority-spin electrons on the right of the FM layer in an NM/FM/NM stack when an electric current flows through the stack.

$$\mathbf{J^S} = \frac{\hbar}{2}\left(n_\uparrow v_\uparrow - n_\downarrow v_\downarrow\right) \tag{1.3}$$

where $v_\uparrow$ and $v_\downarrow$ are velocity of spin-up and spin-down electrons, respectively. The vector $\mathbf{J^S}$ can also be understood as the spin angular momentum current density and it corresponds to the flow of spin angular momentum carried by the conduction electrons.

The spin current can be divided into two groups: *spin polarized current* and *pure spin current*. A spin current generated when $n_\uparrow \neq n_\downarrow$ but $v_\uparrow$ and $v_\downarrow$ are along the same direction is categorized as spin-polarized current. On the contrary, spin current generated when $n_\uparrow = n_\downarrow$ but $v_\uparrow$ and $v_\downarrow$ are along different directions is categorized as pure spin current. The pure spin current does not require net charge flow and occurs as the result of pure spin separation, arising from the effect like SHE. Figure (1.2.2) shows the different types of spin currents.

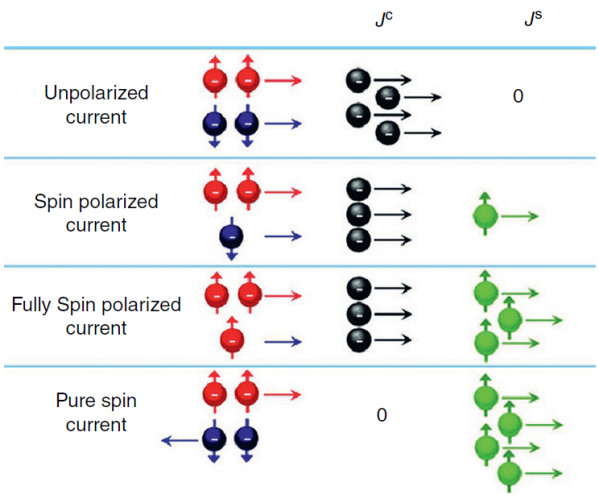

[1]

Figure 1.2.2: Different types of spin currents

1.3 Spin-Orbit Coupling

After developing some understanding about the spin currents, we can now try to understand an important interaction that causes it; the interaction of interest is spin-orbit coupling (SOC). Spin-orbit coupling is the interaction of the orbital angular momentum of the electron with its spin angular momentum. We can take a semi-classical approach and a very simple hydrogen-like model to develop an understanding of spin-orbit interactions. Classical electromagnetism tells us how electric and magnetic fields can transform from one reference frame to another when relativistic effects are considered. Keeping this in mind, we will consider a simple model of an electron moving around a positively charged nucleus. We will consider two different inertial reference frames to explain the interaction between the electron and the nucleus. Schematics of the motion of the electron in different frames are portrayed in figure (1.3.1).

The first reference frame is a lab frame where the nucleus is stationary and the electron is moving around the nucleus with a constant velocity $\mathbf{v}$ in a circular orbit under the influence of a radial electric field $\mathbf{E}$ emanating from the nucleus. The other reference frame is the one where we consider the electron to be at rest; in the rest frame of the electron, the electron sees a positive nucleus revolving around it. The electron, in its

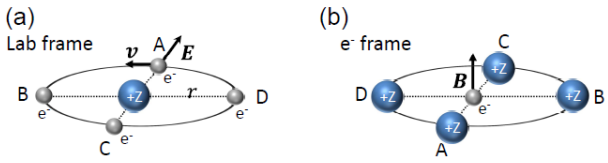

[5]

Figure 1.3.1: Schematics of the moving electron in **a)** the lab frame, and **b)** the rest frame of the electron. The figure shows four different instances (A, B, C, D) of the electron-nucleus pair during the revolution at the corresponding frames.

rest frame, experiences a magnetic field given by the equation (1.4)[1].

$$\mathbf{B} = \frac{-1}{c^2}\mathbf{v} \times \mathbf{E} \tag{1.4}$$

where c is the speed of the light. The expression in equation (1.4) can further be expressed as

$$\begin{aligned}\mathbf{B} &= \frac{-1}{m_e c^2}\left(m_e \mathbf{v} \times \left|\frac{\mathbf{E}}{\mathbf{r}}\right| \mathbf{r}\right) \\ &= \frac{1}{m_e c^2}\left|\frac{\mathbf{E}}{\mathbf{r}}\right| (\mathbf{r} \times \mathbf{p}) \\ &= \frac{1}{r m_e c^2}\left(\frac{\partial V}{\partial r}\right)\mathbf{L}\end{aligned} \tag{1.5}$$

Here, we have made use of the relationship: $\mathbf{p} = m_e \mathbf{v}$, $\mathbf{E} = \left|\frac{\mathbf{E}}{\mathbf{r}}\right| \mathbf{r} = \frac{1}{r}\left(\frac{\partial V}{\partial r}\right)\mathbf{r}$, and $\mathbf{L} = \mathbf{r} \times \mathbf{p}$. Using the above relations, we have expressed the magnetic field experienced by the electron in terms of the angular momentum of the electron $\mathbf{L}$ and the coulomb potential V.

The intrinsic spin property of the electron enables the electron to have its own magnetic moment. The magnetic moment of the electron due to its spin is given by [1]

$$\boldsymbol{\mu_s} = g_e \frac{e}{2m_e}\mathbf{S} \tag{1.6}$$

where g_e is the g-factor and $\mathbf{S}$ is the spin angular momentum. The interaction of

this magnetic moment of the electron (due to its spin) and the previously derived magnetic field (due to its orbital motion) gives rise to spin-orbit coupling or spin-orbit interaction. This SOC interaction is defined using a Hamiltonian (energy operator) given by [1]

$$\begin{aligned}\hat{H}_{SO} &= -\boldsymbol{\mu_s} \cdot \mathbf{B} \\ &= -g_e \frac{e}{2m_e^2 c^2 r} \left(\frac{\partial V}{\partial r}\right) \mathbf{S} \cdot \mathbf{L} \\ &\approx \frac{1}{2m_e^2 c^2 r} \left(\frac{\partial U}{\partial r}\right) \mathbf{S} \cdot \mathbf{L} \end{aligned} \tag{1.7}$$

In order to get the final expression of equation (1.7), we have used $g_e \approx -2$ and $U = -eV$(potential energy); furthermore, we have also taken into account a relativistic correction called *Thomas precession* that contributes a (1/2) factor to the final expression.

The spin-orbit interaction causes the energy of the electron to shift depending on the spin component of the electron. The energy shift can be calculated using the expectation value of the Hamiltonian in equation (1.7). Generally, atoms with larger atomic numbers exhibit greater spin-orbit interaction ($\propto Z^4$)[6][1]. Spin-orbit interaction not only causes shifts in energy but also gives rise to spin-dependent phenomena in solids. These phenomena are discussed more in detail to grasp the idea of spin torques.

1.3.1 Spin currents due to spin Hall effect

The spin Hall effect is a consequence of the spin-orbit interactions in non-magnetic metals. In the previous section, we discussed a simplistic model where the spin angular momentum of the electron interacted with the coulomb potential of the hydrogen-like atom giving rise to SOC. In a crystalline solid, the arrangement of atoms results in a periodic electrostatic potential landscape. The electrostatic potential of the crystal can interact with the spin angular momentum of the electrons resulting in a similar spin-orbit interaction as in the case of the hydrogen-like atom. This spin-orbit interaction of electrons with the crystal lattice causes spin-up and spin-down electrons to deflect to opposite sides of the conductor giving rise to a net spin accumulation on the lateral surfaces of the conductor.

The spin Hall effect gives rise to a flow of spin current in the transverse direction when an electric current flows through the conductor. The generated transverse spin current $\mathbf{j_s}$ is perpendicular to both the charge current $\mathbf{j_c}$ and the spin-polarization direction $\boldsymbol{\sigma}$, and can be described as [6][5]:

$$\mathbf{j_s} = \frac{\hbar}{2e}\theta_{SH}\boldsymbol{\sigma} \times \mathbf{j_c} \tag{1.8}$$

where, θ_{SH} is the spin Hall angle term that describes the conversion efficiency of charge current to spin current. A schematic illustration of the generation of spin currents in a heavy metal (HM) / ferromagnetic metal (FM) heterostructure due to the spin Hall effect is given in figure (1.3.2).

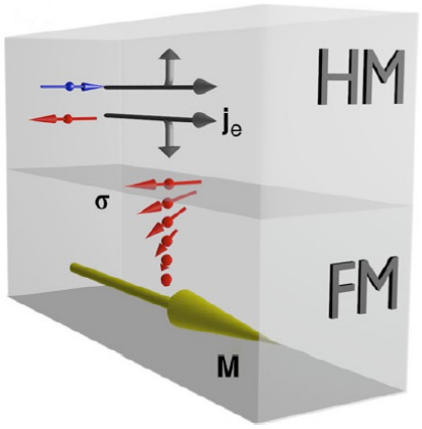

[7]

Figure 1.3.2: Schematic of the generation of spin current in HM/FM heterostructure due to the spin Hall effect.

Figure (1.3.2) shows the generation of transverse spin current in the HM layer due to the flow of longitudinal electric current. In the figure, $\mathbf{j_e}$ shows the direction of the flow of electrons (opposite to $\mathbf{j_c}$), and the red and blue spheres with arrows represent the spin polarization of the electrons. A transverse flow of the spin angular momentum can be seen in the figure when oppositely polarized electrons travel in the opposite direction across the HM layer. The transverse flow of differently polarized spins is represented by the arrows drawn on top of the flow of the electrons. The polarization of spins, due to SHE, at the edges of the HM layer gives rise to spin diffusion. During spin diffusion, spin angular momentum is transferred or diffuses from the HM layer

to the FM layer, exerting a torque on the local magnetic moments. The diffusion of spins from the HM layer into the FM layer is illustrated in the gradual twisting of the red arrows in the figure.

1.3.2 Rashba-Edelstein effect

Spin-orbit coupling can also give rise to an effect called the Rashba effect (also referred to as the Rashba-Edelstein effect) in certain configurations. The Rashba effect is intimately tied to the breaking of inversion symmetry at an interface or heterojunction between materials with strong SOC. Inversion symmetry breaking refers to the loss of symmetry when a structure is not identical upon inverting its spatial coordinates; in simple terms, the structure is not the same when flipped. One such occurrence when this happens is at the interface of a heterostructure where two materials with different electronic structures are brought into contact, which breaks the perfect inversion symmetry of the crystal lattice. The lack of inversion symmetry due to asymmetric interfaces, in the heterostructure, creates an effective electric field in a direction perpendicular to the interface. Electrons moving through this interface see the electric field as an effective magnetic field in their rest frame which can interact with their intrinsic spin angular momentum. The interaction influences the energy of the electrons, depending on the orientation of their spins, when the electrons move through the interface; as a result, the orientation of the spin of the overall electrons, at the interface, preferentially aligns in a certain direction giving rise to a net spin polarization.

We can take a similar approach, as we did while deriving the Hamiltonian for SOC in a hydrogen-like system, to approximate the Hamiltonian of a Rashba system. The interaction of the spin angular momentum of a nearly free electron with the effective magnetic field in its rest frame, while moving through the interface can be expressed as [1][5].

$$\begin{aligned}\hat{H}_R &= -\boldsymbol{\mu_s} \cdot \mathbf{B} \\ &= \mu_B \boldsymbol{\sigma} \cdot \left(\frac{-1}{c^2} \mathbf{v} \times \mathbf{E} \right) \\ &\propto \boldsymbol{\sigma} \cdot (-\mathbf{k} \times \mathbf{z}) \\ &= \alpha_R \boldsymbol{\sigma} \cdot (\hat{\mathbf{z}} \times \mathbf{k}) \end{aligned} \tag{1.9}$$

where μ_B is the Bohr magneton, $\boldsymbol{\sigma}$ is the Pauli vector, $\mathbf{k}$ is the wave vector of the electron, $\mathbf{E}$ is the electric field generated in $\mathbf{z}$ direction (normal to the interface), and α_R is the Rashba parameter. Here, we have made use of $\boldsymbol{\mu_s} \simeq \frac{-e}{m_e}\mathbf{S} = \mu_B\boldsymbol{\sigma}$ and equation (1.4) in the second line of the derivation. The Hamiltonian shows that the energy of electrons with opposite spins in the direction of $(\hat{\mathbf{z}} \times \mathbf{k})$ is different. A schematic of the Rashba effect in HM/FM heterostructure is shown in figure (1.3.3).

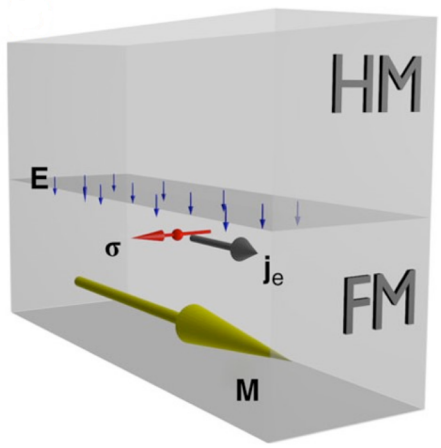

Figure 1.3.3: Schematics of the Rashba effect in HM/FM heterostructure.

The figure (1.3.3) shows the interfacial Rashba effect in an HM/FM heterostructure. The effective electric field between the HM/FM interface (due to inversion asymmetry) is illustrated in the figure by downward blue arrows. The flow of the electrons represented by $\mathbf{j_e}(\propto \mathbf{k})$ through the electric field gives rise to a net spin polarization, represented by the red arrow, in a direction that is orthogonal to both the electric field and the current density. This net spin polarization of electrons can then influence the magnetization of the adjacent magnetic layer through exchange interaction.

1.4 Spin Torques

The spin angular momentum of the electron can apply torques on the local magnetization of the metal and, in doing so, change the magnetization of the metal. The torques applied by the interaction of the spin of the electrons are called spin torques. There are two types of spin torques: *spin-transfer torque (STT)* and *spin-orbit torque (SOT)*. These spin torques are discussed further in the following section.

1.4.1 Spin Transfer Torque

When a stream of polarized electrons passes through an FM layer having a different direction of magnetization than the spin angular momentum of the polarized electrons, the polarized electrons tend to apply a torque on the local magnetization; this effect that arises as a consequence of the conservation of angular momentum is spin-transfer torque. Figure (1.4.1) aids in explaining the phenomena in more detail by considering a system of nonmagnetic (NM) and ferromagnetic (FM) layers.

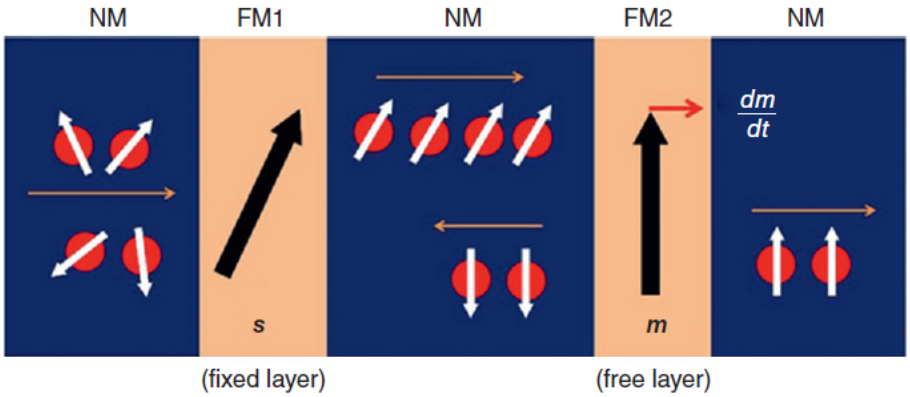

[1]

Figure 1.4.1: STT phenomenon in an NM/FM1(fixed)/NM/FM2(free)/NM layer structure.

The electron passing through the NM layer has a random spin orientation when an electric current is applied to it. As the unpolarized electrons encounter the NM/FM1 interface, the unpolarized electrons get polarized as they move through the fixed layer FM1, which has a local magnetization set along unit vector $\boldsymbol{s}$. The spin-polarized electrons then pass through the NM layer, sandwiched between FM1 (fixed) and FM2 (free) layers, and encounter the NM/FM2 interface. If the local magnetization of FM2, $\boldsymbol{m}$, is not parallel to the direction of spins of the polarized electrons, some spin-polarized electrons again tend to align their spins to the magnetization $\mathbf{m}$ of the free layer to pass through FM2 while other are reflected from the interface. While doing so, the spin angular momentum component of conducting electrons transverse to $\mathbf{m}$ is lost; due to the conservation of the angular momentum, the loss of the perpendicular component of the spin angular momentum applies a torque on the magnetization of the free layer. This apparent torque can switch the magnetization of the free layer when the spin-polarized electron current density is greater than some threshold value.

The transfer of torque by the spin-polarized electron discussed here is called the spin-transfer torque. [1]

A spin torque device that uses spin transfer torque is *Magnetic Tunnel Junction (MTJ)*. It has two ferromagnetic layers of thin films separated by a spacer, usually a non-magnetic metal or a tunnel junction [8]. The magnetization of one of the two ferromagnetic layers is fixed or pinned and the other is free to rotate. The magnetization of the free layer is manipulated using a spin-polarized current and a bit information is stored within the structure depending on the orientation of the magnetization of the two FM layers. If the magnetization of the FM layers is collinear then that state has very small resistance; hence, current can easily flow through the structure and the circuit can be assumed to be closed. Contrary to this, when the magnetization of the FM layers is opposite to each other then the resistance is very high; therefore, current can not easily flow through the structure and the circuit can be assumed to be open. Since the switching of the magnetization depends on the rate of flow of the spin-polarized electrons, a larger current can switch the magnetization faster; however, using a larger current raises questions about the reliability and durability of the spacer between the FM layers. Thus, devices using spin transfer torque have limitations and boundaries.

1.4.2 Spin-Orbit Torque

While the source of the spin-transfer torque is the spin-polarized current, it is generally agreed that the principal sources of the spin-orbit torques (SOT) are the spin Hall effect and the Rashba effect, discussed earlier. The SOT model is usually based on a heavy metal /ferromagnet (HM/FM) bilayer structure. The spin Hall effect and the Rashba effect, arising from the HM layer, collectively give rise to the so-called *damping-like torque* ($\boldsymbol{\tau_{DL}}$) and *field-like torque* ($\boldsymbol{\tau_{FL}}$) components of the SOT; these torques then act on the magnetization of the FM layer causing it to change its orientation. Schematic of the SOT process in HM/FM heterostructure is illustrated in figure (1.4.2).

Figure (1.4.2) shows the anatomy of the SOT process in an HM/FM structure with in-plane magnetization. The schematics show the generation of the spin current and the spin polarization in the HM layer when an electric current flows through the layer.

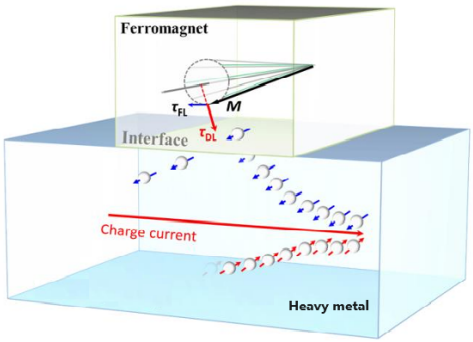

[9]

Figure 1.4.2: Schematics showing the anatomy of the SOT in an HM/FM structure with in-plane magnetization.

The flow of the spin current can be seen in the transverse direction of the HM layer as the electric current flows longitudinally. In the figure, the damping-like and the field-like torques, due to the spin current and the spin accumulation, are perpendicular to each other, and they can be seen acting on the precessing in-plane magnetization of the ferromagnet.

The torques of SOT are dependent on the orientation of the magnetization of the FM layer and the direction of spin polarization. The damping-like and the field-like torques give rise to their respective effective fields, $\mathbf{H_{DL}}$ and $\mathbf{H_{FL}}$, while acting on the magnetization of the FM. Since our focus of study is an HM/FM structure with perpendicular magnetization, schematics showing the direction of the constituents of the SOT in a system with perpendicular magnetization are illustrated in figure (1.4.3).

Figure (1.4.3) illustrates the directions of the torques ($\boldsymbol{\tau_{FL}}$ and $\boldsymbol{\tau_{DL}}$) and their effective fields ($\boldsymbol{H_{FL}}$ and $\boldsymbol{H_{DL}}$) in an HM/FM structure with perpendicular magnetization ($\mathbf{M}$). When the magnetization of the FM is perpendicular to the interface, the field-like and damping-like components are all restricted to the plane of the FM. It can also be noted that the torques and the magnetization are all orthogonal to each other. Under this configuration, $\boldsymbol{\tau_{FL}}$ and $\mathbf{H_{DL}}$ point in the same direction as $\mathbf{j_c}$, $\mathbf{H_{FL}}$ point in the same direction as $\boldsymbol{\sigma}$, and $\boldsymbol{\tau_{DL}}$ point in the opposite direction of $\boldsymbol{\sigma}$. The direction of the spin polarization depends on the flow of the electric current $\mathbf{j_c}$ in the

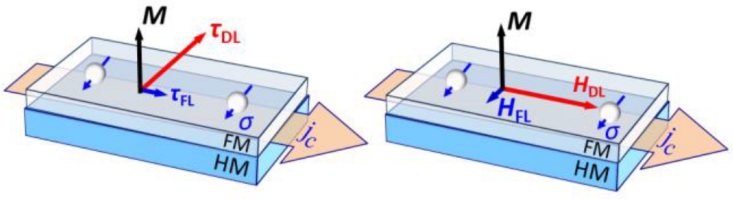

[9]

Figure 1.4.3: The directions of the field-like and damping-like torques ($\boldsymbol{\tau_{FL}}$ and $\boldsymbol{\tau_{DL}}$) and their effective fields ($\boldsymbol{H_{FL}}$ and $\boldsymbol{H_{DL}}$) on perpendicular magnetization in an HM/FM structure. The torques and their effective fields are a consequence of spin current and spin polarization ($\boldsymbol{\sigma}$) arising from the flow of electric current ($\mathbf{j_c}$) in the HM.

HM layer. It must be noted that the direction of the torques and their effective field changes as the orientation of the magnetization changes under SOT.

The effects of SOT can be solved in magnetic systems by integrating the torque terms, discussed here, in the equation describing the dynamics of the magnetization. The equation describing the magnetization dynamics and the inclusion of SOT will be discussed later in the numerical modeling section of the thesis.

1.5 Materials for SOT

The strength of SOT relies on spin-orbit coupling interactions; consequently, the realization of SOT requires the use of particular materials and specific configurations. The efficiency of SOT devices heavily depends on the choice of material exhibiting strong spin-orbit coupling. One such class of materials that exhibits high SOT efficiencies is heavy metal. Heavy metals such as tantalum (Ta), platinum (Pt), and tungsten (W), under specific thicknesses, demonstrate strong spin-orbit coupling interactions, making them good sources of SOT. Their high atomic number leads to enhanced spin-orbit coupling, resulting in efficient conversion of charge current to spin current. Tantalum, platinum, and tungsten have been extensively studied as SOT source materials and their corresponding SOT efficiencies have been reported in the literature. Commonly accepted values of spin-torque efficiencies, θ_{SOT}, in the

literature for platinum is 0.10, tantalum is -0.10 and tungsten is -0.33.[10]

Besides heavy metals, another novel class of materials that has a huge prospect in SOT-inspired technologies is topological insulators (TIs). Topological insulators, like bismuth selenide (Bi_2Se_3) and bismuth telluride (Bi_2Te_3), are materials that possess insulating bulk states but conducting surface states. These surface states of topological insulators exhibit strong spin-orbit coupling, making them attractive candidates for SOT applications. SOT efficiency as high as $\theta_{SOT} = 2.0$ or 3.5, an order larger than in conventional heavy metals, has been reported while using bismuth selenide in a $Bi_2Se_3/Ni_{80}Fe_{20}$ structure [11].

Several other materials from categories belonging to 2D materials, oxides and magnetic insulators, antiferromagnets, ferrimagnets, and low-damping ferromagnets are still being actively evaluated for their potential as sources of SOT. Some materials such as graphene, transition metal dichalcogenides (TMDs), yttrium iron garnet, and $SrTiO_3/LaAlO_3$ interface have been found to work as viable sources of SOT. [10]

The SOT material we use in our study is tungsten (W); cartoon representations of the unit cells of the crystal structures of $\alpha - W$ and $\beta - W$ are illustrated in figure (1.5.1). In the case of tungsten, the large SOT efficiency ($\theta_{SOT} \approx -0.33$) is associated with $\beta - W$, which can only be realized in ultrathin films of a few nanometers. The structure of tungsten film transforms to $\alpha - W$ when the thickness of the film is increased; $\alpha - W$ is not preferred in SOT experiments due to its comparatively lower SOT efficiency. [10]

The $\alpha - W$ represented in figure (1.5.1a) has body centred cubic crystal structure; it is the commonly occurring phase of tungsten in bulk. The $\beta - W$ represented in figure (1.5.1b) is a special A15 phase of tungsten that usually occurs and stabilizes at thin films of few nanometers. Experimental studies of spin Hall angle ($|\theta_{SH}| = |J_s/J_e|$) in magnetic systems with different phases of tungsten report $\theta_{SH} = -0.14$ for $\alpha - W$ and $\theta_{SH} = -0.33$ for $\beta - W$, signifying a higher spin Hall effect in $\beta - W$. [12] The higher spin Hall effect in $\beta - W$ allows us to speculate that the result must be the consequence of the closely packed atoms of the A15 phase of tungsten, enabling higher SOC.

(a) $\alpha - W$ (BCC)

(b) $\beta - W$ (A15 Phase)

[12]

Figure 1.5.1: The unit cell of **a)** $\alpha - W$, this common phase of tungsten has body centered cubic (BCC) lattice structure, **b)** $\beta - W$, this is a special phase of tungsten which is often referred to as A15 phase. Both red and green spheres in **(b)** are tungsten atoms, they are colored differently for distinction and clarity.

Chapter 2

Numerical Modelling

If a system can be modeled numerically, modeling the system is essential while attempting an experimental endeavor. Primary reasons to model a system are to i) approximate or validate analytical theories, ii) predict novel phenomena, iii) interpret findings of experimental approach and iv) test or optimize the design of the device. The principal aspirations for using numerical modeling in this project are to predict and approximate critical points of the experiment, and to develop a better understanding of the acquired results.

The framework used in this project to model the experimental approach is micromagnetics. The term "micromagnetics" was coined by Brown in his book *Micromagnetics* [13] while summarizing "magnetization curve theory" and "domain theory"; these theories are the most popular bases used to solve magnetization problems on nanometer and micrometer scale. Micromagnetics solves the evolution of magnetic dipoles by approximating them as continuous vector fields in small time steps, usually in picoseconds. The dynamics of vector fields are governed by imposing that they obey the Landua-Lifshitz-Gilbert (LLG) equation. Furthermore, the LLG equation can be extended by adding additional torque terms to solve systems with spin-polarized and pure spin currents.

The LLG equation is a differential equation that explains the complex precessional motion of magnetization in solids. The equation is named after its founders Lev Landau, Evgeny Lifshitz, and T.L. Gilbert. The final LLG equation was formed after an improvement by Gilbert over the original equation by Landau and Lifshitz. The LLG equation is expressed as

$$\frac{d\mathbf{M}}{dt} = -\left|\gamma\right| \mathbf{M} \times \mathbf{H_{eff}} + \frac{\alpha}{M_s}\left(\mathbf{M} \times \frac{d\mathbf{M}}{dt}\right) \tag{2.1}$$

where $\mathbf{M}$ is magnetization, γ is gyromagnetic ratio, α is the Gilbert damping parameter, t is time, and H_{eff} is the effective field. The effective field H_{eff} encompasses contributions from all: magnetostatic field, Heisenberg exchange field, anisotropy field, and external field. [14]

Simulation in our project first focuses on exploring the effect of thermal fluctuations on the probable outcome of the experiment. This approach aims to approximate the factor by which thermal fluctuations change the critical points of the experimental result. Thermal effects are analyzed by modeling nanometer-sized Hall bars. The simulation then focuses on modeling the exact experimental sample, on a micrometer scale, to better understand the acquired experimental data. Schematics of the simulated models are illustrated in figure (2.0.1).

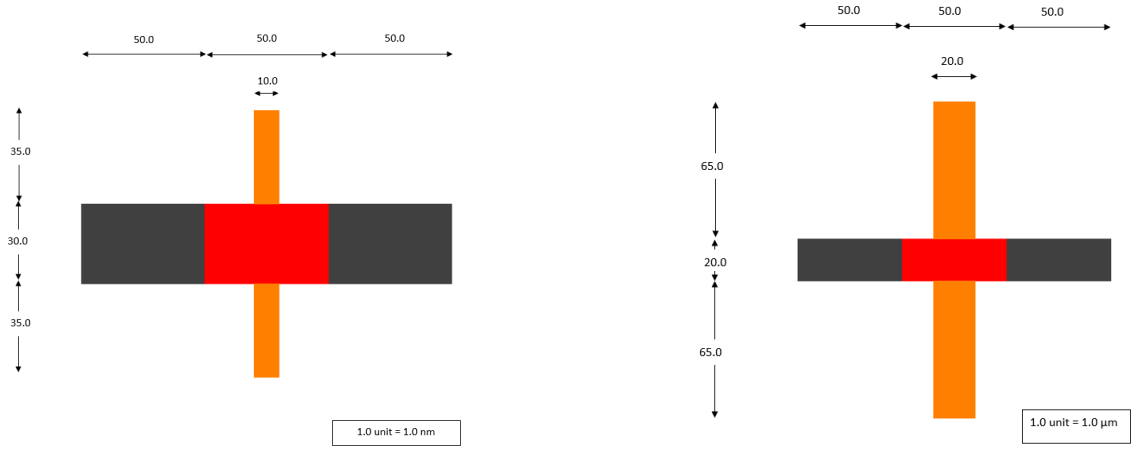

(a) **(b)**

Figure 2.0.1: Schematics of **a)** nanometer (4nm thick), **b)** micrometer (2nm thick), sized Hall bars used in simulations. The central region filled with red color highlights the focus region of the simulation.

The dimensions in figure (2.0.1a) are in nanometers while the dimensions in figure (2.0.1b) are in micrometers. The thickness of the nanometer-sized Hall bar is modeled

to be 4nm; a smaller thickness of 2nm is used in the simulation of a micrometer-sized Hall bar. The main focus of the simulation is centered on the red region of the figure as the change in magnetization of the highlighted region will be responsible for changes in the Hall voltage. For simulations involving SOT, the spin configurations of the voltage arm, portrayed by the reddish brown color region in the figure, are exempted from the applied current. A spatial current density profile is used to model such behavior in our model.

In order to simulate the experiment, the widely popular object-oriented framework tool OOMMF has been used. A brief overview of the simulation software and its important aspects are discussed beforehand to better understand the method of simulations.

2.1 OOMMF

OOMMF (Object Oriented Micromagnetic Framework) is a public domain modeling tool to carry out micromagnetics calculations. The program is developed by the National Institute of Standards and Technology. OOMMF is based on C++ and Tcl/Tk and is supported across multiple platforms. [15]

The modeling associated with this thesis has been done using OOMMF eXtensible solver. The Oxs (OOMMF eXtensible Solver) is an extensible micromagnetic computation engine that solves three-dimensional spin problems defined on three-dimensional grids of rectangular cells. The modeling was mostly done using *Boxsi (Batch OOMMF eXtensible solver interface)* which included extended command line controls enabling its use in shell scripts.

2.2 Problem definition in OOMMF

The problems are mainly defined in OOMMF using scripts. OOMMF requires the use of a MIF (Micromagnetic Input Format) file to specify and set the problems. The program requires a set of Oxs_Ext (Oxs Extension) objects while doing an Oxs simulation which should be initialized in a MIF file. The child classes are used to set different parameters like shapes, sizes, energies, boundaries, and others. A brief description of the available Oxs_Ext classes used in the simulation is given below.

2.2.1 Atlases

Atlases are used to specify the geometric volumes of spaces of the simulation. Atlases specify the bounds for the model. In simple words, the size and shape of the object being simulated are defined using atlases. Oxs_BoxAtlas is the most commonly used atlas in simulations; as the name suggests, Oxs_BoxAtlas represents a boxed rectangular parallelepiped that encompasses a single region. In our simulations, a number of smaller Oxs_BoxAtlas are combined together to make the simulation world; a combination of Oxs_BoxAtlas was carried out through the use of Oxs_MultiAtlas, which allows combining other atlases to form a single region.

2.2.2 Meshes

Meshes are used to define the cellsize used in the simulation. Cellsize discretizes the region specified by the atlas/atlases into defined cuboids.

2.2.3 Energies

Magnetic systems possess different types of energy that must be included in models for correctly predicting the behavior of the system. Each energy term has its own Oxs child class that needs to be defined to include its effect in the system. Some of the common energy terms and child classes are Oxs_UniaxialAnistropy, Oxs_UniformExchage, Oxs_Demag, and Oxs_FixedZeeman. Oxs_UniaxialAnistropy is used to specify an anisotropic property of the simulation model. Oxs_UniformExchage is used to include the exchange interactions between the neighboring cells. Oxs_Demag is used to include the effect of demagnetization energy and field. Similarly, Oxs_FixedZeeman is used to include the effect of the Oersted field arising as the consequence of applying current through metallic strips.

2.2.4 Evolvers

Evolvers updates the magnetization configuration and advances the simulation from one step to the next. The damping factor α and gyromagnetic ratio γ of the LLG equation are specified using this class. This class also allows us to control the time step by which the simulation evolves. There are two kinds of evolvers: time and minimization evolvers. Time evolvers couples with time driver and advances the simulation; the control factor with this evolver is time. Likewise, minimization evolvers couples

with minimization drivers to find the minimum or stationary energy of the system. Since we are dealing with spin-orbit torques, the drivers used in our simulation are a type of time driver that takes the spin momentum term into account.

2.2.5 Drivers

Drivers are an essential and mandatory part of the micromagnetic calculations in OOMMF. The evolvers are tasked to move the simulation forward in individual steps, while the drivers coordinate the simulation altogether by arranging the steps into tasks, stages, and runs. In simple words, evolvers evolve the simulation forward while drivers control the evolvers and the overall simulation by setting stopping conditions. Stopping criteria, iteration limits and different checkpoints can be specified using the driver objects. Drivers and evolvers should be matched accordingly to run simulations and the time evolvers require the use of time drivers; thus, the only type of drivers used in simulations are time drivers.

2.2.6 Other

OOMMF is a very extensive simulation software that includes numerous features to solve different problems of micromagnetics. There are other Oxs child objects that allow the integration of vector and scalar fields but they are not discussed here; OOMMF user guide [15] has a comprehensive overview of all the things available in OOMMF.

2.3 Augmentation in LLG

Simulation models solve specific equations to approximate the overall behavior of a system; modification of the equation is required if additional effects have to be included in simulations. The inclusion of additional factors such as thermal effects, Oersted field, and spin-orbit torque effects in simulations has been accomplished by adding supplementary terms in the equation (2.1). The incorporation of additional factors used in our models is discussed in the following section before proceeding forward.

2.3.1 Incorporating thermal effects

Magnetic systems and their evolution are simulated by a cellwise numerical integration of LLG. Introducing temperature parameter in an already working LLG is usually done by introducing a thermal fluctuation field together with the effective field in the equation. The thermal fluctuation field is chosen in such a way that it imitates and adds the random agitation of the magnetization, caused by thermal effects. The original LLG equation after adding the thermal fluctuation field becomes the stochastic LLG differential equation. The stochastic LLG equation is given by [16]

$$\frac{d\mathbf{M}}{dt} = -\left|\gamma\right| \mathbf{M} \times (\mathbf{H_{eff}} + \mathbf{H_{th}}) + \frac{\alpha}{M_s}\left(\mathbf{M} \times \frac{d\mathbf{M}}{dt}\right) \tag{2.2}$$

where $\mathbf{H_{th}}$ is the thermal fluctuation field. The mean of such fluctuation field must be zero such that the temperature does not drive the system in a particular direction and merely acts as a randomizing agent. The fluctuation field can also be assumed to have a Gaussian distribution, as the randomness is a consequence of myriad interactions underlying crystal lattice. A fluctuation field satisfying these criteria is given by [16]

$$\mathbf{H_{th}} = \hat{\eta}\sqrt{\frac{2\alpha k_B T}{\left|\gamma\right| \mu_0 M_s V \Delta t}} \tag{2.3}$$

where α is the Gilbert damping factor, γ is the gyromagnetic ratio, μ_0 is the permeability of free space, M_s is saturation magnetization, k_B is the Boltzmann constant, T is temperature, V is Volume, Δt is the time step of simulation, and $\hat{\eta}$ is a Gaussian stochastic vector. This fluctuation field is also known as the Langevin thermal fluctuation field.

2.3.2 Incorporating Oersted field from conductor

When current flows through a conductor, the magnetic field is induced around the wire. If the wire is long enough, the magnetic field lines form concentric circles around the wire perpendicular to the wire. The direction of these curls is given by the curling fingers of the right hand if one wraps his/her hand around the wire with the thumb in the direction of the current. These fields will be present no matter the size of the devices we make. To incorporate these fields and observe their effect on the dynamics

of the magnetization of our nano and micron-sized structures, we deduce the analytic expression of the field generated by the following approach.

In the experiment we use Hall bars of length 150 μm and width $10\mu m$ or $20\mu m$ to probe the direction of magnetization of the magnetic layer. The magnetization of the magnetic layer we are interested in lies in the middle portion of the Hall bar. Under this configuration, we can assume that the length of the conductor is long enough and we have a uniform field from the current-carrying conductor stacked with the magnetic layer.

The field from the current flowing conductor can be calculated by integrating individual contributions from an infinitely small section of the wire using the Cartesian coordinate system as shown in the figure (2.3.1).

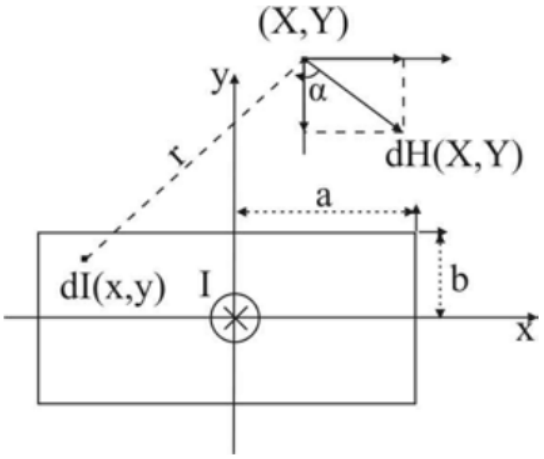

[17]

Figure 2.3.1: Coordinate system defined for integrating contributions to Oersted field from elementary current wires.

The elementary current element at (x, y) inside the rectangular strip produces a radial field of

$$dH(X,Y) = \frac{j \cdot dxdy}{2\pi r}$$

in A/m. Replacing $j = \frac{I}{4ab}$ in the expression and re-writing r in Cartesian coordinate

gives

$$dH(X,Y) = \frac{I \cdot dxdy}{8\pi ab \cdot \sqrt{(x-X)^2 + (y-Y)^2}} \tag{2.4}$$

The elementary field contributions from small current elements in the x and y directions are given by

$$dH_y = dH \cdot cos\alpha$$
$$dH_x = dH \cdot sin\alpha$$

Writing $cos\alpha$ and $sin\alpha$ in terms of the assumed coordinate space gives

$$sin\alpha = \frac{Y-y}{\sqrt{(x-X)^2 + (y-Y)^2}}$$
$$cos\alpha = \frac{X-x}{\sqrt{(x-X)^2 + (y-Y)^2}}$$

We can combine all these expressions with the expression of $dH(X,Y)$ in equation (2.4) and integrate along the x and y directions to get the corresponding field generated at point (X,Y). The final integrals are expressed in equation (2.5) and (2.6).

$$H_x(X,Y) = \frac{-I}{8\pi ab} \int_{-a}^{a} \int_{-b}^{b} \frac{y-Y}{(x-X)^2 + (y-Y)^2} dydx \tag{2.5}$$

$$H_y(X,Y) = \frac{I}{8\pi ab} \int_{-a}^{a} \int_{-b}^{b} \frac{x-X}{(x-X)^2 + (y-Y)^2} dydx \tag{2.6}$$

Integrating equation (2.5) over x gives:

$$H_x(X,Y) = \frac{-I}{8\pi ab}\int_{-b}^{b}\int_{-a}^{a}\frac{(y-Y)dx}{(y-Y)^2\left[\left(\frac{x-X}{y-Y}\right)^2+1\right]}dy$$

$$= \frac{-I}{8\pi ab}\int_{-b}^{b}\int_{-a}^{a}\frac{d\left(\frac{x-X}{y-Y}\right)}{\left(\frac{x-X}{y-Y}\right)^2+1}dy$$

$$= \frac{-I}{8\pi ab}\int_{-b}^{b} atan\left(\frac{x-X}{y-Y}\right)\Bigg|_{-a}^{a} dy$$

$$= \frac{-I}{8\pi ab}\left[\int_{-b}^{b} atan\left(\frac{a-X}{y-Y}\right)dy - \int_{-b}^{b} atan\left(\frac{-a-X}{y-Y}\right)dy\right] \qquad (2.7)$$

We note here that the integration required further in equation (2.7) is in the form:

$$\int atan\frac{1}{x}dx = x\cdot atan\frac{1}{x} + \int\frac{1}{x^2\left(1+\frac{1}{x^2}\right)}xdx \qquad = x\cdot atan\frac{1}{x} + \frac{1}{2}ln(x^2+1)$$

Integrating the first term of equation (2.7) yields:

$$\begin{aligned}
&\int_{-b}^{b} atan\left(\frac{a-X}{y-Y}\right)dy \\
=&\int_{-b}^{b}(a-X)atan\left(\frac{a-X}{y-Y}\right)d\left(\frac{y-Y}{a-X}\right) \\
=&(a-X)\left[\left(\frac{y-Y}{a-X}\right)atan\left(\frac{a-X}{y-Y}\right)+\frac{1}{2}ln\left(\left(\frac{y-Y}{a-X}\right)^2+1\right)\right]\Bigg|_{-b}^{b} \\
=&(a-X)\Big[\frac{1}{2}ln\left(\frac{(b-Y)^2+(a-X)^2}{(-b-Y)^2+(a-X)^2}\right)+\left(\frac{b-Y}{a-X}\right)atan\left(\frac{a-X}{b-Y}\right)... \\
&...-\left(\frac{-b-Y}{a-X}\right)atan\left(\frac{a-X}{-b-Y}\right)\Big]
\end{aligned}$$

And the second integral gives:

$$\begin{aligned}&\int_{-b}^{b} atan\left(\frac{-a-X}{y-Y}\right) dy\\ =&(-a-X)\Big[\frac{1}{2}ln\left(\frac{(b-Y)^2+(-a-X)^2}{(-b-Y)^2+(-a-X)^2}\right)+\left(\frac{b-Y}{-a-X}\right)atan\left(\frac{-a-X}{b-Y}\right)...\\ &...-\left(\frac{-b-Y}{-a-X}\right)atan\left(\frac{-a-X}{-b-Y}\right)\Big]\end{aligned}$$

Therefore, the final expression in x-direction can be written as:

$$H_x(X,Y)=\frac{-I}{8\pi ab}\cdot\begin{bmatrix}(a-X)\Big[\frac{1}{2}ln\left(\frac{(b-Y)^2+(a-X)^2}{(-b-Y)^2+(a-X)^2}\right)+\left(\frac{b-Y}{a-X}\right)atan\left(\frac{a-X}{b-Y}\right)...\\ ...-\left(\frac{-b-Y}{a-X}\right)atan\left(\frac{a-X}{-b-Y}\right)\Big]...\\ ...-(-a-X)\Big[\frac{1}{2}ln\left(\frac{(b-Y)^2+(-a-X)^2}{(-b-Y)^2+(-a-X)^2}\right)+\left(\frac{b-Y}{-a-X}\right)atan\left(\frac{-a-X}{b-Y}\right)...\\ ...-\left(\frac{-b-Y}{-a-X}\right)atan\left(\frac{-a-X}{-b-Y}\right)\Big]\end{bmatrix} \tag{2.8}$$

In a similar manner, the final expression for $H_y(X,Y)$ can be derived to be [17]:

$$H_y(X,Y)=\frac{I}{8\pi ab}\cdot\begin{bmatrix}(b-Y)\Big[\frac{1}{2}ln\left(\frac{(b-Y)^2+(a-X)^2}{(b-Y)^2+(-a-X)^2}\right)+\left(\frac{a-X}{b-Y}\right)atan\left(\frac{b-Y}{a-X}\right)...\\ ...-\left(\frac{-a-X}{b-Y}\right)atan\left(\frac{b-Y}{-a-X}\right)\Big]...\\ ...-(-b-Y)\Big[\frac{1}{2}ln\left(\frac{(-b-Y)^2+(a-X)^2}{(-b-Y)^2+(-a-X)^2}\right)+\left(\frac{a-X}{-b-Y}\right)atan\left(\frac{-b-Y}{a-X}\right)...\\ ...-\left(\frac{-a-X}{-b-Y}\right)atan\left(\frac{-b-Y}{-a-X}\right)\Big]\end{bmatrix} \tag{2.9}$$

The spatial distribution around the current carrying rectangular strip can be modeled correctly using equations (2.8) and (2.9).

Sample images of the Oersted field generated in a nanometer-sized strip simulated in OOMMF are given in figure (2.3.2). The figure depicts the Oersted field generated on the magnetic layer resting on top of the SOT metal (conductor). Figure (2.3.2a) shows the view of the Oersted field generated in the cross-sectional plane made by the thickness and width of the magnetic layer when a positive current flows into the plane of the paper. Similarly, the Oersted field across the plane subtended by the length and width of the magnetic film is shown in figure (2.3.2b); here, the direction

of the current is across the length of the strip in the upward direction (i.e. north). The colormap representing the strength of the z-component of the magnetization is illustrated at the top left section of the figure (2.3.2) (this colormap is also used to represent the z-component of the magnetization in all simulation outputs of our thesis).

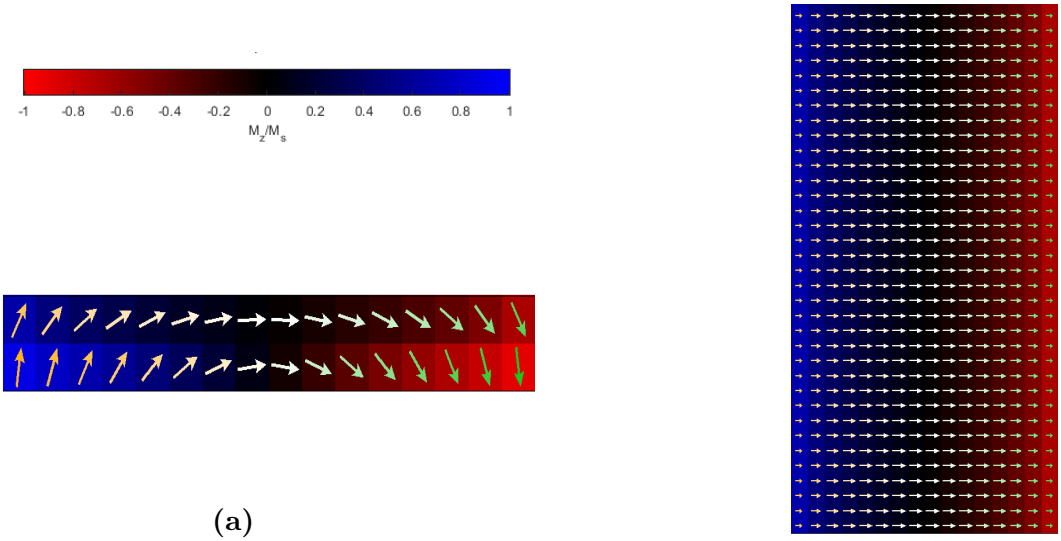

(a) **(b)**

Figure 2.3.2: Oersted field as seen in the plane of the cross section subtended by **a)** width and thickness, **b)** width and length, of the magnetic field resting on top of a conductor. The colormap used in denoting the strength of the z-component of the magnetization is given at the top left section of the figure.

2.3.3 Spin Orbit Torque using OOMMF

The effect of spin-orbit torque in magnetic systems can be captured by adding an additional term in the LLG ODE. LLG equation with the added torque term can be represented as equation (2.10)[18].

$$\frac{d\mathbf{m}}{dt} = -|\gamma|\mathbf{m} \times \mathbf{H_{eff}} + \alpha \left(\mathbf{m} \times \frac{d\mathbf{m}}{dt} \right) + \boldsymbol{\tau_{SOT}} \tag{2.10}$$

where,

$$\boldsymbol{\tau_{SOT}} = -\overbrace{|\gamma|\tau_S \mathbf{m} \times (\mathbf{m} \times \boldsymbol{\sigma})}^{\boldsymbol{\tau_{DL}}} - \overbrace{|\gamma|\tau_F (\mathbf{m} \times \boldsymbol{\sigma})}^{\boldsymbol{\tau_{FL}}}$$

The spin-orbit torque, as discussed in section (1.4.2), comprises of the damping-like (DL) and field-like (FL) components. Rewriting and expanding the terms of equation (2.10) results in the final equation (2.11).

$$\frac{d\mathbf{m}}{dt} = -|\gamma|\mathbf{m} \times \mathbf{H_{eff}} + \alpha \left(\mathbf{m} \times \frac{d\mathbf{m}}{dt} \right) - |\gamma|\tau_S \mathbf{m} \times (\mathbf{m} \times \boldsymbol{\sigma}) - |\gamma|\tau_F \left(\mathbf{m} \times \boldsymbol{\sigma} \right) \quad (2.11)$$

with

$$\tau_s = \frac{\theta_{SOT}}{2} \left| \frac{\hbar}{\mu_0 e} \right| \frac{J^{SOT}}{t_F M_s}$$

$$\xi = \frac{\tau_F}{\tau_S}$$

Here, $\mathbf{m} = \mathbf{M}/M_s$ is the reduced magnetization, γ is the Gilbert gyromagnetic ratio, α is the damping parameter, $\boldsymbol{\sigma}$ is the unit vector along the direction of spin polarization of current generated by the spin Hall effect, θ_{SOT} is the spin-orbit torque efficiency, J^{SOT} is the current density, t_F is the thickness of the (free)magnetic layer, τ_S is the damping-like coefficient, τ_F is the field-like coefficient and ξ is a constant factor to correlate damping-like and field-like coefficients.[18]

SOT can be modeled in OOMMF using its *Oxs_SpinXferEvolve* class. Oxs_SpinXferEvolve is a time evolver class that integrates spin momentum terms with the LLG ODE. This class can be used to model both, spin-transfer torque (STT) and spin-orbit torque (SOT) effects. The augmented equation solved by Oxs_SpinXferEvolve is given in equation (2.12).

$$\frac{d\mathbf{m}}{dt} = -|\gamma|\mathbf{m} \times \mathbf{H_{eff}} + \alpha \left(\mathbf{m} \times \frac{d\mathbf{m}}{dt} \right) + |\gamma|\beta\epsilon(\mathbf{m} \times \mathbf{m_p} \times \mathbf{m}) - |\gamma|\beta\epsilon'\mathbf{m} \times \mathbf{m_p} \quad (2.12)$$

Here,

$$\beta = \left|\frac{\hbar}{\mu_0 e}\right| \frac{J}{tM_s}$$
$$\mathbf{m_p} = \text{(unit) electron polarization direction}$$
$$\epsilon = \frac{P\Lambda^2}{(\Lambda^2+1)+(\Lambda^2-1)(\mathbf{m}\cdot\mathbf{m_p})}$$
$$\epsilon' = \text{secondary spin transfer term.}$$

We can reduce the equation (2.12) of Oxs_spinXferEvolve into equation (2.11) by making appropriate substitutions of parameters. First, the Lambda parameter Λ must be set to 1 to remove the dependence of ϵ on $\mathbf{m}\cdot\mathbf{m_p}$. We can also note that the electron polarization direction vector $\mathbf{m_p}$ can completely encapsulate the effect of spin polarization direction vector $\boldsymbol{\sigma}$. After doing the substitution

$$\Lambda = 1 \longrightarrow \epsilon = \frac{P}{2}$$

$$J = J^{SOT}$$

$$\epsilon = \frac{\theta_{SOT}}{2} = \frac{P}{2} \Longrightarrow \theta_{SOT} = P$$

$$\epsilon' = \xi\epsilon = \xi\frac{P}{2}$$

The above substitution allows us to model spin-orbit torque in magnetic systems using the Oxs_spinXferEvolve class in OOMMF. We need to correctly assign the direction polarization vector and substitute the spin-orbit efficiency value in the polarization parameter of the class. If field-like torque is to be included in the model, a value for ξ also must be assigned. In our model, the damping-like torque term is considered and the field-like torque term is discarded, as it has been suggested that the field-like torque has no deterministic effect on magnetization switching [19][20]. Field-like torque can be set to zero by setting ϵ' to zero.

2.4 Magnetic material and parameters used

The magnetic material of interest in our simulation is CoFeB. In experiments, we use CoFeB which is made up of an atomic composition of 20% Cobalt, 60% Iron, and 20% Boron. CoFeB thin films are popular because of their ability to induce perpendicular magnetic anisotropy (PMA) in the ultra-thin thickness range. Thin film with PMA has myriad potential in the storage industry. The summary of material parameters used in our simulations is given in table (2.4.1).

Table 2.4.1: Material parameters used in simulations.

Parameter	Symbol	Value
Magnetization saturation	Ms	$9.57 \times 10^5 A/m$
Exchange a coefficient	A	$13 \times 10^{-12} J/m$
Damping constant	α	0.01
Anisotropy field	Ha	$11000 A/m$ (nm Hall bar)
in (001) direction		$13000 A/m$ (μm Hall bar)

[21]

Note that an anisotropy field is used in place of an anisotropy constant to set the strength of anisotropy; OOMMF allows either quantity to be allocated. A trial and error method was used to set the value of the anisotropy field that could align the overall magnetization of the model in an out-of-plane direction.

2.5 Thermal effects in nanometer-sized CoFeB Hall bars

This chapter compares the result of two models identical in shape and geometry which are evolved using different evolvers. One evolver includes the effect of temperature and another excludes it; in other words, the temperature parameter for one model is 298 K whereas the temperature is set to 0 K in the other model. The objective of this chapter is to observe and quantify any changes in critical switching parameters.

2.5.1 Field-induced magnetization switching

This segment focuses on studying the thermal effects on the states and critical field values required to switch magnetization in an out-of-plane direction. A uniform out-

of-plane field between -2500 Oe to 2500 Oe is applied to the simulation world to induce magnetization switching along the easy axis.

Model description and initial states

The magnetic material being simulated for this task is a nanometer-sized CoFeB Hall bar. The size of the Hall bar portrayed by figure (2.0.1a) is constricted to nanometers to save computational time and cost. The simulation world is discretized with a cell-size of $2nm \times 2nm \times 2nm$ dimensions. The easy axis of the Hall bar is fixated to be in [0,0,1] orientation such that it coincides with the out-of-plane axis of the Hall bar. In order to apply a magnetic field to the Hall bar model, a uniform field was generated using *Oxs_FixedZeeman* class. There are other ways to generate uniform fields in oommf but Oxs_FixedZeeman class was used as it would later be used for simulating Oersted fields from the conductor. Snapshots of initial magnetization states obtained after relaxing the simulation world for 5ns with and without thermal effects are given in figure (2.5.1).

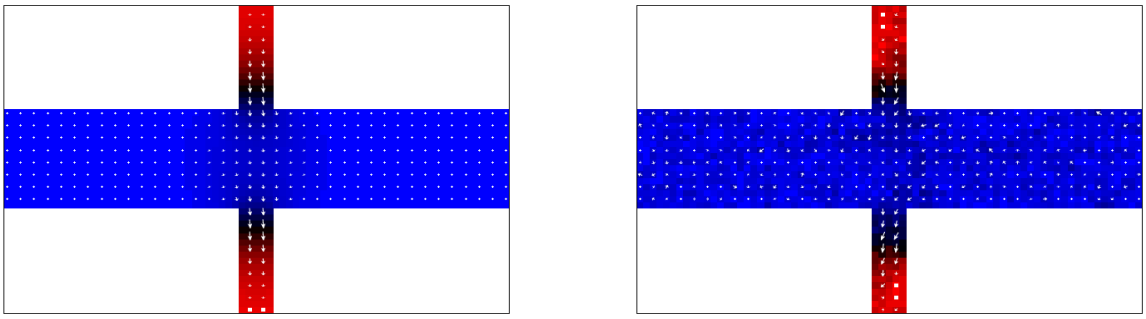

(a) **(b)**

Figure 2.5.1: Magnetization state at a) $T = 0K$ and b) $T = 298K$ of nanometer-size CoFeB Hall bars after relaxing the simulation world for 5ns.

Even though both simulation worlds had the same geometry and their parameters were set identically, the initial states obtained at different temperatures were slightly different. Figure (2.5.1a) shows a smooth and balanced configuration of magnetization across the simulation world whereas figure (2.5.1b) shows a rattled configuration of magnetization due to the inclusion of thermal effect. It can also be observed that the overall magnetization configuration in both cases looks similar if minor differences are set aside.

Result and observation

The initial magnetization states shown in figure (2.5.1) were then evolved under the influence of an external uniform out-of-plane field. The result of the simulation after sweeping the field from -2500 Oe to 2500 Oe and back again is summarized in figure (2.5.2).

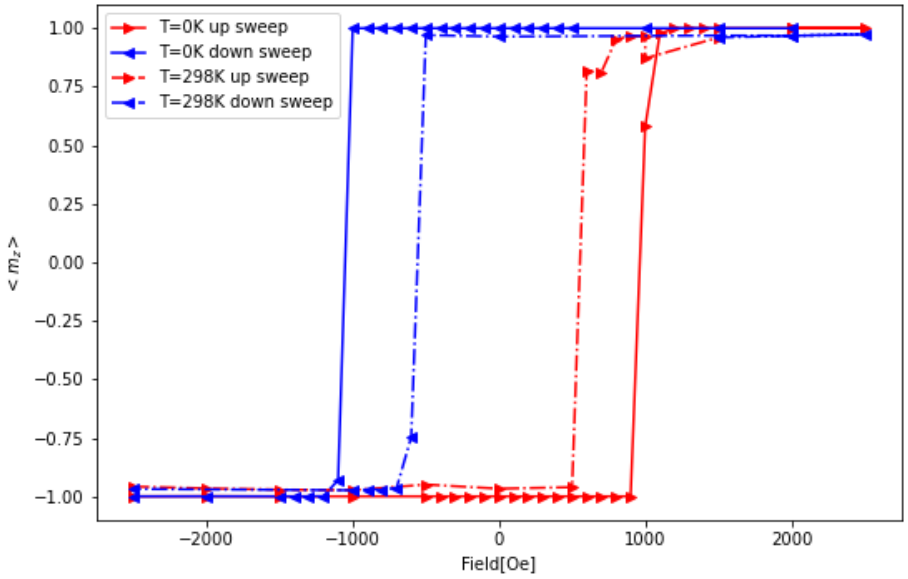

Figure 2.5.2: Hysteresis loops of nanometer-sized Hall bars obtained in the z-direction by sweeping an out-of-plane field at two different temperatures.

Hysteresis loops obtained in figure (2.5.2) clearly demonstrate the effect of including thermal fluctuations. For $T = 0K$, the magnitude of the critical field value for magnetization reversal was 1100 Oe. However, the magnitude of the critical field value needed for magnetization reversal dropped by 500 Oe, requiring only 600 Oe, when the thermal effects were included in the simulation. Furthermore, the effects of including thermal agitation can also be observed in the evolution of magnetization components at different steps of the hysteresis. The evolution of x,y, and z components of the magnetization during hysteresis is shown in figure (2.5.3).
The trend of magnetization components for $T = 0K$ is very smooth and undisturbed. On the other hand, the evolution of magnetization when including thermal effects appears to fluctuate and rattle in all directions. When performing experiments at room temperature, we expect to see behavior similar to the result given by figure

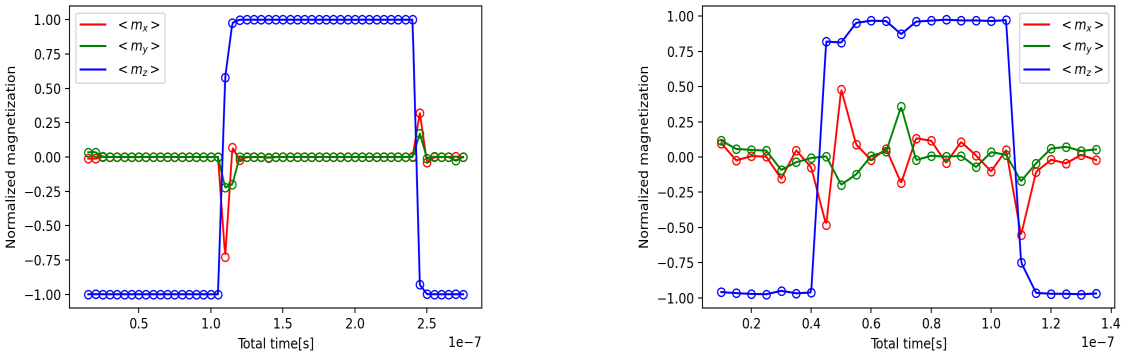

Figure 2.5.3: x, y and z components of the magnetization at different stages of field hysteresis of nanometer-sized CoFeB Hall bar for a) $T = 0K$ and b) $T = 298K$.

(2.5.3b).

2.5.2 SOT-induced magnetization switching

This section is dedicated to the study of thermal effects on magnetization dynamics induced by spin-orbit torque. Simulations carried out with $T = 0K$ parameter are simple and fast; the same is not true when thermal effects are included in the model. Adding additional thermal effects on a simple model increases its complexity making the simulation slower but the result obtained from such a simulation is closer to the outcome likely to be obtained from experiments. The excitation and agitation added by thermal effects tend to lower the critical density parameter while attempting current-induced switching in the magnetic system. In this section, we perform identical simulations, including and excluding thermal effects, to better understand the significance of thermal effects.

Model description and initial states

The model parameters in this section are kept the same as mentioned earlier in section (2.5.1). The corresponding initial states at different temperatures in figure (2.5.1) are evolved with an in-plane magnetic field of 1000 Oe for 5ns; the resultant evolved states are then used as the starting point for SOT simulations. Initial states used for this section are illustrated in figure (2.5.4).

In the figure, we note that the separate simulations, at different temperatures, did not

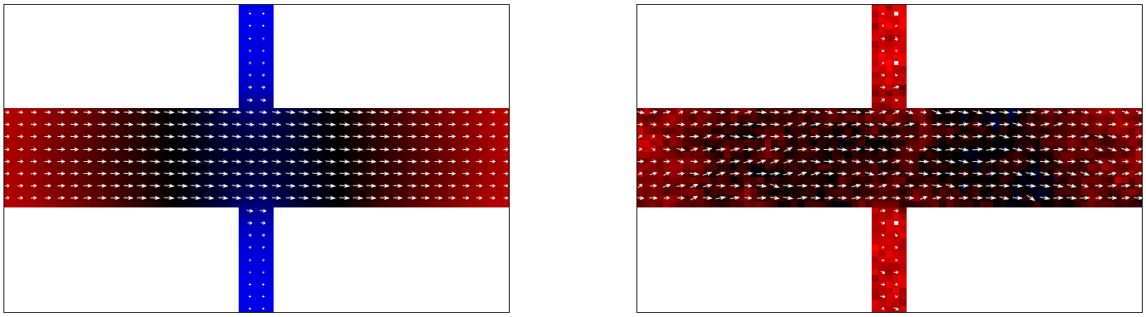

(a) **(b)**

Figure 2.5.4: Magnetization state of nanometer-sized CoFeB Hall structure at a) $T = 0K$ and b) $T = 298K$ with a uniform in-plane field of 1000 Oe after relaxing the simulation world for 5ns.

yield a similar magnetization state. The magnetization states within the narrow arms (voltage electrodes in the experiment) in figure (2.5.4b) appear to have flipped to obtain a stable magnetization state at $T = 298K$. The erratic behavior of magnetization in the presence of thermal effects is also clearly visible in figure (2.5.4b).

Result and Observation

The magnetization states portrayed in figure (2.5.4) evolved under the influence of spin-orbit torque. The current profile used in the SOT evolver class was that of a simple DC source. The magnitude of the modeled current (current density) was changed from $-300\mu A$ to $300\mu A$ in fixed step sizes and the corresponding changes in magnetization were recorded. The result of the simulation is summarized in figure (2.5.5). The figure clearly demonstrates the effect of including thermal agitations. The magnitude of current required for a sudden magnetization reversal during the sweep is lowered when thermal effects are included in the simulation. Magnetization reversal for $T = 0K$ can be observed at a modeled current of $\pm 80\mu A$; whereas, the current magnitude of $\pm 50\mu A$ was enough to reverse the magnetization orientation of the same system. The apparent change in the value of critical current can be directly associated with the inclusion of thermal effect. Both the shape of the hysteresis and the critical switching points differ between $T = 0K$ and $T = 298K$; furthermore, the significant decrease in critical current density required to switch magnetization validates the fact that joule heating assists SOT-switching.

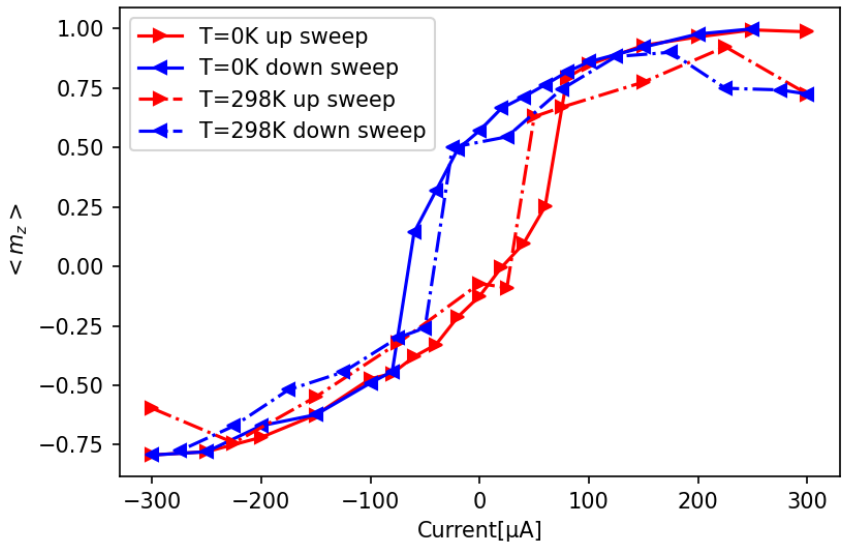

Figure 2.5.5: Magnetization response of nanometer-sized Hall bar at different temperatures while sweeping an in-plane current with a constant in-plane field of 1000 Oe.

2.6 Micrometer-sized Hall bars

This section focuses on studying the evolution and dynamics of magnetic materials on the micro-meter scale. The structure being simulated in this section is a symmetrical Hall bar structure as illustrated in figure (2.0.1b). The Hall bar is similar in shape and geometry to the experimentally fabricated structure. The goal of this section is to understand and predict the overall response of the magnetic system in situations similar to the experimental setup.

2.6.1 Field-induced magnetization switching

A simple way to characterize the magnetic properties of a magnetic system is to conduct field hysteresis. Magnetic systems are subjected to out-of-plane and in-plane magnetic fields, the magnitude of the field is gradually changed, and the response of the magnetic system is recorded. Hysteresis loops provide information about the coercivity, remanence, and anisotropy of a magnetic system. The information about the easy and hard axis of a magnetic system can be easily seen from hysteresis loops. To characterize our model simulation, we first perform in-plane and out-of-plane hysteresis and observe the response of the magnetic system in response to the applied

field.

Model description and initial state

The magnetic material used here is a 2nm thick CoFeB film in the shape of a symmetric Hall bar. The dimension of an individual cell used to discretize the simulation world is $500nm \times 500nm \times 1nm$. The shape of the cell is not a cube but a cuboid stretched equally in the x and y directions. The unit cell of the model has dimensions larger than the exchange length of the magnetic system; however, we expect to capture the approximate behavior of the magnetic system of our interest through the simulations. The easy axis of the model system is fixated in $[0, 0, 1]$ orientation with an anisotropy field of 13000 Oe; anisotropy can be allocated in OOMMF either by assigning crystalline anisotropy constant or by fixing an anisotropy field. The uniform magnetic field is generated using the $Oxs\_FixedZeeman$ class. Since the size of the simulation world here is bigger than the previous nanometer-sized model, the stopping time of each stage here is 10ns. An image of the simulation world after relaxing the model system for 10ns is given in figure (2.6.1).

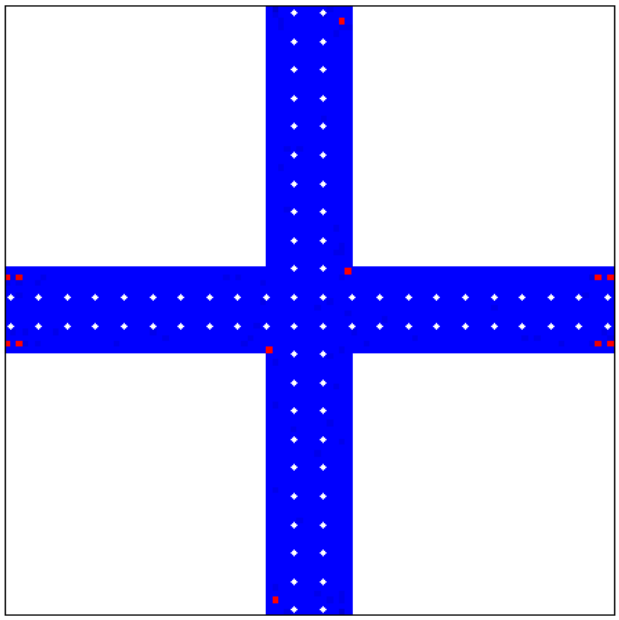

Figure 2.6.1: Initial magnetization state of micrometer-sized Hall bar after relaxing the magnetic system for 10ns.

The relaxed magnetic system in figure (2.6.1) shows signs of perpendicular magnetic anisotropy; blue-colored regions in the figure include magnetization in out-of-plane orientation while small red segments include magnetization directed into-the-plane.

Result and observation

The magnetic model depicted in figure (2.6.1) was evolved simulating the presence of an applied external magnetic field, and the corresponding magnetization components were recorded. The range of uniform field applied to the system was between $-10,000\ Oe$ to $10,000\ Oe$. The field was swept through the system by gradually increasing or decreasing the uniform field in fixed step size. The final result of the simulation is illustrated in figure (2.6.2).

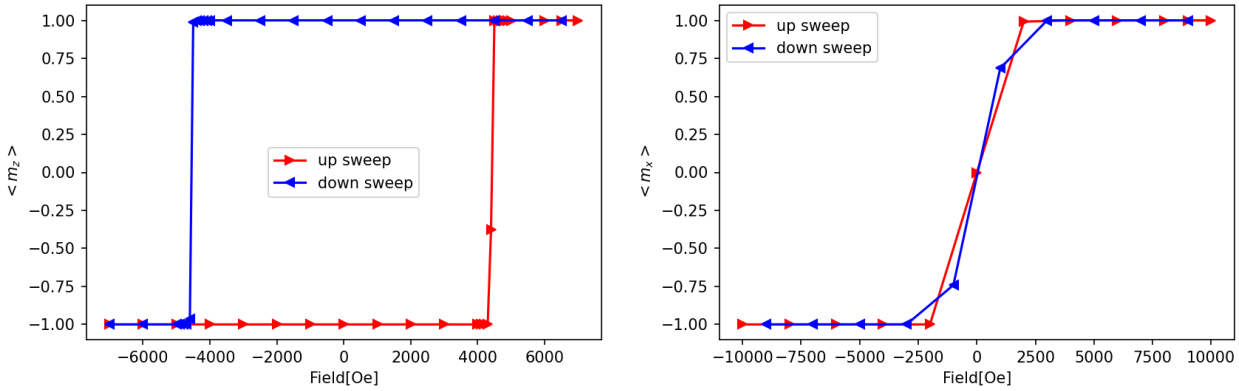

(a) **(b)**

Figure 2.6.2: Corresponding magnetization components while sweeping the magnetic field in **a)** out-of-plane direction **b)** in-plane direction, for micrometer-sized Hall bar.

The results from field sweeps, shown in figure (2.6.2), clearly signify the presence of perpendicular magnetic anisotropy in the model system. Figure (2.6.2a) indicates a strong sign of remanence during out-of-plane field sweeps; the magnetic system was able to withstand opposing field strength up to 4500 Oe (in magnitude) before reversing the orientation of inherent magnetization. Figure (2.6.2b), on the other hand, shows that the system did not retain much magnetization while sweeping the field in the in-plane direction. The narrow hysteresis loop consolidates the assumed configuration of the model's easy axis in an out-of-plane direction. It can also be seen

in figure (2.6.2b) that the system does not require a field higher than 2500 Oe to win over the perpendicular anisotropy field.

2.6.2 SOT-induced magnetization switching

SOT-induced magnetization switching is a phenomenon of manipulating the orientation of magnetic moments, or magnetization, in a magnetic material using spin-orbit torques through the use of an electric current. This section will focus on studying the magnetic systems where spin-orbit torques are realized.

Our study focuses on studying a bi-layer magnetic system where a magnetic film is coupled together with a heavy metal film. The heavy metal layer acts as the source of spin-orbit torque. When current passes through the heavy metal layer, spin currents are generated and suffused along the transverse direction; the spin currents then apply a torque on the magnetic layer residing on top or bottom of the heavy metal layer. In our model, the magnetic layer is discretized and simulated by integrating the spin-orbit torque effect in the equation driving the magnetization dynamics, namely the LLG equation. Different SOT source materials have different spin-orbit efficiencies to exert torques on the adjacent magnetic material. While simulating the SOT effect, corresponding SOT efficiency has to be used depending on the source material for spin-orbit torque. In our model, we are using $\beta - Tungsten$ as the source of SOT; the spin-orbit torque efficiency, θ_{SOT} for tungsten is reported to be approximately -0.33 [22].

Field assisted magnetization switching through DC

Current-induced magnetization reversal in in-plane magnetic film can be easily achieved; in such a system, magnetization switching can be achieved without the need for an external magnetic field. The same can not be achieved for a magnetic system with perpendicular magnetic anisotropy (PMA). Magnetic films with PMA require an additional in-plane external magnetic film to allow a deterministic magnetization reversal. Figure (2.6.3) shows a very simplified configuration of magnetization under the influence of different fields undergoing field-assisted current-induced magnetization switching.

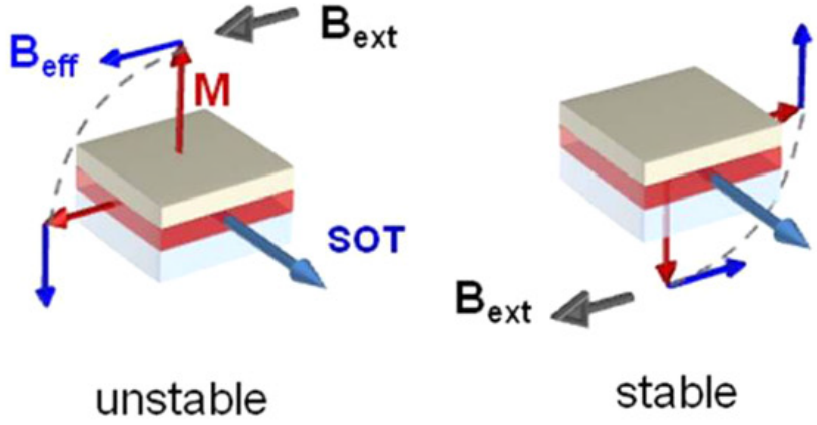

[23]

Figure 2.6.3: Schematics of a simplified MTJ configuration having a perpendicular magnetization under the influence of an external field, and SOT effective field.

The configuration in figure (2.6.3) shows the external magnetic field, the magnetization, and the SOT field all perpendicular to each other. The figure shows a state to be an unstable one when the effective field and the external applied field both share the same orientation causing the magnetization to rotate. When the configuration of fields involved reaches a compromise such that the effective field balances out the externally applied field, such state is shown in the figure as a stable state. A proper magnetization switching can only be achieved in magnetic films with PMA if all the components in figure (2.6.3) do not solely dominate the magnetic system.

The initial sets of simulations, performed to gain insight into the critical switching parameters (critical current density and critical field value), were all done simulating a DC source. The current density profile, unless specified, resembles the density profile of a constant DC source which is very easy to assign and adjust.

Current sweeps with constant in-plane magnetic field

The purpose of changing the magnitude of current density (current applied) is to find the critical current value needed to switch the magnetization from one orientation to the reverse. Although the magnitude of the current density varied through different stages of the simulation, the modeled external in-plane magnetic field was kept uniform and unchanging throughout all stages. The simulation parameters–geometry,

mesh, and cellsize–were all kept similar to the model parameters set in the previous section (2.6.1). The magnetization state given in figure (2.6.1) was relaxed with an in-plane magnetic field of 1000 Oe for 10ns before applying any current through the conductor. The in-plane magnetic field was adjusted to 1000 Oe after a few trial-and-error simulations where magnetization reversal was observed. The initial state of magnetization used in this section is given in figure (2.6.4a).

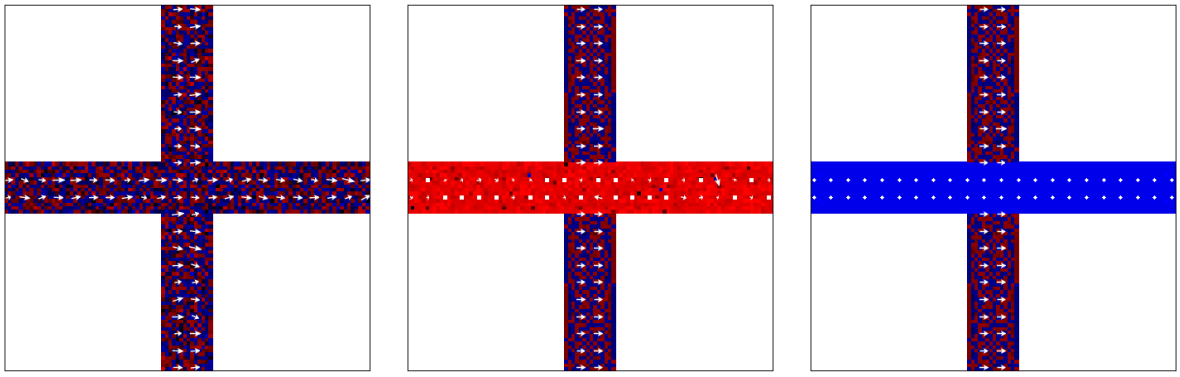

(a) Initial (I = 0mA) **(b)** I = -150mA **(c)** I = 150mA

Figure 2.6.4: Magnetization states at different stages of the current sweep. **a)** Initial relaxed state with an in-plane magnetic field and no current. **b)** Magnetization state when applied current is -150mA. **c)** Magnetization state when applied current is 150mA.

The initial magnetization state was subjected to different current density values at fixed step size. A full sweep in the range -300mA to 300mA was performed and the corresponding magnetization states were recorded. The result of the current sweep is given in figure (2.6.5).

Figure 2.6.5 shows that the z-component of the magnetization responds well to the current density being applied through the conductor. The magnitude of the M_z component increases with the corresponding magnitude of the current density. The average magnetization in the central region points almost completely in the out-of-plane orientation at current values with a magnitude of 150mA, as shown in figure (2.6.4b) and (2.6.4c). Increasing the magnitude of the current beyond 150mA shows a decrease in the perpendicular component of the magnetization; the SOT effect, beyond 150mA, becomes stronger and starts to dominate the effective fields forcing

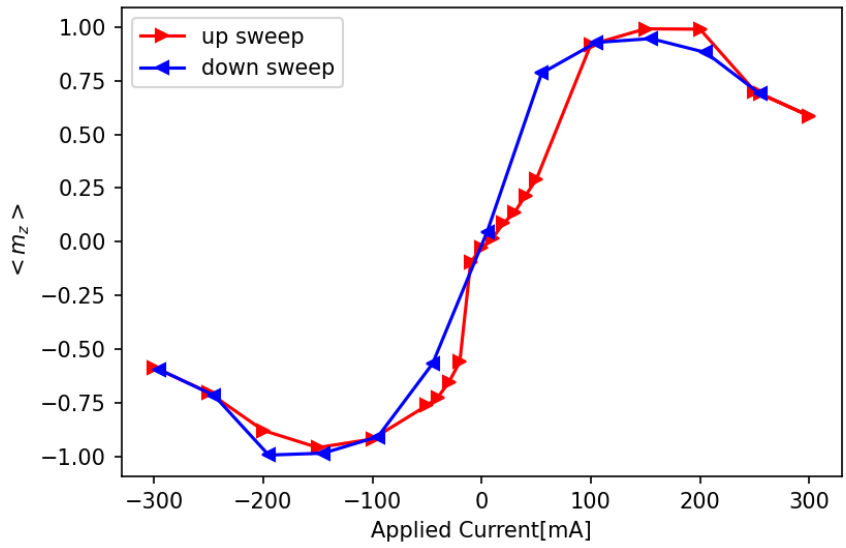

Figure 2.6.5: Average m_z component of the central region during current sweeps with a uniform in-plane magnetic field strength of 1000 Oe.

the magnetization to the effective field generated by SOT (i.e. in the Y-direction).

Field sweeps with constant in-plane current

Changes in magnetization while sweeping current with constant uniform in-plane field were discussed in the previous sub-section (*Current sweeps with constant in-plane magnetic field*); here, we will study the changes in magnetization while sweeping the field with constant in-plane current. In this section, the critical current magnitude is kept constant at 150mA but the value of the simulated external field is changed between -7000 Oe to 7000 Oe with a fixed step size. The simulation is carried out twice to account for separate polarities of the current. The initial magnetization state given in figure (2.6.1) is evolved with constant current (for both polarities) and is allowed to relax for a total of 10ns; the resultant magnetization state is then used as the initial point of the simulation for each concerned polarity. The initial magnetization states and maximum m_z component stages obtained during the simulation are illustrated in figure (2.6.6).

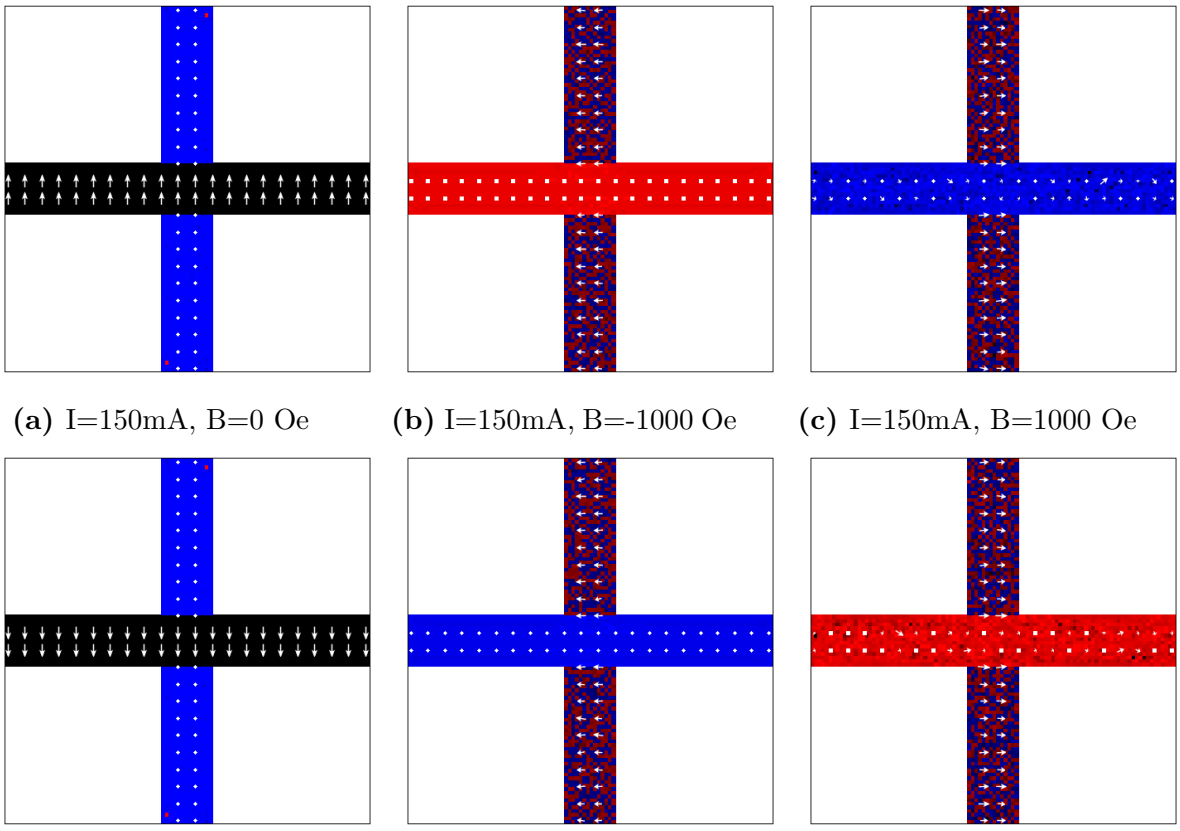

(a) I=150mA, B=0 Oe **(b)** I=150mA, B=-1000 Oe **(c)** I=150mA, B=1000 Oe

(d) I=-150mA, B=0 Oe **(e)** I=-150mA,B=-1000 Oe **(f)** I=-150mA, B=1000 Oe

Figure 2.6.6: Magnetization states of the micrometer-sized CoFeB Hall bar at different current and field values while sweeping an in-plane external field through the film.

Figure (2.6.6) also shows the simulation stages where the maximum out-of-plane component is achieved during the sweep process, for comparison. Magnetization components can be seen to be the reverse of each other when the polarity of the current is reversed. The complete upshot of the simulation is summarized in figure (2.6.7).

The result in figure (2.6.7) is similar to the experimental result reported by Avci et al.(2012)[23]. Even though the device geometry and the SOT source material in our study are different than the experimental arrangement used by Avci et al.(2012), the same kind of behavior can be expected in a system with out-of-plane anisotropy.

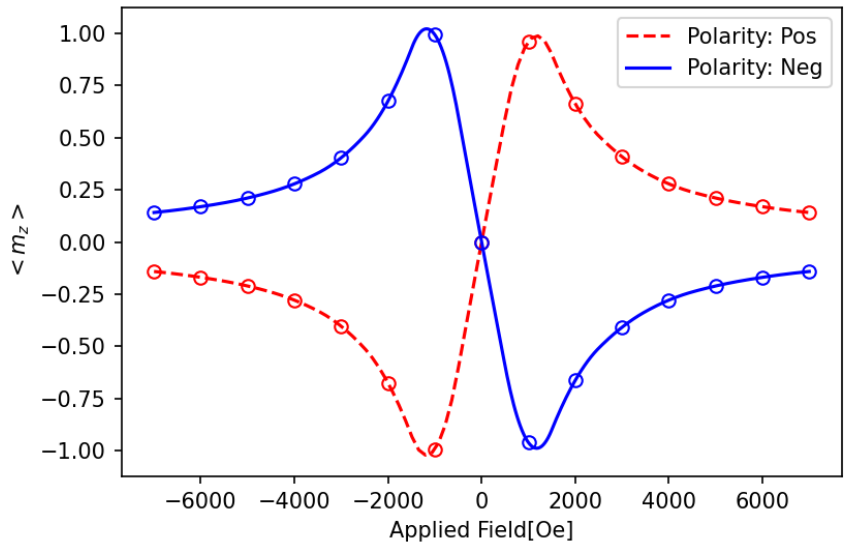

Figure 2.6.7: Changes in magnetization while sweeping a simulated external field at constant in-plane current with magnitude 150mA (red dotted) and -150mA(solid blue).

2.6.3 Magnetization evolution while applying current pulse

Microstructures with a few nanometer thicknesses are very sensitive and fragile; particular care has to be taken while applying current through such structures. Current-induced magnetization switching requires the application of high current density through fabricated structures. A continuous application of constant direct current through the magnetic system can cause excessive heating of the conductor and potentially destroy the structure of interest. To avoid this problem in SOT experiments, current pulses are generally used. A fast current pulse can transfer enough SOT at high current density while keeping the integrity of the fabricated structure. In this section, we will model a short 5ns current pulse, FWHM (full width half maximum), to source SOT in our model magnetic system. We will study the evolution of magnetic components of our model system under the influence of a short current pulse.

The total duration of simulation in this section is 30ns (starts at $t = 0s$ and ends at $t = 30ns$). The current pulse is modeled such that its maximum is obtained at $t = 10ns$ within the simulation window. The current density profile obtained while sourcing a current pulse of 120mA is illustrated in figure (2.6.8). In the figure (2.6.8), we note

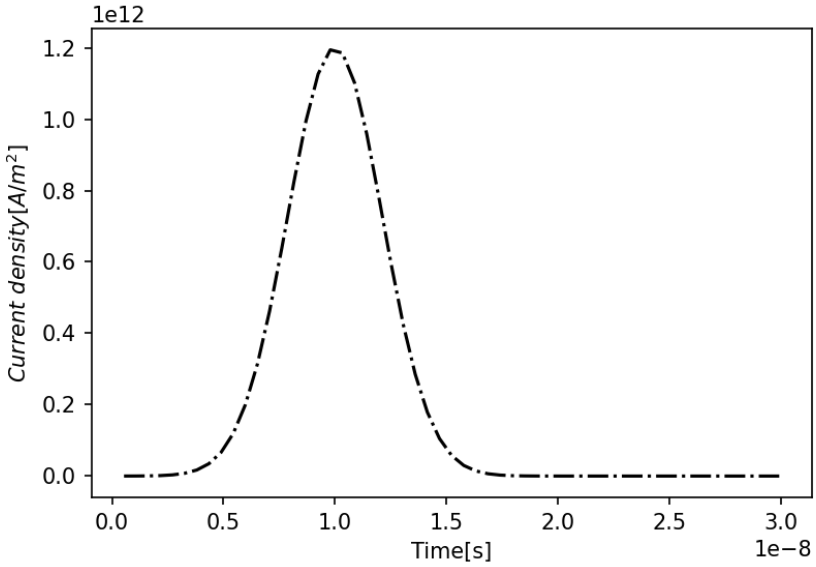

Figure 2.6.8: Current density profile modeled for micrometer-sized CoFeB Hall bar's simulation imitating a current pulse.

that a current pulse with a magnitude of 120mA generates current density as high as $1.2 \times 10^{12} A/m^2$. Such high intensity pulse here is the result of having a structure with a relatively wide cross section. The necessary current density can be reached in experiments if structures with smaller cross section are fabricated. Here we are not including the thermal effects, that would be present while conducting the experiment at room temperature, which would further reduce the required current density to achieve deterministic magnetization reversal. The current pulse when applied to our model magnetic system gradually changes the inherent magnetization components. Changes in the z-component of the magnetization of our model (necessary to realize AHE) while applying the current pulse depicted in figure (2.6.8) are illustrated in figure (2.6.9).

The result shows that the maximum z-component of the magnetization is realized at a slightly lower current density of approximately $1.0 \times 10^{12} A/m^2$; furthermore, increasing current density beyond the value reduces the z-component of the magnetization where SOT starts to dominate. The magnetization configuration appears to become unstable as the current pulse gradually decreases; the unstable magnetization configuration starts to precess in the yz-plane resulting in fluctuating positive and negative y and z components until eventually yielding to the external field applied along the x-direction. The changes in x,y, and z components of the magnetization are shown in

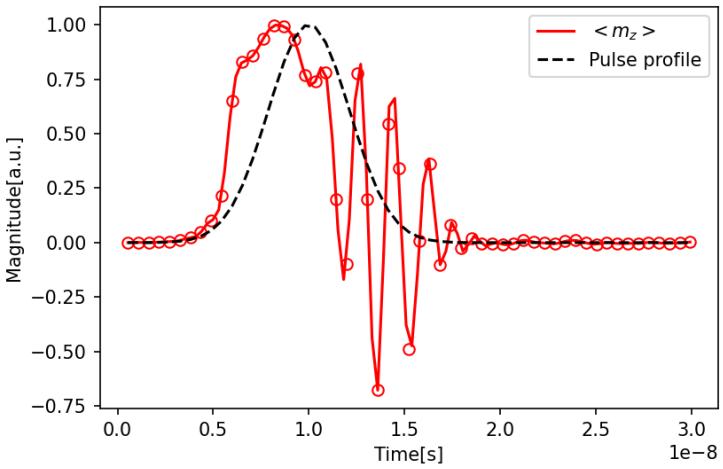

Figure 2.6.9: Changes in z-component of the magnetization over the central region of the modeled Hall bar in response to the simulated current pulse.

figure (2.6.10).

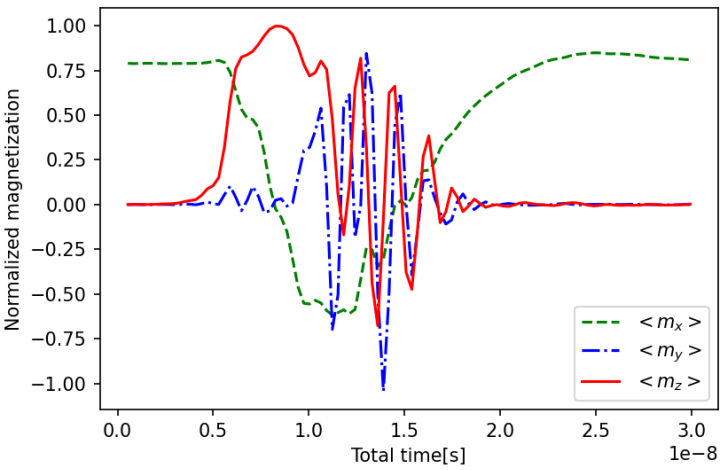

Figure 2.6.10: Changes in the average components of magnetization in response to the modeled 5ns current pulse.

The precession plane of magnetization can be inferred from the figure (2.6.10) by observing the fluctuating average y and z components of the magnetization during the subsiding phase of the current pulse. The ultimate orientation of the magnetization can also be seen to point along the positive x-direction, the same as the direction of

the applied in-plane field after the current pulse subsides completely. A few snapshots of the simulation world at different time intervals are given in figure (2.6.11). The individual cells of the model, i.e. pixels, in figure (2.6.11) are colored according to the corresponding magnetic components at the given point in time; the same color map is used for all magnetic components for simplicity.

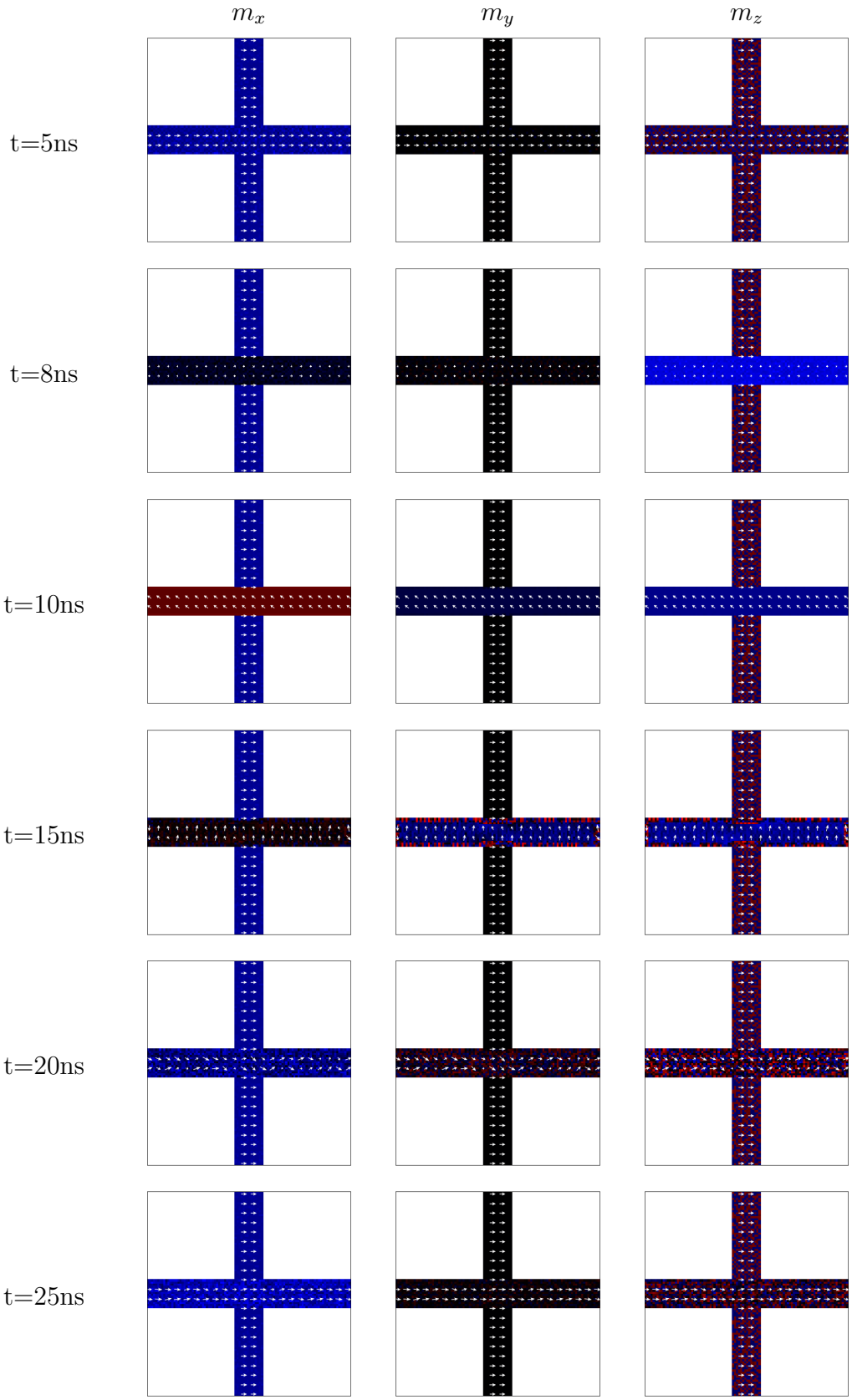

Figure 2.6.11: Evolution of different components of magnetization during the application of pulse through micrometer-sized Hall bar.

Chapter 3

Nanofabrication Techniques

At present, there exists a wide range of techniques to manufacture structures and devices at the micro and nanoscale. These techniques are crucial for the development of advanced materials, electronics, optics, and medical devices. The study of novel phenomena on the micro and nanoscale has been made possible due to these fabrication techniques. A very brief overview of some of the most popular fabrication techniques has been discussed below before diving deep into the fabrication technique used in our study.
‘

1. Lithography: Lithography is an important technique used to pattern and transfer designs onto substrates. Materials can be selectively added or removed to create precise features using lithography. There are various types of lithographic methods that have their own operating principle, resolution, and versatility. The most prevalent types of lithography are photolithography, electron beam lithography (EBL), and nanoimprint lithography. Photolithography uses light to transfer patterns onto a photosensitive material (photoresist) coated on a substrate. EBL utilizes a focused electron beam to create patterns with high resolution. Creating patterns with EBL usually takes a longer time than photolithography. Nano-imprint lithography involves pressing a mold or template onto a substrate to transfer patterns or structures.[24] In our study, the samples are fabricated using photolithography.

2. Thin Film Deposition: Thin film deposition involves depositing a thin layer of material onto a substrate to create functional coatings or device components. There are different types of deposition techniques such as physical vapor depo-

sition (PVD), chemical vapor deposition (CVD), and atomic layer deposition (ALD). PVD techniques involve the deposition of thin films through physical processes, usually in vacuum environments; some physical processes are thermal evaporation, sputtering, electron beam evaporation, and molecular beam epitaxy (MBE). CVD techniques rely on the chemical reaction of vaporized precursor molecules to deposit thin films on the substrate. ALD technique involves the alternate exposure of the substrate to two or more precursor gases, creating a self-limiting surface reaction to give a uniform film. ALD is a precise and controlled deposition technique where thin films are grown one atomic layer at a time.[25][24] In our study, sputtering is used to deposit thin films.

3. Etching: Etching techniques are used to selectively remove material from a substrate to create patterns or structures. Some common etching methods include wet etching, dry etching, and chemical etching. Wet etching and chemical etching involve processes where the substrate is immersed in a chemical solution, while dry etching utilizes reactive gases–in the form of plasma or ions–to etch the substrate. These techniques enable the fabrication of intricate features and high aspect ratio structures. Etching is widely used in the fabrication of integrated circuits.

4. Laser Micromachining: Laser micromachining employs focused laser beams to remove or modify materials at the microscale. It is a versatile technique for creating complex structures, drilling holes, and surface modification. Some of the commonly used laser micromachining processes are laser ablation, laser cutting, and laser engraving.

5. Nanoparticle synthesis: Nanoparticle synthesis techniques produce nanoparticles with controlled size, shape, and composition. Some of the methods that can be put into this category are sol-gel synthesis, chemical precipitation, and aerosol methods.

The structures made in our study were fabricated using photolithography and sputtering techniques. Both of the aforementioned techniques have been explained in detail to shed light on the methods used.

3.1 Sputtering

Sputtering is a physical vapor deposition (PVD) technique that uses high-energy ions to bombard a solid target material, causing atoms or molecules to be ejected from the target surface. The ejected or sputtered species are then deposited onto a substrate in a vacuum chamber to form thin films or coatings. The primary principle underlying sputtering is the transfer of momentum between the impinging ions and target atoms that leads to the ejection of target atoms of the target material. There are three different types of sputtering techniques: DC sputtering, RF sputtering, and Magnetron sputtering. DC sputtering uses a direct current (DC) power source to create a voltage difference between the target material and the substrate; the resultant voltage difference then accelerates the ions toward the target, causing sputtering. It only works for conducting targets. RF sputtering employs a radio frequency (RF) power supply to create an alternating electric field between the target material and substrate. The alternating electric field ionizes the gas in the chamber, generating a plasma. The positively charged ions from the plasma bombard the target material, causing the atoms to sputter. RF sputtering is not limited to conducting targets and is suitable for all conductive and non-conductive materials. Magnetron sputtering is a variation of RF sputtering that exploits the use of magnetron assembly behind the target material to generate a magnetic field that confines the electrons near the surface of the target material. Doing so enhances the plasma density and ionization efficiency of the sputtering process. The Magnetron sputtering technique was used to fabricate structures in our study; hence, the subject will be discussed further.

3.1.1 Magnetron sputtering

Magnetron sputtering sputters atoms of a target material by creating a plasma between a cathode (target material) and an anode (substrate table) exploiting the use of magnetron. A magnetron consists of a cathode assembly which includes integrated permanent magnets or electromagnets. The magnetron assembly creates a magnetic field parallel to the surface of the cathode. The secondary electrons emitted from the cathode surface, as a result of ion bombardment, are confined by the existing magnetic field to traverse in a direction perpendicular to both the magnetic field and the electric field (the electric field is normal to the surface of the cathode). This $\vec{E} \times \vec{B}$

drift path is also known as *racetrack*. The racetrack forces the electrons to travel in a closed loop parallel to the cathode surface in a direction perpendicular to the applied magnetic field. Figure (3.1.1a) shows a circular magnetron assembly highlighting the electron racetrack; furthermore, the motion of the electrons within the racetrack is shown in figure (3.1.1b).

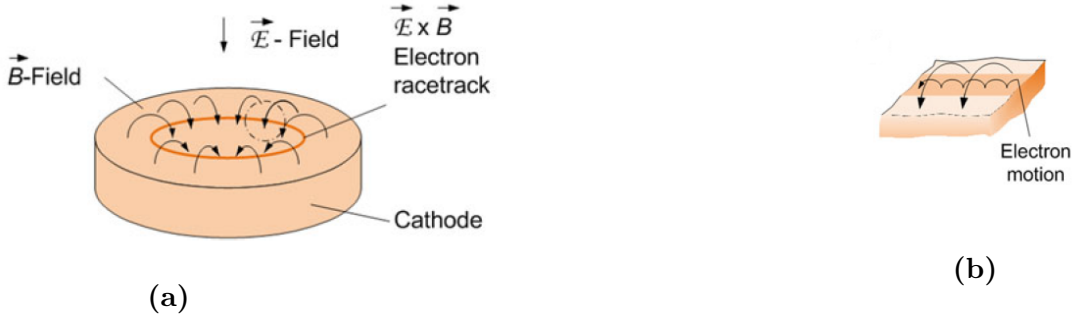

[24]

Figure 3.1.1: A circular magnetron assembly illustrating a) the electron racetrack under the influence of electric and magnetic field, b) motion of the electron within the racetrack.

The entrapped secondary electrons close to the surface of the cathode lose their kinetic energy either with gas atoms (ionization) or with other electrons resulting in an extremely dense plasma along the drift ring. In addition, the confined electrons are prevented from drifting toward the anode substrate table, eliminating the issue of substrate heating.

3.1.2 Sputtering hardware and process

The sputtering system used to fabricate structures in this project is a multi-target sputtering system manufactured by *MANTIS*. It consists of 4 different cathode heads, capable of sputtering 4 different targets within a single deposition cycle under vacuum. The process, and the working principles involved, in sputtering a target material of interest have been briefly discussed below.

Pumping

Most fabrication processes on the micro and nanoscale are usually conducted under partial vacuum conditions. The reason behind this necessity is to provide a free unobstructed path for the atoms in a line-of-sight process, between a source material

and a target substrate. Doing so reduces the chances of the atoms colliding with the existing gas molecules inside the process chamber. Preventing unwanted collisions of the sputtered atoms allows the atoms to reach the substrate with sufficient momentum to adhere to a substrate. Another reason to conduct the fabrication procedure, especially sputtering processes, under vacuum conditions is to reduce contamination by minimizing the impingement of air or other gas molecules onto the substrate surfaces. Partial vacuum conditions are classified by different labels depending on the pressure range they reach inside the process chamber. The classification of vacuum phases is given in table (3.1.1). [24]

Table 3.1.1: Classification of vacuum phases

Degree of vacuum	Pressure range	
	[Pa]	[Torr]
Rough	$10^5 > p > 10^2$	$750 > p > 7.5 \times 10^{-1}$
Fine	$10^2 > p > 10^{-1}$	$7.5 \times 10^{-1} > p > 7.5 \times 10^{-4}$
High	$10^{-1} > p > 10^{-5}$	$7.5 \times 10^{-4} > p > 7.5 \times 10^{-8}$
Ultrahigh	$10^{-5} > p$	$7.5 \times 10^{-8} > p$

The vacuum level inside the process chamber during sputtering processes plays an important role in determining the quality and purity of the deposited film. Our sputtering system can reach as low as $2 \times 10^{-5}\ mbar \approx 2 \times 10^{-3}\ Pa$; thus, our process chamber can reach a high vacuum before initiating sputtering. The system uses two pumps: roughing and turbo pumps, to pump the gas out of the process chamber.

Plasma ignition and sputtering

After pumping the gases from inside the process chamber of the sputtering system, Argon (an inert gas) is discharged in controlled proportion through a gas inlet. The high frequency oscillating electric field, created by the RF generator, ionizes the neutral argon atoms. The positive Argon ions are then accelerated towards the negatively charged target, usually referred to as the cathode in spite of changing polarity due to the AC source. The Ar ions then knock the atoms of the target material (so-called cathode) and are deposited onto the substrate resting on a grounded sample table (so-called anode). A schematic showing the sputtering process for a single target system has been shown in figure (3.1.2).
The additional components of the figure (3.1.2) all have their roles during the sputtering process. As discussed earlier, the magnetron located beneath the target material

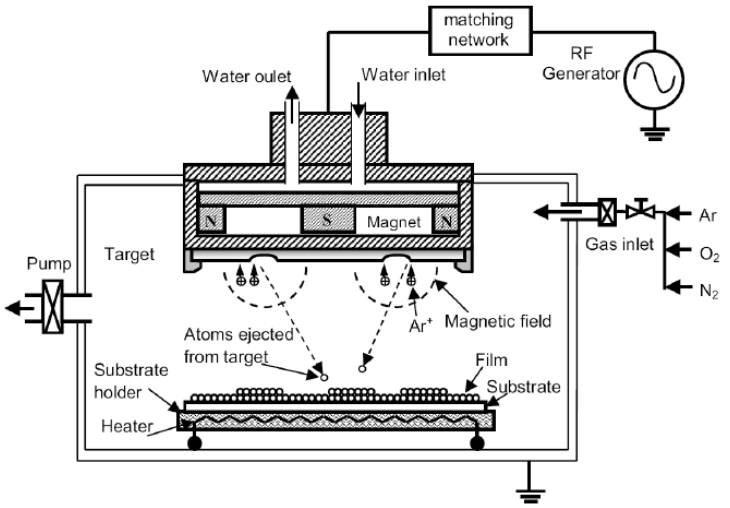

[26]

Figure 3.1.2: Schematics of RF magnetron sputtering system

contributes to creating and sustaining an extremely dense plasma near the surface of the target material (cathode). Furthermore, the cathode is cooled using a water chiller to regulate the appropriate temperature through the water inlet and outlet emanating from the cathode assembly. While the flow of Argon is maintained at a steady rate, the turbo pump of the system is usually kept in standby mode to pump the excess argon gas from inside the chamber. Even though the schematics show the working principles of a single target RF magnetron sputtering system, our system comprises 4 targets (cathode) system placed adjacent to each other with shutter controls to cover the targets when not in use; nevertheless, our multi-target sputtering system operates exactly as illustrated in figure (3.1.2).

Venting

The final stage of the sputtering process is venting. After a successful deposition of the material onto the substrate, Nitrogen gas is discharged into the chamber using the gas inlet to increase the pressure inside it. The pressure gradually increases and when the pressure inside the chamber is at the same level or more than the ambient pressure, the process chamber can be opened and the coated substrate can be taken out.

Challenges

The Magnetron sputtering process relies on the magnetic field generated by the magnets of the magnetron to enable the sputtering process. Magnetron sputtering has a lot of advantages over ordinary RF and DC sputtering methods; however, it faces some challenges when dealing with ferromagnetic target materials. The ferromagnetic target materials shunt the magnetic field emanating from the inherent magnets, situated within the magnetron assembly. This decrease in the magnetic field strength of the discharge region reduces ion current density, and plasma ionization and causes irregularity of the magnetic field distribution. These factors can result in the reduction of discharge power and deposition rates.[27] Sometimes the magnetic flux can be shunted to the extent that no plasma may ignite; consequently, the deposition of the target material will not be possible. Thus ferromagnetic target materials have to be used with some care while working with a magnetron sputtering system.

To overcome the challenges previously discussed, modifications can be made to either the sputter system or the target material in hand. The easiest modification that allows to circumvent the shunting of magnetic flux is to use very thin target materials, whenever possible. The magnetic field will be able to penetrate the target material if the ferromagnetic target material is very thin and the magnetic field strength of the magnets used is high enough. Manufacturers of target materials usually provide the users with a variety of target thicknesses depending on one's need; it is recommended to acquire ferromagnetic target material with the smallest available thickness from the manufacturer. Another modification that allows us to get around the shunting problem is to simply acquire a cathode with stronger magnets underneath it. Stronger magnets will produce strong fields and hence can penetrate thicker ferromagnetic targets.

3.2 Photolithography

Photolithography plays a crucial role in the production of integrated circuits, advanced electronic devices, and microelectromechanical systems (MEMS). Photolithographic techniques harness the power of light to fabricate precise patterning and intricate structures at the micro and nanoscale. Photolithography is a process of transferring or generating patterns onto a substrate using a particular type of photo-

sensitive coatings; such coatings or materials that are sensitive to light are called photoresists. The most common photolithographic technique uses ultraviolet light (UV) to fabricate structures on the micrometer scale.

Photolithography may or may not require a dedicated photomask to transfer patterns onto a substrate. A photomask is a type of mask that contains patterns on it. The photomask allows some part of the light to pass through it while blocking other portions of the light in such a way that a specific portion of the photoresist–coated on top of the substrate–is exposed to light; in doing so, the pattern is transferred from the mask to the substrate. Here we will only discuss the optical lithographic technique that requires a dedicated photomask, namely: mask-based photolithography. Lithography, in general, requires a sequence of steps to successfully develop patterns onto a substrate. Figure (3.2.1) presents an overview of the all sequences involved in mask-based photolithography.

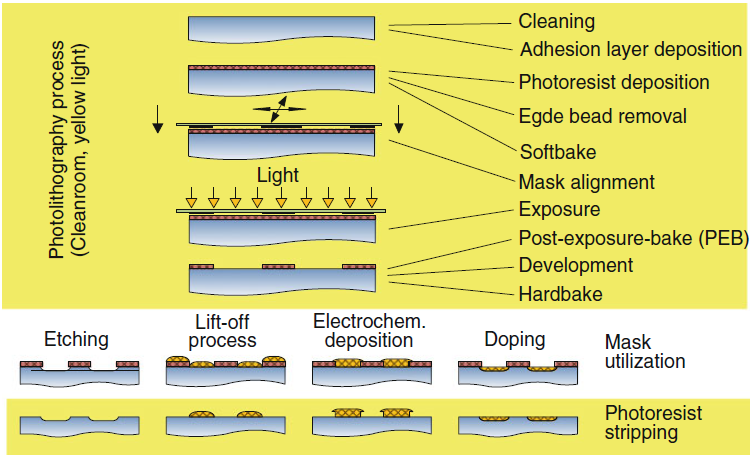

[24]

Figure 3.2.1: Typical sequence of processes for mask-based photolithography.

The sequence of processes given by figure (3.2.1) is usually carried out inside a clean room. Furthermore, the photoresist may be sensitive to typical everyday light sources which may include some electromagnetic radiation close to the ultraviolet region; therefore, photolithography is usually carried out in a special yellow light clean room. The yellow light source interacts with the photoresist to a minimum extent.

3.2.1 Photolithography process sequence

Photolithography pattering, more or less, is completed in the sequence given by figure (3.2.1). Some steps or procedures may need modification depending on the needs of the user. The sequence in figure (3.2.1) is briefly explored in the following section.

Substrate Preparation

The first step of any micro and nanofabrication technique is to prepare the substrate to undergo a certain cleaning procedure. Furthermore, the substrate may require the application of adhesion agents before coating them with a particular resist, depending on the type of resist being used. Photolithography demands very high requirements of cleanliness for a substrate while making initial preparations. If the substrate is not cleaned properly, foreign particles present will result in errors while transferring the patterns. Similarly, surface contamination will create unwanted adhesion issues for the photoresist.

There are a variety of ways to clean substrates. The most basic cleaning procedure for new substrates involves the use of acetone or methyl chloride to remove grease followed by a methanol or isopropyl alcohol rinse and an optional distilled water rinse. Sometimes the substrates may also be put into an ultrasonic bath sonicator during the rinsing process if the particles appear very obstinate. An alternative cleaning procedure, a very aggressive one, for cleaning new substrates involves the use of acidic agents. A very commonly used acidic solution to clean new substrates is called *Piranha solution*, also known as *Piranha etch*. Piranha etch is a solution of sulfuric acid (H_2SO_4) and hydrogen peroxide (H_2O_2) in a 3:1 proportion. Piranha etch is a very strong oxidizing agent capable of dissolving almost all organic impurities; thus, the use of this solution requires special care in a laboratory.

The cleaned substrates may require further treatment before applying photoresist on them. Photoresists should properly adhere to the substrate before patterning anything on them. Typical photoresists are hydrophobic (water repelling) and they require a similar hydrophobic substrate surface to promote sufficient adhesion. If a substrate shows signs of insufficient photoresist adhesion, *hexamethyldisilazane* (HMDS) can be applied to the substrate to convert the hydrophilic (bonding with water) surface to hydrophobic. The process to promote adhesion typically is carried out in

two steps: dehydration and applying HDMS. The dehydration step is completed by heating the substrate to a temperature of $(100 - 200)°C$. The adhesion promoting agent, HDMS, is applied to the dry substrate via liquid priming or vapor priming. Spin coaters are used for liquid priming, whereas vapor priming ovens are used for vapor priming.[24]

Photoresist Application

A spin coater is typically used to coat or deposit photoresist on top of a substrate. Different spin configurations can be set on a spin coater to coat photoresists of different thicknesses. After dispensing a few milliliters of photoresist on a substrate, the substrate is gradually spun to a target spin speed which is held for a short process time of approximately 30-40 seconds before bringing it to a halt. The spin coater generates a photoresist film of uniform thickness on almost all regions of the substrate if done correctly. An edge bead forms on the edges of the substrate while spin coating the substrate. If needed, edge beads can be removed by applying a solvent on a slowly rotating substrate on a spin coater. There are other alternatives for applying photoresist such as spray coating and deposition by electrophoresis; however, the most common technique is spin coating.

Softbake

Photoresist film, after spin coating, may develop built-in stress resulting from shear during the spinning process. Such film stresses can be reduced by heating the film to a particular temperature; this intermediate step of heating a substrate with film on it is called *softbake* or *prebake*. Annealing the film also helps to remove residual solvents from the surface and minimizes the contamination of the photomask by inhibiting the sticky behavior of resist. A hotplate or an oven is used for this step.

Mask Alignment and Exposure

Device fabrication on micro and nano scales is done in several multiple cycles, creating layers on top of each other. Creating an accurate multi-layered structure requires precise alignment between a mask and a substrate; therefore, a lithography tool should be equipped with an accurate mask alignment feature together with an exposure feature.

There are different sorts of lithography tools; their design differs from each other

based on exposure techniques. There are three kinds of exposure techniques in photolithography: contact, proximity, and projection. The main ideas of the different exposure techniques are presented in figure (3.2.2).

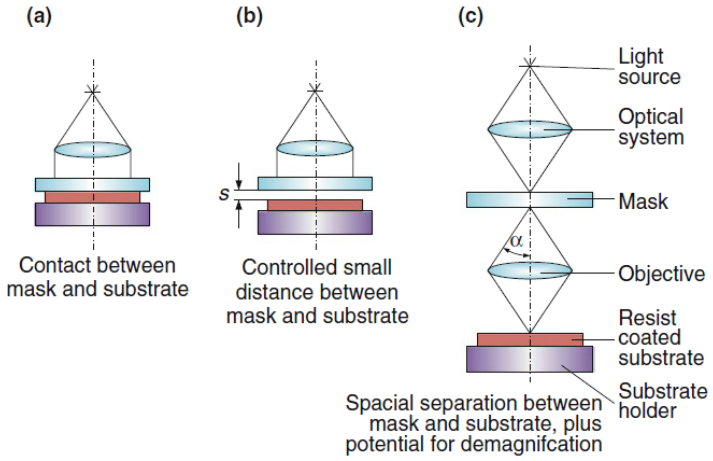

[24]

Figure 3.2.2: Different types of exposure techniques in photolithography. **a)** Contact exposure, **b)** Proximity exposure, **c)** Projection exposure.

In contact exposure, the photomask touches (makes contact with) the substrate during exposure; exposure is done by shining parallel light on the mask to project a shadow on the substrate. Proximity exposure is similar to contact exposure but the photomask in proximity exposure does not make contact with the substrate. In this technique, exposure is performed with a particular gap between the substrate and the mask to reduce the chances of damage to the photomask. The lithography tool used for contact and proximity exposure is called a *mask aligner*. Projection exposure is achieved by using lenses to project the image of a photomask onto a substrate (coated with photoresist) at a distance. Mask in projection exposure is usually referred to as a *reticle*. A reticle differs from a full field photomask based on the information engulfed in it. A photomask contains the entire pattern of a single layer of a full wafer; on the other hand, a reticle consists of a single-layer pattern that only covers a small portion of the wafer.[24] A reticle has to be stepped and patterned several times to expose the entire wafer. The lithography tool to achieve projection exposure is called a *stepper* or a *scanner*.

A mask alignment process is an important step in photolithography. The mask align-

ment process requires alignment markers (also known as *fiducials*) to properly stack layers on top of each other. Alignment markers are created on the substrate together with the pattern of interest while making the first or initial layer. The already present alignment markers on the substrate are then matched with the corresponding alignment markers on the mask to fabricate the next layer structures. Similarly, new alignment markers are fabricated while patterning the second layer if the third layer is to be stacked on top of the existing one. For mask alignment, some systems may adjust the position of the mask while others may adjust the position of the substrate by shifting (in x and y direction) and rotating (by an angle θ) the corresponding part.

Exposure is carried out after a successful mask alignment. The most common light source used in photolithography is a high-pressure mercury vapor lamp. It produces high intensity light in the ultraviolet (UV) region. Figure (3.2.3) shows a typical high-pressure mercury arc spectrum. The light intensity peaks of interest in figure

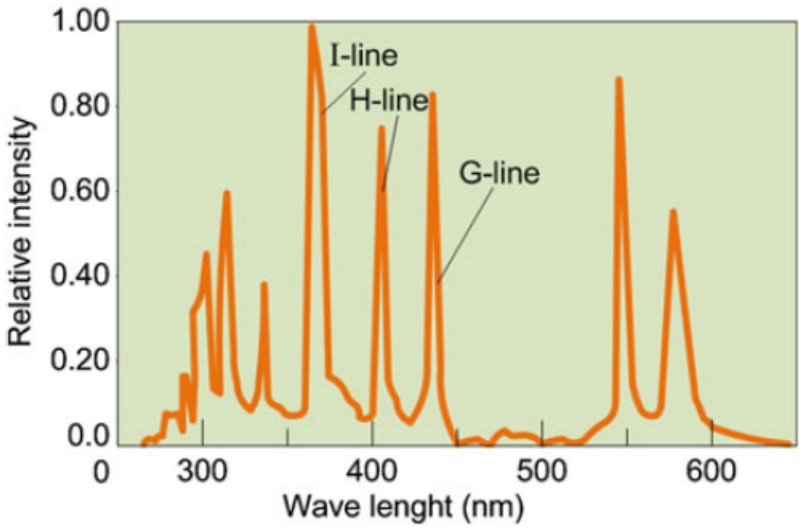

[24]

Figure 3.2.3: Typical high-pressure Hg arc spectrum

(3.2.3) are located at 435nm (called G-line), 410nm (called H-line), and 365nm (called I-line). Among them, the most commonly used line is the I-line.

Pattern Development

The exposed section of the photoresist has to be processed appropriately to convert the photoresist into usable three-dimensional structures; this final pattern producing step is called development. Pattern development requires a developing agent (developer) to complete this process. Most developing agents are typically aqueous alkaline solutions. The exposed area of a positive photoresist or the unexposed area of a negative photoresist is washed away by the developing agent during development. There are three different ways of developing patterns in photolithography; they are spray, puddle, and immersion development.

For spray development, the developer is sprayed on top of an exposed photoresist through a nozzle while spinning the substrate at a moderate speed. During puddle development, the developer is dispersed on an exposed substrate while gently spinning the substrate. In puddle development, the surface tension of the applied developer forms a puddle on the substrate surface. Both spray and puddle development, use fresh developers throughout the development process. During immersion development, the exposed substrate is simply immersed in a developer and agitated gently to develop the final pattern. One has to ensure that the developer is not extremely diluted during immersion development to get the best result.

The developed patterns have to be washed with deionized water to stop further development and wash developer residues from the substrate. The developed patterns can also be post-baked to an appropriate temperature–ensuring that the temperature does not exceed the melting point of the photoresist–to remove residual solvents and anneal the film.

3.2.2 Photolithography hardware and materials used

The lithography tool used for device fabrication in our study is an *OAI 804 MBA contact aligner*; it is semi-automated, equipped with four cameras, and an optical front and backside mask aligner. The printing modes available in the system are proximity, soft, hard, and vacuum. The resolution that can be achieved during soft

contact is less than $2\mu m$; furthermore, the resolution increases to a sub-micron level during hard contact. The system makes use of vacuum suction to hold the substrate and mask into place. The UV light source used in the system is a Hg-Arc lamp calibrated at an intensity of $13.3mW/cm^2$. The dimension of a mask accepted by the system is $5'' \times 5'' \times (0.065 - 0.1)''$.

The photoresists used in the fabrication procedure are Microchem LOR2A and Microposit S1805. Microchem LOR2A is used while making bi-layer resist films as an under-layer because of its good adhesive properties with semiconductors. Microposit S1805 is a positive photoresist that can be used in single or bi-layer resist films. The thickness of the films, LOR2A and S1805, is varied by spinning the films at a particular spin rate using a spin coater. The developing agent used for the photoresists is a Microposit MF-319 developer. MF-319 developer works well when coupled together with S1800 photoresists.

3.3 Fabrication steps and overview

This section discusses the steps and procedures undertaken for pattering our structures of interest starting from the very beginning. Device fabrication was performed using photolithography and sputtering techniques; however, there were a few other issues that needed consideration before fabricating our structures of interest. All steps taken during the fabrication procedure will be discussed in this section.

3.3.1 Substrate selection and preparation

The first step of fabricating any microstructures is to select a suitable substrate, depending on the functionality of the device to be synthesized. A substrate acts as a support structure for the layers and device to be fabricated. To fabricate the best uniform structures, a substrate must have a good surface finish, few crystal defects (high degree of crystalline perfection), and good thermal conductivity. The most common substrates in the electronic industry are semiconductors, particularly silicon. In addition to semiconductor materials, glass substrates are also used in the fabrication of microstructures. Glass substrates are particularly useful when final micro-devices have transparency and high chemical stability needs. The most common type of glass substrate used in micro-device fabrication is borosilicate glass. In our study, devices

were fabricated on pieces of a silicon wafer (with silicon dioxide on top) and borosilicate glass.

Silicon wafers were diced and coverslips (borosilicate glass) were cut into small rectangular pieces before cleaning them. The cleaning procedure was carried out by dipping the substrates into an acetone bath, followed by an isopropyl alcohol (IPA) bath, followed by a distilled water bath; sonication is used sometimes during the acetone and IPA baths. The washed substrate is then blow dried using clean compressed air; afterward, the substrate is heated above $100°C$ on a hot plate to remove the residual solvents. All cleaning procedures are performed on a wet bench inside a clean room.

3.3.2 Spin coating

Spin coating was used to coat the substrate with photoresist in our project. The spin-coating tool used for coating the photoresist was *Laurell Ws-400B-6NPP/LITE*. The fresh photoresist was administered on top of a clean substrate through a pipette. The spinning process was completed in 3 stages. The first stage involved an initial spread process where the substrate is gently rotated with an acceleration of 100 rmp (rounds per minute) for 5s reaching 500 rmp at the end of the stage. The purpose of the initial spread process is to distribute the centrally administered resist to an almost whole section of the substrate. The second stage involves rapidly accelerating the substrate to a designated spin speed and holding it for a total of 40-45 seconds at the particular spin speed. The second stage creates a uniform film of the photoresist on top of the substrate. Film thickness varies with the spin speed and their relationship (spin curve) can be found on the data sheet of the used photoresist. In our case, a spin speed of 5000rpm was used to acquire an S1805 film thickness of approximately 400nm. During the third stage, the substrate is decelerated gently to a halt. Gently decelerating the substrate helps to maintain the uniformity of the film.

The coated substrate is usually heated on an oven or hotplate, immediately after the spin coating process, in a process called soft-bake. The substrate is soft-baked on a hotplate for 2-5 min at a specific temperature, depending on the type of photoresist used. In our study, S1805 films were soft-baked at $115°C$ for 2 minutes, while the LOR2A films were heated to $180°C$ for 5 minutes following the spin-coating process. The purpose of soft-bake is to evaporate the solvent present making the photoresist

more solid and uniform. The soft-baking process changes the thickness of the photoresist slightly, and it prepares the film to be exposed to UV light. The substrate is allowed to cool and settle down for 5-10 min before taking it to the lithography tool.

3.3.3 Exposure and Development

The coated substrate was transferred to a mask aligner, *OAI 804 MBA contact aligner*, to expose patterns onto it. Our mask aligner requires the substrate to be a 4" wafer; if a smaller substrate is to be used, it has to be put on top of an existing wafer. After putting the substrate on top of the wafer, the stage of the aligner, containing the substrate, was carefully aligned with alignment markers (when applicable) and moved to contact position with the mask for exposure.

Exposure time in photolithography depends on a number of factors such as the photoresist used, the thickness of the resist, and the wavelength of the light from the UV source. Exposure time can be calculated by dividing the intensity of the UV source by the exposure dose required at a particular resist thickness; the exposure dose vs. resist thickness curve can be found on the datasheet of the photoresist used. The calculated exposure time can only be used as a starting point for a trial and error method of developing a custom recipe for the combination of materials and tools used in a particular laboratory. In our study, the same trial and error method was used to develop a working recipe for the fabrication process. A complete working recipe is available in the appendix section of this thesis.

In our fabrication process, the exposure times used were 2s, 6.5s, and 12s depending on the combination of substrate, photoresist, and developer used. The exposed resist was then developed using *MF-319* developer using immersion developing technique. The developed substrate was then washed with distilled water to stop the developing process. Compressed clean air was used to dry the final patterned substrate which is then carried into a sputtering chamber to deposit materials on the patterns.

3.3.4 Material deposition and Lift-off

Our fabrication technique uses photolithography to make patterns and employs a sputtering system to grow structures on the existing patterns. The developed patterns are filled with sputtered atoms to grow layers of ultra-thin films. Our sputtering

system is a multi-target (4 cathodes) sputtering system from *MANTIS*. The system parameters and conditions used while growing different layers of the specific structure are discussed in the experimental section.

The final step of our fabrication process is lift-off; it is carried out after material deposition. The substrate with deposited material is immersed in an acetone bath, which is agitated gently by stirring the solvent. It was noted that the sonication process, despite being effective, damages films and structures; thus it is strongly discouraged. A mixture of agitation technique and relaxation time allows the photoresist to be stripped from the substrate, leaving only the structure of interest on top of the substrate. The substrate is then washed with IPA followed by distilled water; compressed air is used at the end to dry the solvents from the fabricated structures. The same process is repeated from the beginning while fabricating multi-layer structures.

3.3.5 Thickness Calibration

In our study, film thicknesses play an important role, either to induce PMA in CoFeB films or to acquire the $\beta - W$ phase in W films; therefore, we want the thickness of our fabricated device to be as precise as we can make. Our sputtering system uses a quartz crystal microbalance (QCM) to measure the thickness of the film grown. The QCM quantifies the thickness variation by measuring the change in the resonant frequency of the quartz crystal. The thickness measurement relies on the material parameters of the target used and the position of the sputtering head. In experiments where the thickness parameter is very significant, certain calibration is required to correctly adjust the value reported by the QCM; such calibration is allowed in our sputtering system through the use of *tooling factor (TF)*. Correctly adjusting the tooling factor for a cathode target allows us to acquire a precise thickness for every recurring film deposition.

The procedure to adjust the tooling factor requires the fabrication of a film or pattern of anticipated thickness at a pre-defined tooling factor. Afterward, the actual thickness of the fabricated film or pattern is measured by a Profilometer or Atomic Force Microscope (AFM). In our study, we used a Profilometer to quantify the thickness of the fabricated pattern. The tooling factor is then adjusted to a new correct value

using the relationship given by equation (3.1).

$$Actual\ TF = Initial\ TF \times \frac{Thickness\ measured}{Thickness\ QCM} \tag{3.1}$$

The calibration procedure can be repeated an additional time if the thickness criteria are very important. The adjusted tooling factor works for all future deposition while using the calibrated target from the particular cathode position. All target materials used in our study were first calibrated properly before using them to make films and structures.

3.4 Fabricated samples

The experimentation in our project mainly made use of two different kinds of sample geometry: a cloverleaf pattern and a Hall structure with contact pads. The cloverleaf pattern is used for sheet resistance measurement while implementing Van der Pauw's method; the Hall structures are used to study the inherent magnetization of the ferromagnetic films. Despite making several samples with different compositions of material, the structure geometry and dimensions are always kept constant. The structures are fabricated using photolithography and the fabricated structures' uniformity is acquired through a dedicated photomask (ordered from the **4D LABS core facility at SFU**). The images of the two types of structures alongside their respective drawings with corresponding dimensions are given in figure (3.4.1).
Both structures in figure (3.4.1) are symmetric along the x and y axis, excluding the alignment markers of the Hall sample. The images of the fabricated structures, 3MgO/2CoFeB/6W Hall structure and 3MgO/6W cloverleaf pattern, are included in figure (3.4.1a) and (3.4.1c); drawings of the corresponding structures with dimensions are given in figure (3.4.1b) and (3.4.1d), respectively. Similar patterns are fabricated with different layer attributes while conducting the experiments.

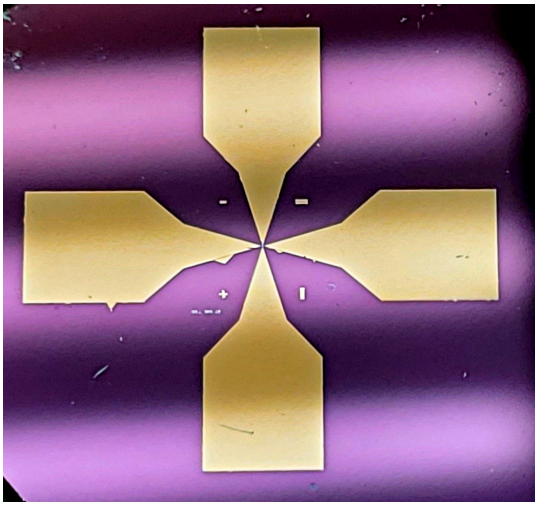

(a)

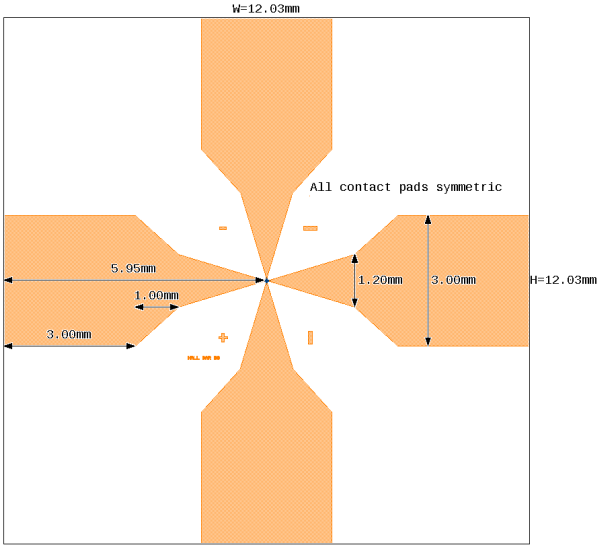

(b)

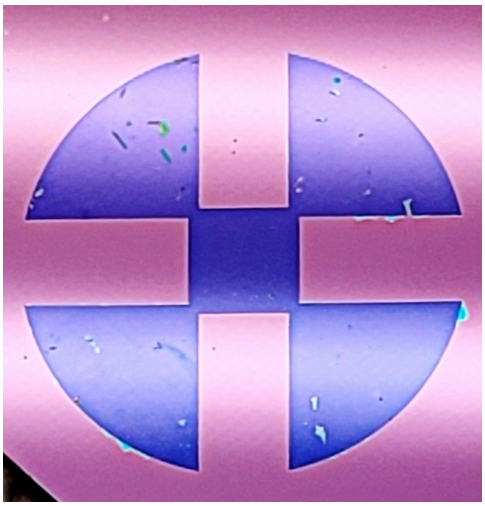

(c)

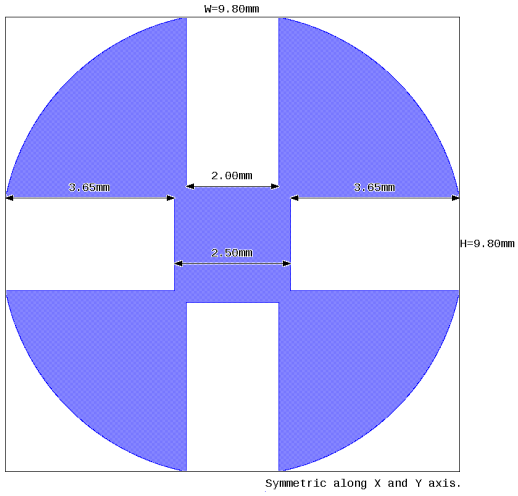

(d)

Figure 3.4.1: Images of micro-structures used in the experiment. Figure **a)** shows a picture of a fabricated Hall structure (3MgO/2CoFeB/6W) with contact pads on a silicon substrate(SiO_2 on top). Figure **b)** shows a drawing of the Hall structure given in **(a)** with dimensions. Figure **c)** shows an image of a test cloverleaf pattern of 3MgO/6W on a silicon substrate(SiO_2 on top). Figure **d)** illustrates a drawing of the cloverleaf pattern shown in **(c)** with dimensions.

Chapter 4

Experimental Work

4.1 Sheet resistance

The resistance of thin conductive films of uniform thickness is called sheet resistance. There are several methods, contact, and contact-less techniques, to measure sheet resistance. One of the most popular techniques to characterize the electrical properties of thin films is Van der Pauw's method. The method was developed by Van der Pauw in 1958 [28] to measure resistivity and Hall coefficient of samples of arbitrary shapes. The method makes use of four-point probes; out of which, it uses two contact points to apply current across the sample and the other two to measure the voltage drop between the remaining contact points.

Although the aforementioned method appears very powerful, as it does not depend on the shape of the sample, some caveats must be met to obtain accurate results. The method requires that the sample of interest should be flat and of uniform thickness, any isolated holes should not be present in the sample, and the sample should be completely isotropic and homogeneous. Furthermore, the contact points must be located at the edge of the sample and their contact area must be smaller, at least an order, than the area of the entire sample.

Every measurement has its sources of uncertainties and errors. Even if all of the conditions of the Van der Waal method are met, which is very difficult in an actual experiment, the result of the method will still have some uncertainties associated with it. The shape and size of the sample can influence the final magnitude of the error.

Similarly, the position and the size of the electrical contacts of the setup can also cause the error values to differ. The most commonly used shapes of the sample while determining the resistivity of a sample using the Van der Pauw (VDP) method are given in figure (4.1.1)

It has been shown that the errors arising from the measurement method can be minimized by using the cloverleaf technique [28]; the cloverleaf geometry is illustrated in figure (4.1.1a). The square sample, with sufficiently longer edges and smaller contact points at the corners, as depicted in figure (4.1.1b), also has been found to minimize the error and give reliable outcome [29]. The contact points setups as shown in the figure (4.1.1c) are not recommended and are speculated to have greater error.

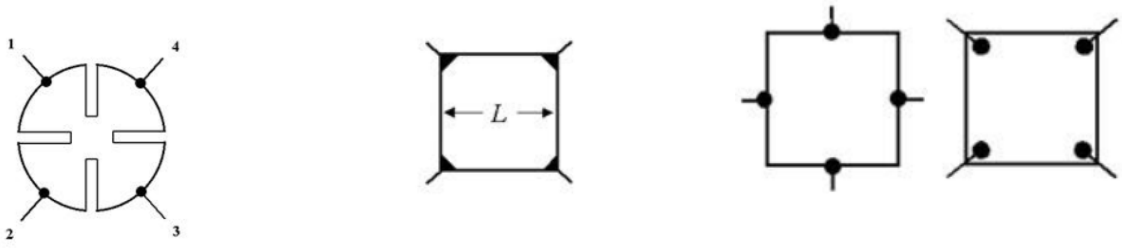

(a) Cloverleaf

(b) Square with contacts at corners

(c) Square with contacts at the edges or inside the sample

Figure 4.1.1: Sample shape and geometry used for Van der Pauw's method.

4.1.1 Fabrication and setup

In our study, we use the Van der Pauw method to measure the sheet resistance of Tungsten films. The primary objective of this section is to find the thickness criteria for acquiring β-tungsten. Tungsten thin films exhibit a body-centered cubic $\alpha - W$ structure in bulk; however, they exhibit a close-packed A15 $\beta - W$ phase as the thickness of the film reduces. This $\beta - W$ state is of particular interest to us because of its giant spin Hall effect which in turn produces large spin-orbit torques.

The device geometries we use in our method are cloverleaf pattern (as illustrated in figure (4.1.1a)) and square pattern with contacts at the corners (as depicted in figure (4.1.1b)). The cloverleaf pattern is fabricated using photolithography. The square pattern, on the other hand, is made on top of a square substrate, eliminating the need

for lithography. The thin films are grown on a borosilicate glass or a silicone substrate with SiO_2 on top. A Titanium adhesion layer is used between the substrate and the thin film to promote the adhesive quality of the grown film. Sputter deposition is used to grow thin films on top of the substrates. Sputter deposition parameters are kept uniform while growing the thin films of interest.

A *2450 Keithley Source Measure Unit (SMU)* is used to source current and measure voltages during the measurement procedure. To make precise contacts, micromanipulator probes are used in the measurement setup. The probe heads are carefully positioned at the edges of the fabricated films complying with the configuration of the figure (4.1.1a) and figure (4.1.1b), before doing any measurements.

4.1.2 Measurement and calculation

Prior to calculating the average resistivity of a sample, the sheet resistance must be obtained first. The average resistance of thin film (ρ) is related to the sheet resistance (R_s) by $\rho = R_S.t$, where t is the thickness of the film. To calculate sheet resistance, the resistance of the thin film must be calculated using Ohm's law by using the measured voltage drop and the applied current values across the contact points. An example resistance label and how it can be calculated is given in equation (4.1).

$$R_{12,34} = \frac{V_{34}}{I_{12}}, \tag{4.1}$$

where label $R_{12,34}$ represents the resistance value obtained while applying current from terminal 1 to 2, i.e. I_{12}, and measuring voltage drop between terminal 3 and 4, i.e. V_{34}.[30] The numbering of contact points is similar to the configuration shown in the cloverleaf pattern of the figure (4.1.1a). The accuracy of the measurement can be improved by including the reciprocal and reversed polarity measurements. A reciprocal measurement to an existing measurement $R_{12,34}$ refers to measuring $R_{34,12}$ where the current and voltage channels are swapped. Similarly, a reversed polarity measurement to an existing measurement $R_{12,34}$ is determining $R_{21,43}$ where the direction of the current and voltage drop is reversed. Combining all the results of these

measurements and averaging them will yield:

$$R_v = \frac{R_{12,34} + R_{21,43} + R_{34,12} + R_{43,21}}{4} \tag{4.2}$$

and

$$R_h = \frac{R_{23,41} + R_{32,14} + R_{41,23} + R_{14,32}}{4} \tag{4.3}$$

The vertical resistance value obtained in equation (4.2) and horizontal resistance value obtained in equation (4.3) can then be used to solve the Van der Pauw equation [30]:

$$e^{\frac{-\pi R_v}{R_s}} + e^{\frac{-\pi R_h}{R_s}} = 1 \tag{4.4}$$

Numerical methods can be used to solve for the sheet resistance of the sample using equation (4.4). One such simple numerical method that converges quickly is the Newton-Raphson method. The Newton-Raphson method approximates the root of a real-valued function through an iterative process until the convergence criterion is met. The iterative algorithm employed to acquire the root of the equation (4.4) is expressed in equation (4.5).

$${R_s}^+ = R_s + {R_s}^2 \, \frac{1 - S^{R_v} - S^{R_h}}{\pi \left(R_v S^{R_v} + R_h S^{R_h}\right)} \tag{4.5}$$

Here, R_s^+ represents the n^{th} sheet resistance approximation term while R_s represents the preceding $(n-1)^{th}$ sheet resistance approximation term in the iteration. A substitution of variable with $S = e^{\frac{-\pi}{R_s}}$ has been done in equation (4.5) for simplicity.

4.1.3 Result and Analysis

The measured values R_v and R_h are inserted into the equation (4.5) and the algorithm is iterated, with an initial guess value, until the resistance value converges. The resultant value is then multiplied by the thickness of the film to obtain the resistivity of the film at that particular thickness. The result of the sheet resistance measurement, using the Van der Pauw technique, is summarized in figure (4.1.2).

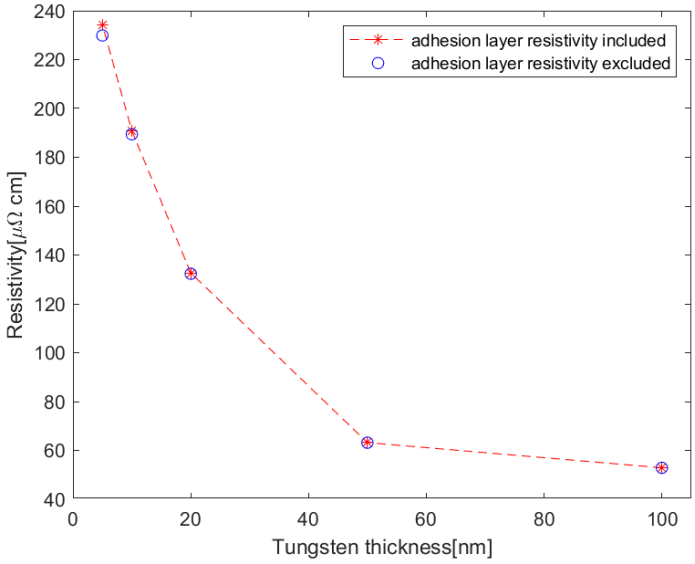

Figure 4.1.2: Resistivity of Tungsten films obtained using Van der Pauw 4-point measurement technique.

The resistivity trend in figure (4.1.2) shows an increasing pattern with the reduction of thickness. The resistivity of the underlying 5nm titanium adhesion layer is also taken into account in the analysis as seen in the figure. Tungsten films can be seen to have the usual resistivity values of $(50-65)\mu\Omega cm$ at the thickness range of (100-50)nm; the resistivity value suggests the presence of $\alpha - W$ at these thicknesses. The resistivity of tungsten film increases suddenly to $132\mu\Omega cm$ at 20nm thickness suggesting the presence of a mixture of $\alpha - W$ and $\beta - W$ states. The resistivity further increases to $(190-230)\mu\Omega cm$ in the thickness range of (10-5)nm; such high resistivity of tungsten films suggests the presence of $\beta - W$ state at the corresponding thicknesses.[31] Therefore, we will use tungsten films with thicknesses less than 10nm as a source of SOT in our SOT experiments, as it shows signs of the required $\beta - W$ behavior having a large spin Hall angle.

4.2 Magnetic measurements

There are several ways to probe the magnetization components of a magnetic material; some of the most common techniques are Magneto-Optical Kerr Effect (MOKE), Vibrating Sample Magnetometry (VSM), SQUID Magnetometry, Kerr Microscopy and Magnetic Force Microscopy (MFM). The mentioned techniques, among others, help to

characterize magnetic materials providing information about the strength and orientation of magnetization, coercivity, retentivity, saturation, anisotropy, and other useful features of the magnetic system.[32] Each method has its advantages and limitations while implementing them. Our experiment focuses on studying out-of-plane magnetization components during the application of current. Studying current-induced changes in magnetization, especially out-of-plane components, will be easier if the measurement technique already makes use of the current applied to the sample. One such simple measurement technique that directly integrates the use of current to study the strength and direction of out-of-plane magnetization components is the anomalous hall effect (AHE) based measurement technique.

4.2.1 Measurement Principle and Configuration

AHE-based measurement technique employs a Hall bar to detect and quantify anomalous Hall effect. The AHE arises when a current flows through a ferromagnetic material that possesses a net magnetization; AHE is different from the ordinary Hall effect that arises in non-magnetic conductors. As the current is applied across a ferromagnetic sample, the inherently present field due to the presence of magnetization influences the drifting electrons. The presence of the additional intrinsic field together with any external applied field collectively gives rise to the Lorentz force that acts on the electrons drifting in a perpendicular direction to the field. As a result, the electrons are scattered and deflected to one side of the sample, giving rise to a transverse voltage across the material, known as the Hall voltage.

The AHE measurement is typically performed using a Hall bar geometry, which consists of a narrow and rectangular-shaped sample with electrical contacts placed at opposite edges. Current is passed through the sample, and the Hall voltage is measured across the perpendicular edges using voltage probes. The Hall voltage is directly proportional to the strength of the magnetic field and the magnitude of the current. The out-of-plane component of the magnetization of the sample correlates directly to the measured Hall voltage. The sign of the Hall voltage provides information about the polarity of the magnetization, while the magnitude of the voltage is related to the strength of the magnetization.

Since the Hall voltage depends on the geometry of the Hall bar employed in the setup and configuration of measuring equipment. We will cover the geometries and measurement configuration used in our experiment briefly.

Hall bar geometry

Hall bar geometry differs from one experiment to another depending on the measurement setup and requirements. Different Hall bar geometries have different numbers of contact points to measure voltage components across the longitudinal current arms. The simplest form of Hall bar geometry is a 4-contact Hall bar geometry where opposite ends of longitudinal wider arms are used to source current and opposite ends of transversal narrower arms are used to measure generated Hall voltage. Hall bar geometries with a higher number of contact points such as 6- and 8-contact Hall bars are used to measure additional voltage components across the wider longitudinal current arms. Such Hall bar geometries are used in experiments where voltage differences in both directions–transverse (V_{xy}) and longitudinal (V_{xx})–are of interest. Figure(4.2.1) shows sample images of 4-point and 6-point Hall bar geometries.

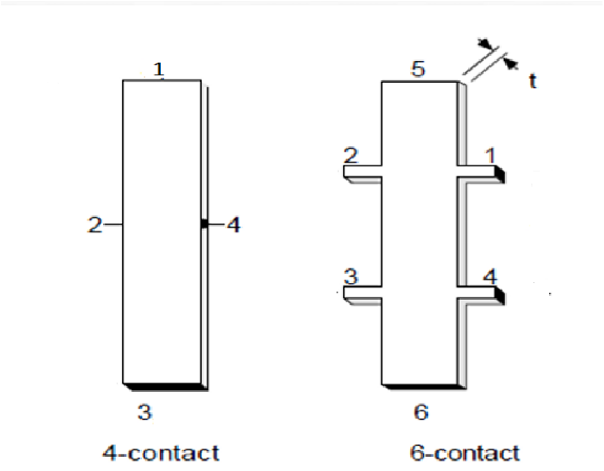

Figure 4.2.1: Sketches of Hall bars showing a 4-point Hall bar geometry (left) and 6-point Hall bar geometry (right)

In our experiment, we have employed the simplest form of the Hall bar, i.e. 4-point Hall bar geometry. The length of all four arms of our Hall bar is equal and the width of all the arms is the same. The Hall bar appears symmetric with a uniform width when patterned on the substrate. The entire Hall pattern was fabricated by stacking

layers on top of each other using photolithography. The geometry and dimensions of one of the fabricated Hall bars of our experiment are illustrated in figure (4.2.2).

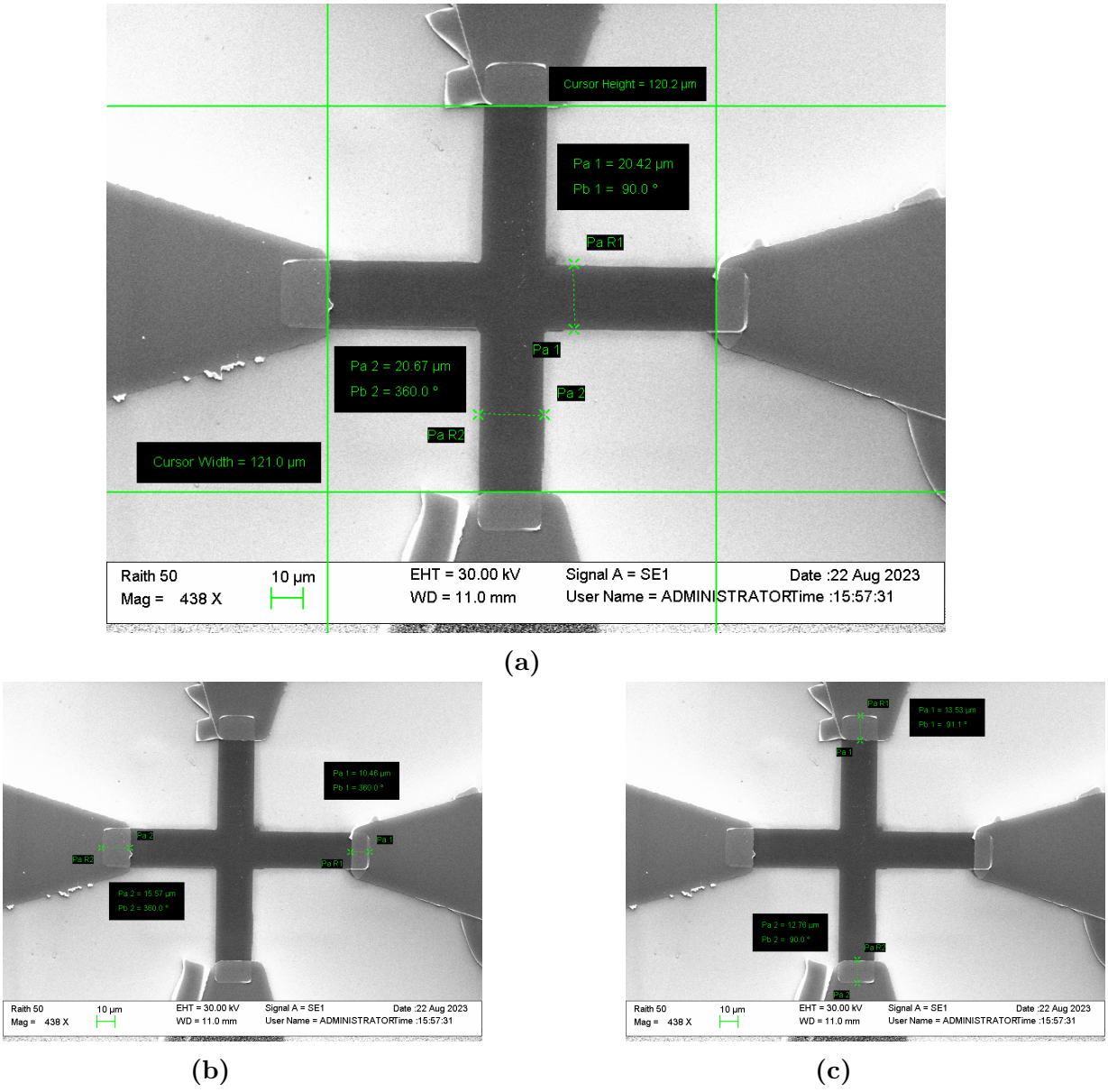

Figure 4.2.2: Images of 3MgO/5CoFeB/6W Hall bar captured using an SEM. Figure **a)** includes the overall dimensions of the Hall structure measured using the SEM. Figure **b)** and figure **c)** show the information about the horizontal and the vertical overlap regions of the main Hall structure with the contact pads, respectively.

The geometry and dimensions of the sample Hall structure (3MgO/5CoFeB/6W), portrayed by images in figure (4.2.2), are captured using a scanning electron microscope (SEM). The dimensions and annotations in the images of figure (4.2.2) are

directly obtained from the SEM; moreover, the dimensions of the fabricated Hall structure can be seen to correspond directly to the model Hall structure of figure (2.0.1b), used in simulations. The information about the overlap region between the contact pads and the Hall structure can be seen in figures (4.2.2b) and (4.2.2c); the overlap region falls within the range of $(10-15)\mu m$. All the Hall structures discussed in this project share the same geometry and approximate dimensions as shown as in the figure (4.2.2).

Measurement Configuration

AHE measurement technique requires two separate channels: one to source current and the other to measure the voltage across the Hall bar. While sourcing a constant current, source meter or current source generates a uniform voltage difference across the terminals; the voltage difference between the terminals is generated based on the resistance of the load being used. The simultaneous measurement of voltage while sourcing specific current through the Hall bar terminals may result in an unwanted flow of current from voltage terminals, due to the potential difference generated by the current source at current terminals. In our experimental configuration, we have addressed this issue by attaching a $100k\Omega$ resistor across each voltage arm before connecting them to the voltmeter. In doing so, the unwanted flow of current from voltage terminals is shunted in the Hall bar structure. Schematics of our measurement configuration are illustrated in figure(4.2.3b).

A terminating 50Ω resistor can also be seen in parallel to the current source in figure (4.2.3b); the purpose of the terminating resistor is to match the impedance between the current source and the fabricated sample to reduce signal reflection when short current pulses are used. The resistive elements, including the fabricated Hall structure, are all connected to each other using a circuit board. Our custom circuit board is equipped with an area with big contact pads, matching the size of our fabricated structure, such that the Hall structure can be directly attached to the circuit board. To attach the sample (on the substrate) to the circuit board, we make use of *8331D Silver Conductive Epoxy Adhesive* from *MG Chemicals*. The use of epoxy makes the arrangement easy, sturdy, and robust; it also improves the quality of the signal when short current pulses are used. A depiction of the final Hall structure affixed to our custom circuit board is illustrated in figure (4.2.3a). Conductive epoxy can be seen

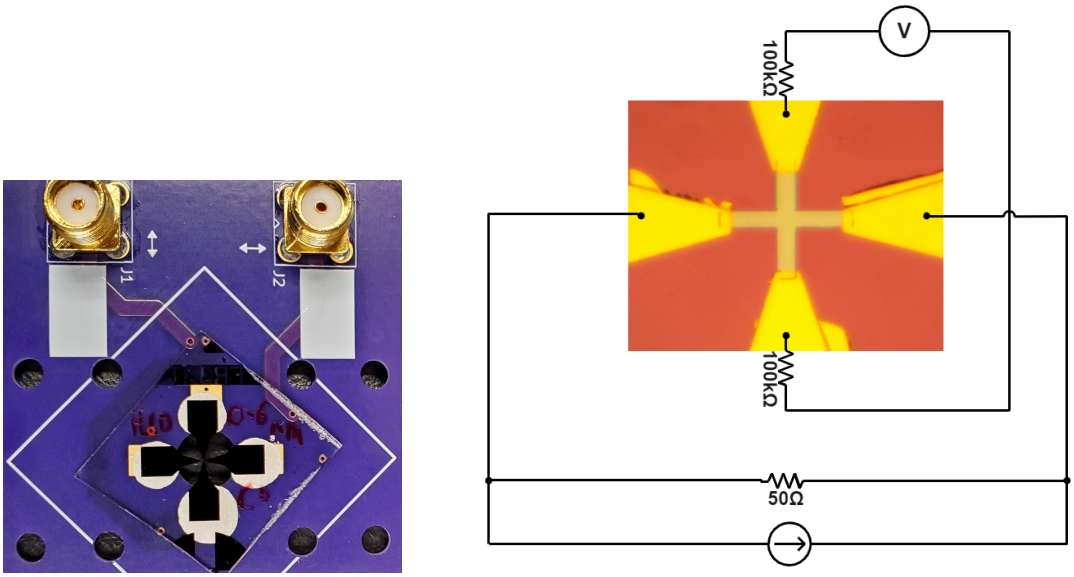

(a) **(b)**

Figure 4.2.3: Schematics of measurement configuration employed for detecting Hall signals. Figure **a)** shows the Hall structure–on a glass substrate–attached to the circuit board using conductive adhesive epoxy. Figure **b)** shows the elements of the measurement configuration.

through the glass substrate bonding the sample structure to the pads of the circuit board. The circuit board containing the Hall structure is attached to a mount and the mount is placed onto a stage, capable of rotating on its axis, inside an electromagnet. BNC cables are then used to connect the source meter unit to the circuit board.

4.2.2 Hall measurements on cobalt films

The interest of our research revolves around magnetic thin films with out-of-plane anisotropy; particularly, films with perpendicular magnetic anisotropy (PMA). Cobalt films have in-plane anisotropy when the thickness of the film is above 1nm; however, the anisotropy of cobalt films changes as the thickness of the films is reduced below 1nm. A good quality ultra-thin (thickness below 1nm) cobalt film can show strong signs of PMA [23]. Acknowledging the thickness criteria of the cobalt films for inducing PMA, we fabricated Hall structures with ultra-thin cobalt films.

Film fabrication parameters

Hall structures with different thicknesses of cobalt films were made and corresponding Hall measurements were done to study the inherent anisotropy of the films. The conditions used in the fabrication of films to make the Hall structures are summarized in Table(4.2.1).

Table 4.2.1: Parameters used to fabricate the Hall structure comprising Co films.

Sputter parameters	Layer attribute		
	Mgo	Co	W
Base chamber pressure (Vacuum)	$5.5 \times 10^{-5} mbar$	$4.5 \times 10^{-5} mbar$	$4.0 \times 10^{-5} mbar$
Thickness	$4nm$	$0.4nm/0.6nm/1.0nm$	$4nm$
Rate of deposition	$0.0424 \mathring{A}/s$	$0.200 \mathring{A}/s$ $/0.165 \mathring{A}/s$ $/0.165 \mathring{A}/s$	$0.267 \mathring{A}/s$
Argon flow rate	$15.0 sccm$	$15.0 sccm$ / $30.0 sccm$ / $30.0 sccm$	$10.0 sccm$

The table (4.2.1) summarizes some of the important parameters used in the making of the corresponding stack of films. The Hall structures were fabricated by stacking MgO film, Co film, and W film respectively on top of the surface of a Borosilicate glass substrate; the Hall structures were patterned using the optical lithography technique. The quality of the film heavily depends on the criteria and conditions used during the fabrication process, fine-tuning all these parameters to acquire a superior quality of film is an extensive process and it has not been explored in our study.

Result and Analysis

The fabricated Hall structure for different thicknesses was each configured accordingly for our measurement setup. The primary aim of the experiment was to study the anisotropy of the cobalt films by measuring the Hall voltage developed across the vertical voltage arms of the Hall structure while passing a steady flow of current through the horizontal current arms under the influence of a perfect out-of-plane magnetic field. Figure (4.2.4) shows a comparison between the Hall signal obtained

from three different thickness criteria of the cobalt films.

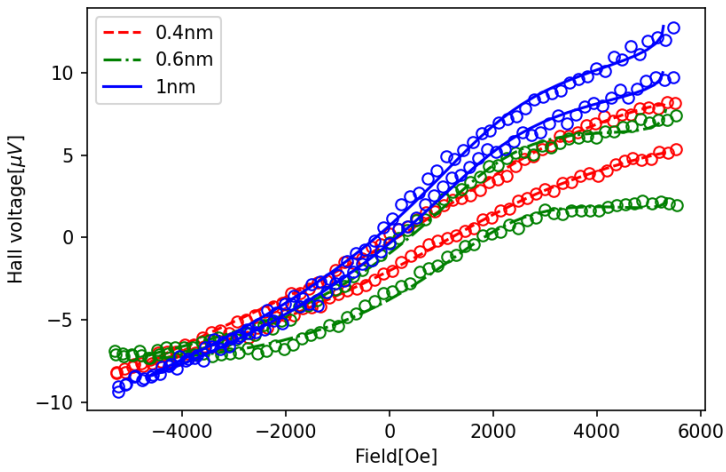

Figure 4.2.4: Signal obtained from different cobalt films using the Hall bar measurement setup when an out-of-plane field is applied across the plane of the fabricated Hall structure.

The result summarized in figure(4.2.4) is the outcome of several averaging steps. The Hall voltage at each field value–denoted by the open circles in the figure(4.2.4)–was measured 20 times before integrating them into a final value; similarly, the whole sweep cycle between maximum field value and minimum field value was allowed to run for 3 separate cycles before amalgamating them into a final outcome. In our measurement setup, a stall time of 3.0s was used while changing the magnitude of the applied field generated by the electromagnet to ensure the uniformity of the applied field; this step was also necessary to eliminate the effect of the changing magnetic fields that otherwise would dominate the measured Hall signal. Similarly, the averaging procedure of combining results from different field sweeps was necessary to eliminate any noises and disturbances arising during the measurement process. The apparent drift between the decreasing and the increasing field sweeps across all Hall structures, of different cobalt thicknesses in figure (4.2.4), can be attributed to long stall times and averaging procedures of the experimental setup that might have generated joule heating. To clarify and properly address the underlying developments of the hysteresis measurement, the drifted branches of the field sweeps were ignored and the data of the hysteresis measurement was re-plotted; the re-plotted data from the hysteresis measurement is illustrated in figure(4.2.5a).

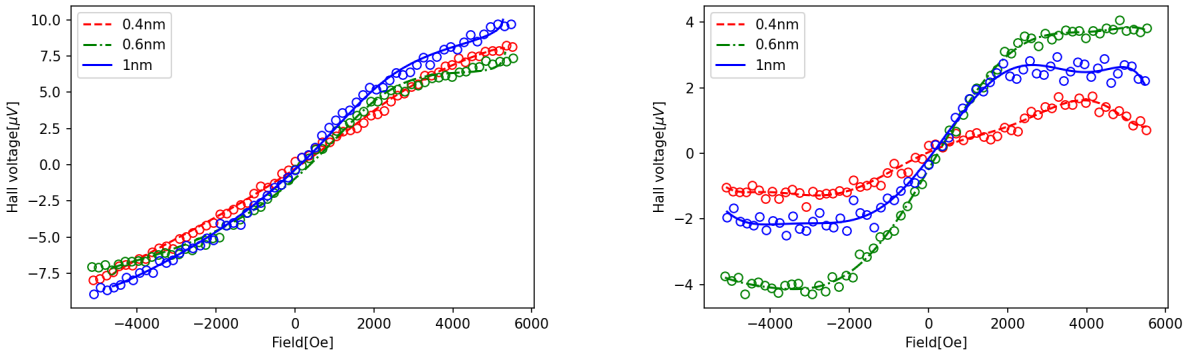

Figure 4.2.5: Processed Hall signals from Hall structures with cobalt thin films. **a)** Average Hall signals obtained from the experiment excluding the drift as seen in figure(4.2.4). **b)** Pure anomalous Hall component extracted after eliminating the ordinary Hall component of the acquired signal.

The slope of the trend in the figure(4.2.5a) generated during the field sweep is the upshot of the ordinary Hall effect(OHE), OHE arises when an electric conductor is placed inside a magnetic field. Similar to OHE, when a ferromagnetic conductor (Co in this case) is placed inside a magnetic field, the observed effect is called the Anomalous Hall Effect (AHE). AHE includes an additional component alongside the ordinary Hall component, resulting from the inherent magnetization of ferromagnetic materials. Since we are interested in studying the magnetization and anisotropy of the cobalt films of the Hall structure, we can eliminate the ordinary Hall component of the acquired signal to turn our focus on the pure anomalous Hall component. The result of subtracting the ordinary Hall component from the overall acquired signal is illustrated in figure (4.2.5b).

The pure anomalous Hall components in figure(4.2.5b) appear different across different cobalt thicknesses. The AHE component looks similar in shape for 0.6nm and 1.0nm thick cobalt films; however, the AHE component appears non-existent in the case of 0.4nm Co film. The AHE component is more prominent in 0.6nm thick cobalt film than in the case of 1.0nm thick cobalt film. We can note that the Hall voltage of the pure AHE signals is centered around the field value of 0 Oe, signifying that the anisotropy of the films is in-plane rather than out-of-plane in nature. Another important feature of the figure(4.2.5b) is the flattening of the hysteresis curve, insinuating

the saturation point. The 1.0nm cobalt film appears to saturate at approximately a field amplitude of 1800 Oe whereas the 0.6nm cobalt film seems to saturate at a field amplitude of approximately 2000 Oe.

Since the anisotropy of our fabricated ultra-thin Co films was in-plane rather than out-of-plane, we decided to experiment with a candidate film that promises a higher probability of PMA. One such material that is extensively used in Spintronics is an alloy of cobalt, Iron, and Boron; thin films made out of this alloy appear to have a better chance of out-of-plane anisotropy.

4.2.3 Hall measurements on CoFeB films

CoFeB is a type of amorphous metallic alloy made up of Cobalt, Iron, and Boron. In our study, the atomic composition of the constituents of the alloy was 20% Cobalt, 60% Iron, and 20% Boron, i.e., $Co_{20}Fe_{60}B_{20}$. CoFeB has become a material of significant interest in the field of spintronics because of its well-suited properties for spintronics applications. CoFeB films have been found to have high spin polarization, high Curie temperature, moderate to high saturation magnetization, low damping parameters, and strong magnetic anisotropy. CoFeB films are particularly popular while investigating a magnetic system with an out-of-plane anisotropy. The thickness criteria when out-of-plane anisotropy may be realized in CoFeB films is as high as 1.5nm, sometimes even higher. [33] Apart from the thickness criteria, another important method to help induce out-of-plane anisotropy in CoFeB system is annealing. In order to improve the quality of the film and the out-of-plane magnetic anisotropy of the film, a very thin layer of MgO (2nm-4nm) is stacked together with the CoFeB layer before annealing them to high temperatures ($300^\circ - 400^\circ\ C$). Annealing MgO/CoFeB films at $(300-400)^\circ C$ transfers the amorphous state of CoFeB into a crystalline state; moreover, the process also allows the diffusion of Boron into the adjacent MgO layer which further enhances the out-of-plane magnetic anisotropy of the film. [34] Here we will discuss the result obtained from Hall structures with CoFeB layer fabricated and prepared under different conditions.

Film fabrication parameter

The Hall structures made to study the CoFeB films had different thicknesses, the result of different thicknesses of the constituent layers. Our objective, in this particular

section, is to study the different kinds of Hall signal we get at different thicknesses and under different fabricating conditions. The thickness criteria of CoFeB layer was varied between 1nm-3nm during the process. Similar to the cobalt films, the fabrication process here utilizes the photolithography and sputter deposition technique to fabricate the Hall structure of interest. Table (4.2.2) summarizes some of the parameters used in the fabrication process of the films.

Table 4.2.2: Parameters used to fabricate the Hall structure comprising CoFeB films.

Sputter parameters	Layer attribute		
	Mgo	CoFeB	W
Base chamber pressure (Vacuum)	$6.5 \times 10^{-5} mbar$	$6.0 \times 10^{-5} mbar$	$6.0 \times 10^{-5} mbar$
Thickness	$3.0nm - 4.0nm$	$1.0nm - 3.0nm$	$6.0nm - 10.0nm$
Rate of deposition	$0.0424 \AA/s$	$0.357 \AA/s$	$0.267 \AA/s$
Argon flow rate	$15.0sccm$	$15.0sccm$	$10.0sccm$

The CoFeB Hall structures were made by stacking MgO film, CoFeB film, and W film respectively on top of the surface of Silicon substrates (SiO_2 on top). Silicon wafer is a better thermal conductor than glass; hence, it is more appropriate choice when annealing is required.

Result and Analysis

In order to test the kind of signal that would be obtained from CoFeB thin films, an initial test sample 4MgO/3CoFeB/10W was fabricated. The Hall sample was fabricated by stacking 4nm of MgO, followed by 3nm of CoFeB, followed by 10nm of W on top of a silicon substrate that had SiO_2 on top. The preparation of this test sample did not involve any annealing step. The result of sweeping an out-of-plane field through the surface of the Hall sample is summarized in figure (4.2.6).

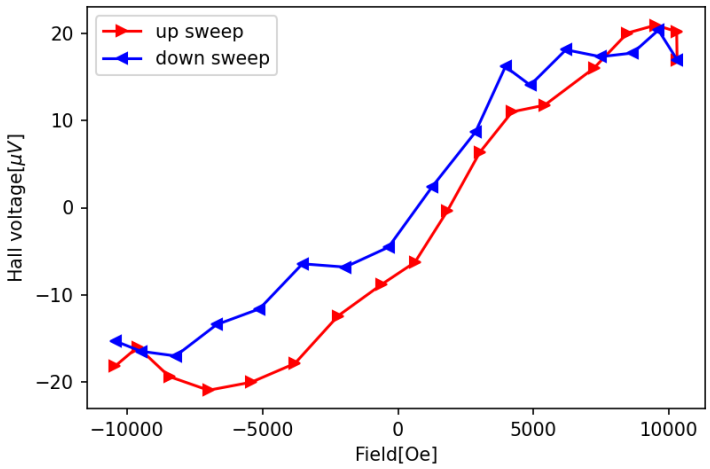

Figure 4.2.6: Hall signal obtained after sweeping an out-of-plane uniform field through a 4MgO/3CoFeB/10W test sample.

The hysteresis loop obtained in figure (4.2.6) is the final outcome after the averaging steps. This test sample had a thicker ferromagnetic (CoFeB) and heavy metal (W) layer; the anisotropy of CoFeB layer at this thickness criteria can be expected to be more in-plane than out-of-plane. The obtained trend here appears different than the results obtained from cobalt films. Despite using a higher field during the sweep, the magnetic signal does not give a clear impression of saturation points, and the ordinary and anomalous Hall components are very difficult to separate. The magnetic signal in figure (4.2.6) appears noisy, distorted and irregular. The test sample responds well to the changes in the externally applied magnetic field; however, the quality of the signal may have been poor due to the quality of the fabricated film.

The result from the initial test sample 4MgO/3CoFeB/10W elucidated the significance of the quality of the film. The quality of the film not only influences the anisotropy of the fabricated film but it also affects the quality of the Hall signal obtained from the Hall setup. Consequently, some changes were made to the fabrication process and the preparation of the sample to promote a better quality of the film. What little sonication was used during the fabrication process was completely eliminated and ample time was allocated to clean the substrate more thoroughly. In addition, the stack of films, making the Hall structure, was annealed to improve the crystal structure of the overall film and promote out-of-plane anisotropy; the sample

was heated to 350° C for an hour inside a high vacuum chamber (pressure reaching as low as 9.0×10^{-6} Pa). Three distinct Hall structures with different CoFeB thicknesses were fabricated next as neatly as possible; the thicknesses of the MgO under-layer and W capping layer were kept uniform among the batch of the samples. The results from the annealed samples are summarized in figure (4.2.7).

Figure (4.2.7) summarizes the result obtained for fabricated Hall structures with 3 distinct thicknesses of CoFeB films; the figure includes plots as acquired directly from the measurement and the processed plots focusing on the anomalous Hall component of the experiment. The phenomenon of interest within the plots in figure (4.2.7) are the sudden changes in the overall sloping trending of the Hall signal. As mentioned earlier, the slope or tilt of the curve in response to the field is caused by the ordinary Hall effect whereas the sudden changes from the overall tilting behavior are caused by the changes in the magnetization of the ferromagnetic layer. The Hall responses for different CoFeB thicknesses in figure (4.2.7) appear very distinctive. The Hall response in the case of 3nm CoFeB in figure (4.2.7a) appears almost linear in nature, with some fluctuations; the linear response when flattened in figure (4.2.7b) reveals very little sign of changes in magnetization. The quality of the signal obtained from 3nm CoFeB suggests that the annealing procedure had very little impact on the quality of the film.

The plots for 2nm CoFeB have a very different kind of result compared to the outcome of 3nm CoFeB. The signal in figure (4.2.7c) is the type of response we expect to get while subjecting a Hall structure with a ferromagnetic layer to a sweeping magnetic field. The ordinary Hall component is clearly demonstrated in the overall tilt of the "S" curve in the figure (4.2.7c); similarly, the big smooth changes in Hall signal observed in response to the field is a direct consequence of the changes in inherent magnetization, embodied by the anomalous Hall component of the signal. The result of subtracting the ordinary Hall component of the acquired dataset for 2nm CoFeB is illustrated in figure (4.2.7d); the perfect "S" curve helps us to characterize the ferromagnetic layer of the Hall structure. The curve in figure (4.2.7d) is centered around a field value of 0 Oe and shows a very small sign of remanence; these features of the curve help us to deduce that the anisotropy of the magnetic film for 2nm CoFeB is still in-plane in nature. The magnetic layer of the Hall structure in figure (4.2.7d)

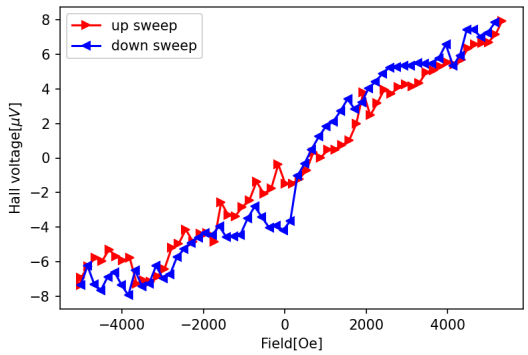

(a) 3MgO/3CoFeB/6W (AHE + OHE)

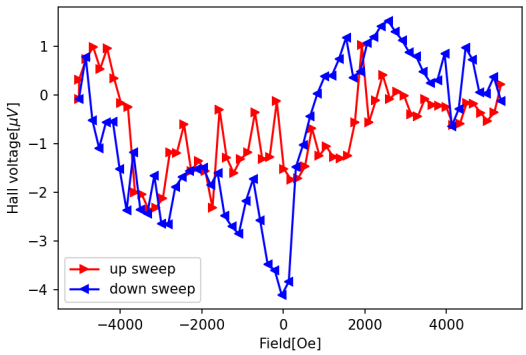

(b) 3MgO/3CoFeB/6W (AHE)

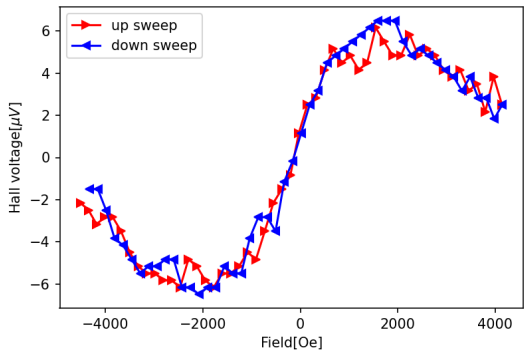

(c) 3MgO/2CoFeB/6W (AHE + OHE)

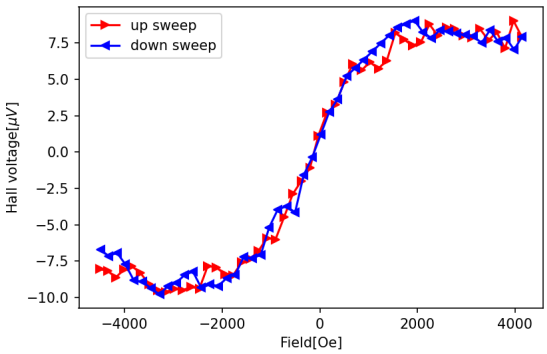

(d) 3MgO/2CoFeB/6W (AHE)

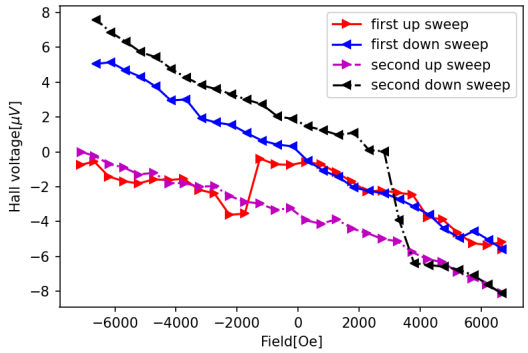

(e) 3MgO/1.2CoFeB/6W (AHE + OHE)

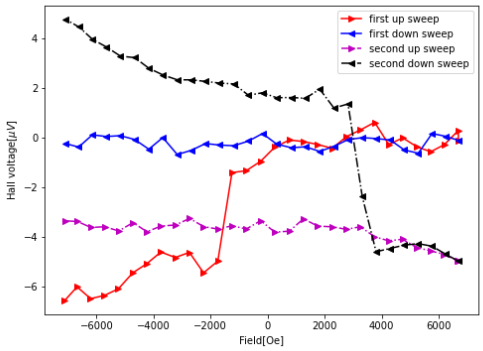

(f) 3MgO/1.2CoFeB/6W (AHE)

Figure 4.2.7: Processed Hall signals from Hall structures with CoFeB thin films. Plots **a)**, **c)** and **e)** show the result as acquired directly from the measurement for Hall structures with 3nm, 2nm, and 1.2nm CoFeB respectively (includes both ordinary and anomalous Hall component). Plots **b)**, **d)** and **f)** show the pure anomalous Hall component obtained after subtracting the ordinary Hall component from the corresponding experimentally acquired dataset for 3nm, 2nm, and 1.2nm CoFeB respectively.

can be seen to saturate at an amplitude of approximately 2000 Oe during the out-of-plane field hysteresis. The annealing process in the case of 2nm CoFeB seems to have improved the quality of the film and hence the quality of the Hall signal during the experiment.

The plots for 1.2nm CoFeB differ from the plots of 3nm CoFeB and 2nm CoFeB. Figure (4.2.7e) portrays the result of two different field sweeps for 1.2 nm CoFeB; the first and second field sweeps are both included in the plot to show different developments in response to the external field. The result of excluding the ordinary Hall components from the experimental data for 1.2 nm CoFeB is depicted in figure (4.2.7f). The sudden change in magnetization during the first field sweep in figure (4.2.7f) can be observed when the polarity of the field is changed from positive to negative; on the other hand, a similar change in magnetization is observed during the second field sweep when the polarity of the field is changed from negative to positive. It can also be noticed in figure (4.2.7f) that the similar changes in the Hall voltage during the reverse sweep in both field sweeps are absent; the changes in magnetization, however prominent, were sporadic in nature. The sporadically occurring changes in the Hall voltage of both field sweeps again raise concern about the quality of the film and the measurement technique.

Throughout the signal obtained from different thicknesses of CoFeB, the range of the Hall signal obtained during the field sweep was consistent. A DC of 100mA was used for all hysteresis measurements discussed in this chapter; despite the high amplitude of the applied current, it must be noted that only a small fraction of the applied current passed through the sample due to the presence of the terminating resistor. Furthermore, the slope of the curves obtained in the case of 2.0nm and 1.2 nm CoFeB Hall structures in response to the magnetic field were very consistent. These consistencies help us to assert that the changes observed during the field sweeps were entirely magnetic responses. Since the response from 3.0nm CoFeB Hall structures appeared odd, further study of the Hall signal for Hall structures with thicker ferromagnetic layers may be required.

4.2.4 Hall signal comparison across different compositions

Thus far we have only discussed the Hall effects on ferromagnetic films less than or equal to 3nm; in this section, we will do a comparative study of the Hall effects on thicker ($\geq 5nm$) ferromagnetic films. The effect of subjecting a conductive non-magnetic film to the magnetic field is also included in the comparison. The objective of this section is to compare the Hall signals across the Hall structures with a purely ferromagnetic layer, a purely non-magnetic layer, and a bi-layer comprising ferromagnetic and heavy metal layers.

Film fabrication parameter

The same photolithography technique, the Hall bar pattern, and the Hall effect setup as mentioned in section (4.2.1) are used here for the comparative study. The purely ferromagnetic Hall structure is made up of 11nm thick CoFeB, the purely non-magnetic Hall structure comprises 6nm thick W, and the bi-layer Hall structure is a stack of 5nm CoFeB and 6nm W. The fabrication process did not involve any annealing step. The fabrication parameters for the films involved are summarized in table (4.2.3).

Table 4.2.3: Fabrication parameters used in the fabrication of ferromagnetic and non-magnetic Hall structures.

Sputter parameters	Layer attribute		
	Mgo	CoFeB	W
Base chamber pressure (Vacuum)	$7.0 \times 10^{-5} mbar$	$5.5 \times 10^{-5} mbar$	$5.0 \times 10^{-5} mbar$
Thickness	$3.0nm$	$5.0nm$ & $11.0nm$	$6.0nm$
Rate of deposition	$0.0427 \mathring{A}/s$	$0.357 \mathring{A}/s$	$0.267 \mathring{A}/s$
Argon flow rate	$15.0sccm$	$15.0sccm$	$10.0sccm$

All the Hall structures are fabricated on a Silicon substrate with SiO_2 on top. A 3nm MgO is used as an underlayer for all the fabricated Hall structures and the motive of its use is to maintain consistency; moreover, it also has a good adhesive quality to

most substrates.

Result and Analysis

The fabricated Hall structures were affixed to our custom circuit board and then configured accordingly for the Hall effect measurement setup. A constant DC of 100mA was applied across the current arms of the Hall structures and corresponding Hall voltages were measured through the voltage arms. The signals from the corresponding samples in response to the uniform out-of-plane field are summarized in figure (4.2.8).

Figure (4.2.8) illustrates the Hall effects experienced by our fabricated structures under the influence of the applied magnetic field. Figure (4.2.8a) includes the data acquired directly from the measurement setup for the 6nm W Hall structure; the plot reveals the expected linear relationship between the Hall voltage and the applied magnetic field. The linear response is a clear indication of the ordinary Hall effect; the absence of kinks and curves in figure (4.2.8a) and figure (4.2.8b) suggest that those features are the characteristics of a system with ferromagnetic thin films.

The acquired response of the bi-layer Hall structure of 5nm CoFeB and 6nm W is illustrated in figure (4.2.8c); the corresponding anomalous component extracted after subtracting the ordinary Hall component from the acquired response is portrayed by figure (4.2.8d). The kinks in the plots are an indication of the change in inherent magnetization of the ferromagnetic layer. The shape of the Hall response appears different from the Hall responses of ferromagnetic devices below 3nm thickness. The expected anisotropy of the 5nm CoFeB film, present in the bi-layer structure, is in-plane; despite the similarity in anisotropy, the shape of the Hall response appears “W” shaped rather than the usual “S” curve of the magnetic hysteresis. Furthermore, it can be seen in the plots that the kinks occur at an approximate field strength of 1000 Oe, and a huge change in the Hall voltage can be observed succeeding the critical points.

The result acquired from the Hall measurements on a purely ferromagnetic 11nm CoFeB film is shown in figure (4.2.8e); the pure anomalous component of the dataset

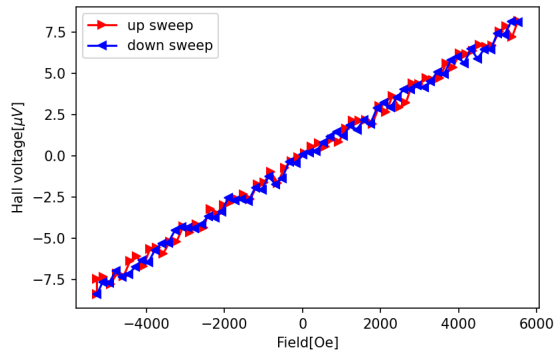

(a) 3MgO/6W (AHE + OHE)

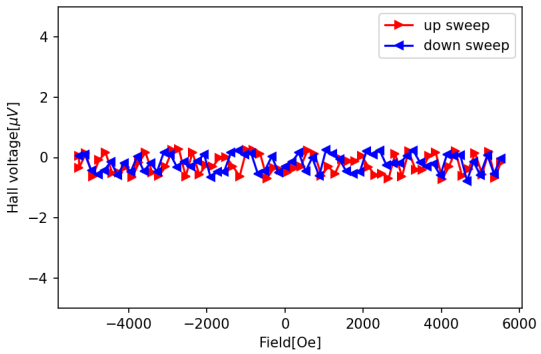

(b) 3MgO/6W (AHE)

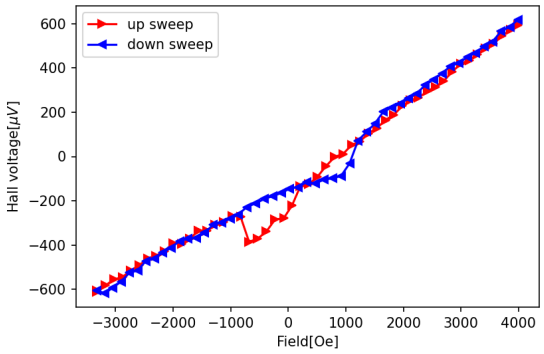

(c) 3MgO/5CoFeB/6W (AHE + OHE)

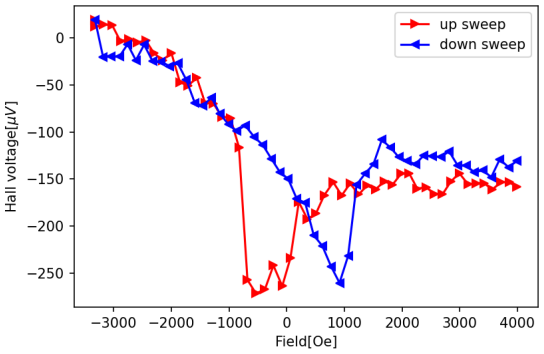

(d) 3MgO/5CoFeB/6W (AHE)

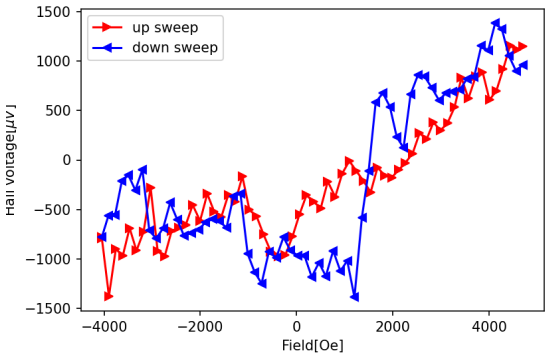

(e) 3MgO/11CoFeB (AHE + OHE)

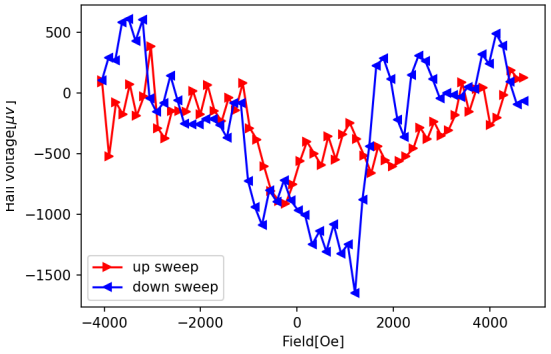

(f) 3MgO/11CoFeB (AHE)

Figure 4.2.8: Processed Hall signals from Hall structures of different thicknesses and composition. Plots **a)**, **c)** and **e)** show the result as acquired directly from the measurement for 3MgO/6W, 3MgO/5CoFeB/6W, 3MgO/11CoFeB respectively (includes both ordinary and anomalous Hall components). Plots **b)**, **d)** and **f)** show the pure anomalous Hall component obtained after subtracting the ordinary Hall component from the corresponding experimentally acquired dataset for 3MgO/6W, 3MgO/5CoFeB/6W, 3MgO/11CoFeB respectively.

has been plotted in figure (4.2.8f). The result from 11nm CoFeB appears analogous to the response obtained from the bi-layer Hall structure comprising 5nm CoFeB. Even though the response from the 11nm CoFeB appears noisy and erratic, the variations in the Hall voltage due to the changes in magnetization are comparatively bigger. A thicker film with lower resistivity allows more electrons to flow through the current channel, thus deflecting more electrons across the voltage channels of the Hall structure; the effect can be seen to be correctly encapsulated in the experiment dataset. The result from 11nm CoFeB further corroborates the finding that the shape of the Hall response on thicker ($\geq 5nm$) ferromagnetic devices is different than the Hall response of ultrathin ($\leq 3nm$) ferromagnetic devices.

4.2.5 Developments and challenges for SOT measurements

Deterministic magnetization switching using spin-orbit torque usually requires considerable current density. Even though the critical current density for a magnetic system utilizing SOT depends on factors such as the SOT source material's spin hall angle and the magnetic layer's properties, the optimal current density required may still be in the order of 10^{12} A/m^2. The integrity of the fabricated micro-structure may not hold at such current density when current is applied for a longer period of time. One of the solutions to address this issue is to make use of short current pulses; current pulses in the range of (5-10)ns FWHM can be expected to generate the required SOT effect while preserving the integrity of the fabricated structure.

SOT experiments can make use of both in-plane and out-of-plane magnetic anisotropies. SOT experiments with in-plane anisotropy of the magnetic layer usually do not require an additional external field to achieve deterministic magnetization reversal; experiments requiring no use of the external field for magnetization switching are called field-free magnetization switching experiments. Such experiments rely on optical means to probe and characterize the inherent magnetization; lasers used in such experiments must be stable, and the setup should minimize mechanical vibrations and noises. On the other hand, SOT experiments with out-of-plane magnetic anisotropy often require an external field in the direction of applied current to achieve deterministic magnetization reversal; such experiments are usually referred to as field-assisted magnetization switching experiments. Both optical means and the Hall-based measurement techniques can be used to observe changes in the inherent magnetization of

such field-assisted switching experiments.

In our project, we initially tried to conduct a field-free magnetization switching SOT experiment but we realized our measurement setup was not stable and sensitive enough to probe the changes in the magnetization of our fabricated microstructure. We then proceeded toward the Hall-based measurement technique to study the effect in magnetic systems with out-of-plane anisotropy. Since the field-assisted SOT experiment heavily relies on the anisotropy of the magnetic system being out-of-plane, we were not able to acquire a solid SOT-dependent signal while using our fabricated structures. The setbacks from our experimental endeavor have made us realize that the study of film quality is very important before making a qualitative film with out-of-plane anisotropy. Furthermore, we found out that a simple setup such as ours could be very noisy and unstable; hence, some changes regarding current sources and amplifiers may be essential to acquire solid signals.

Chapter 5

Summary and Conclusion

Our study was motivated by the idea of spin-orbit torque. The project was mainly divided into two different segments: numerical simulation and experimental approach. The numerical simulation focused on modeling an experimental idea using a popular object-oriented framework tool OOMMF. The purpose of the simulation was to model a magnetic system including SOT and develop an idea about the critical parameters of the system. The experimental segment of the project focused on the fabrication and testing of the modeled system.

The first portion of the modeling concentrated on the study of thermal effects on a nanometer-sized CoFeB Hall structure. The size of the model used for this particular segment was nanometers rather than micrometers to save on time and computational cost. The evolution and progress of the simulation while encompassing thermal effects is much slower than its ideal counterpart where thermal effects are often ignored. The result of including thermal effects in simulations revealed a considerable drop in the critical parameters of magnetization switching. The magnitude of the critical field value needed for field-induced magnetization reversal dropped by 500 Oe from an 1100 Oe critical field value when thermal effects were included in the simulation. Similarly, the magnitude of the critical current density needed for current-induced magnetization reversal dropped to a $4.16 \times 10^{11} A/m^2$(current amplitude of $50\mu A$) from $6.66 \times 10^{11} A/m^2$(current amplitude of $80\mu A$) when thermal effects were included. Such a significant decrease in the magnitude of critical parameters in magnetization switching clearly demonstrates that thermal effects aid magnetization reversal in magnetic systems. For a sensitive experimental approach, the inclusion of thermal effects, if necessary, must be included in models as it has been found to

influence the outcome of the models greatly.

The second portion of the simulation concentrated on modeling a micrometer-sized CoFeB Hall structure, that would closely resemble the actual experimental sample. As the size, complexity, and discretization of the model used in modeling directly influence the pace and time consumption of simulations, few compromises were made while modeling the micrometer-sized Hall structure. The individual cell used to discretize the simulation world was changed from a cubic $2nm \times 2nm \times 2nm$ cell to a stretched cuboidal $500nm \times 500nm \times 1nm$ cell and the thermal effects were excluded from the model to save on time and computational cost. Since the dimension of the cell size in planer x and y directions is bigger than the accepted exchange length of the magnetic system, the micrometer-sized simulation models are more approximate than accurate in nature. The simulation gave an estimate of an approximately 100mA current amplitude (current density of $2.5 \times 10^{12} A/m^2$) for a complete magnetization reversal with an assisted in-plane field of 1000 Oe along the direction of current flow. It must be noted here that thermal effects were not considered which would otherwise significantly drop the critical parameters of the magnetization switching. No remanence was observed during current-induced magnetization hysteresis; however, a smooth response of the magnetization was observed in response to the amount of current applied in the model. When short current pulses were used in modeling, the changes in magnetization were found to be short-lived and they quickly subsided as the amplitude of the pulse gradually faded. It was further speculated that such fast changes in magnetization during the application of fast current pulses may be difficult to observe with simple Hall measurement techniques.

The primary task of the experimental approach was to characterize tungsten films using their sheet resistance. Sheet resistance measurement was carried out by employing Van der Pauw's 4-point method. Cloverleaf patterns and square patterns with contact points at corners were used during measurements; the patterns were synthesized by making use of photolithography and sputter deposition techniques. The expected behavior of an increase in resistivity with the reduction in the thicknesses of the film was obtained from the experiment. The experiment revealed a usual bulk resistivity value of $(50 - 65)\mu\Omega cm$ for tungsten films above 50nm thickness; whereas, the resistivity of tungsten films at thicknesses below 10nm was found to be as high as $(190 - 230)\mu\Omega cm$. The usual resistivity value at thicker films indicated the presence

of $\alpha - W$ in fabricated films; whereas, the very high resistivity at thicknesses below 10nm insinuated the presence of $\beta - W$ in the synthesized films. The spin Hall angle for $\beta - W$ films has been reported to be -0.33, making it a very good source material of SOT.

The deterministic field-assisted magnetization switching through SOT in our project requires a ferromagnetic layer with out-of-plane anisotropy; therefore, the second task of the experimental approach was focused on the study of anisotropies of the fabricated film structures. The magnetic measurement technique employed for studying the magnetization of our fabricated devices was the Hall-based technique. A 4-contact symmetric Hall structure was fabricated with the material of interest to characterize the magnetic films. Good quality cobalt films under 1nm thickness have been known to exhibit signs of perpendicular magnetic anisotropy (PMA); thus, initially, we decided to fabricate Hall structures with cobalt films. Film stacks of MgO/Co/W Hall structures were fabricated and studied using a Hall-based measurement technique to characterize cobalt films of variable thicknesses. The experiment only revealed an in-plane anisotropy in Co films under 1nm, the signal quality for 0.6nm Co film was found to be better than 1nm Co film; however, the Hall signal indicated the presence of in-plane anisotropy despite the extreme thickness criteria of the film.

The result from Co films motivated us to find an alternative material that showed higher chances of PMA. Upon consideration, we decided to switch to $Co_{20}Fe_{60}B_{20}$ films from Co films while fabricating the Hall structure; CoFeB is a very popular ferromagnetic material that is extensively used in Spintronics and SOT-related experiments. The same Hall-based experiment was repeated for CoFeB; however, the initial test sample did not produce any better results than the Co films. The CoFeB test sample accentuated the importance of film quality and encouraged a few modifications in our fabrication process. The next batch of Hall structures was carefully made and annealed to $350°C$ for an hour to improve the quality of the film by making it more crystalline. The result from annealed samples was significantly better than the initial non-annealed sample. The 2nm CoFeB annealed Hall structure produced a promising Hall signal with clear switching points during the experiment.

The result from the 2nm CoFeB Hall structure was promising but its hysteresis measurement did not show any sign of remanence. We speculated that the anisotropy of

the 2nm CoFeB film must be out-of-plane, even if not perfectly PMA, and continued to SOT measurement. We quickly realized that our simple Hall-based measurement setup was not stable and sensitive enough to record–if any–SOT-induced effects. The setbacks from our experimental endeavor also made us realize the importance of the study of film quality. The study of film quality is a long and extensive process as it involves tuning and adjusting several parameters of the fabricating procedure. In our project, we do not further proceed with the study of film quality but we acknowledge its significance for an experiment such as ours.

Our SOT-motivated project slowly transitioned to a comparative study of Hall signals at different thicknesses of ferromagnetic devices. Despite the setback from SOT measurements, we decided to proceed further and include a comparative study of Hall signals at higher thicknesses of ferromagnetic devices. The end section of our project compares the Hall effect in purely non-magnetic, purely magnetic, and a mixture of magnetic and non-magnetic Hall structures. A purely non-magnetic Hall structure, 3MgO/6W, revealed an expected linear response of the Hall voltage to the applied field. The Hall structure with mixed layers, 3MgO/5CoFeB/6W, revealed a rather surprising "W" shaped hysteresis curve than the usual "S" hysteresis curve noticed earlier with ferromagnetic samples below 5nm. The purely magnetic Hall structure, 3MgO/11CoFeB, revealed a hysteresis curve analogous to the "W" shaped hysteresis curve; however, the strength of the signal or Hall voltage in the case of the purely magnetic layer appears to be higher than the case of the mixed layer.

Our project encompasses the numerical and experimental approaches to SOT-inspired ideas using a simple Hall structure. We hope our research and endeavor serve as a reference and building block for future experimental endeavors similar to ours.

Bibliography

[1] *Spin Current and Spin Dynamics*, chapter 6, pages 105–149. John Wiley & Sons, Ltd, 2020.

[2] Sunil Nair, S. Wirth, S. Friedemann, F. Steglich, Q. Si, and A. J. Schofield. Hall effect in heavy fermion metals. *Advances in physics*, 61(5):583–664, 2012.

[3] Naoto Nagaosa, Jairo Sinova, Shigeki Onoda, A. H. MacDonald, and N. P. Ong. Anomalous hall effect. *Reviews of modern physics*, 82(2):1539–1592, 2009.

[4] Hongming Weng, Xi Dai, and Zhong Fang. From anomalous hall effect to the quantum anomalous hall effect. *arXiv preprint arXiv:1509.05507*, 2015.

[5] Yu-Ming Hung. *Spin currents and spin orbit torques in ferromagnets and antiferromagnets*. PhD thesis, New York University, 2017.

[6] Niklas Roschewsky. *Spin-Orbit Torques in Ferrimagnets and Topological Insulators*. PhD thesis, UC Berkeley, 2019.

[7] Halise Celik. *Spin-orbit torque measurements in heavy metal/ferromagnet heterostructures using the magneto-optic Kerr effect*. PhD thesis, University of Delaware, 2018.

[8] D.C. Ralph and M.D. Stiles. Spin transfer torques. *Journal of Magnetism and Magnetic Materials*, 320(7):1190–1216, 2008.

[9] Lijun Zhu, Daniel C. Ralph, and Robert A. Buhrman. Maximizing spin-orbit torque generated by the spin hall effect of pt. *Applied Physics Reviews*, 8(3), 2021.

[10] Qiming Shao, Peng Li, Luqiao Liu, Hyunsoo Yang, Shunsuke Fukami, Armin Razavi, Hao Wu, Kang Wang, Frank Freimuth, Yuriy Mokrousov, et al. Roadmap of spin–orbit torques. *IEEE Transactions on Magnetics*, 57(7):1–39, 2021.

[11] AR Mellnik, JS Lee, A Richardella, JL Grab, PJ Mintun, Mark H Fischer, Abolhassan Vaezi, Aurelien Manchon, E-A Kim, Nitin Samarth, et al. Spin-transfer torque generated by a topological insulator. *Nature*, 511(7510):449–451, 2014.

[12] Jiaxing Liu. *Deposition and characterization of magnetron sputtered beta-tungsten thin films*. PhD thesis, Columbia University, 2016.

[13] WF Brown Jr. Micromagnetics 18 john wiley & sons. *New York*, 1963.

[14] Isaak D Mayergoyz, Giorgio Bertotti, and Claudio Serpico. *Nonlinear magnetization dynamics in nanosystems*. Elsevier, 2009.

[15] Michael J Donahue and MJ Donahue. Oommf user's guide, version 1.0. 1999.

[16] E Martínez, L López-Díaz, L Torres, and CJ García-Cervera. Minimizing cell size dependence in micromagnetics simulations with thermal noise. *Journal of Physics D: Applied Physics*, 40(4):942, 2007.

[17] Dmytro Chumakov. High frequency behaviour of magnetic thin film elements for microelectronics. 2006.

[18] Sachin Pathak, Chanyoung Youm, and Jongill Hong. Impact of spin-orbit torque on spin-transfer torque switching in magnetic tunnel junctions. *Scientific reports*, 10(1):2799, 2020.

[19] Pietro Gambardella and Ioan Mihai Miron. Current-induced spin–orbit torques. *Philosophical Transactions of the Royal Society A: Mathematical, Physical and Engineering Sciences*, 369(1948):3175–3197, 2011.

[20] Ioan Mihai Miron, Kevin Garello, Gilles Gaudin, Pierre-Jean Zermatten, Marius V Costache, Stéphane Auffret, Sébastien Bandiera, Bernard Rodmacq, Alain Schuhl, and Pietro Gambardella. Perpendicular switching of a single ferromagnetic layer induced by in-plane current injection. *Nature*, 476(7359):189–193, 2011.

[21] Gabriel D Chaves-O'Flynn, Daniele Pinna, Georg Wolf, and Andrew D Kent. Micromagnetic study of spin transfer switching with a spin polarization tilted out of the free layer plane. *Journal of applied physics*, 117(17):17–, 2015.

[22] Qiming Shao, Peng Li, Luqiao Liu, Hyunsoo Yang, Shunsuke Fukami, Armin Razavi, Hao Wu, Kang Wang, Frank Freimuth, Yuriy Mokrousov, Mark D. Stiles, Satoru Emori, Axel Hoffmann, Johan Akerman, Kaushik Roy, Jian-Ping Wang, See-Hun Yang, Kevin Garello, and Wei Zhang. Roadmap of spin-orbit torques. *IEEE transactions on magnetics*, 57(7):1–39, 2021.

[23] Can Onur Avci, Kevin Garello, Ioan Mihai Miron, Gilles Gaudin, Stéphane Auffret, Olivier Boulle, and Pietro Gambardella. Magnetization switching of an mgo/co/pt layer by in-plane current injection. *Applied physics letters*, 100(21):212404–212404–3, 2012.

[24] Hans H. Gatzen, Volker Saile, and Jürg Leuthold. *Deposition Technologies*, pages 65–203. Springer Berlin Heidelberg, Berlin, Heidelberg, 2015.

[25] Krishna Seshan. *Handbook of thin film deposition techniques principles, methods, equipment and applications*. Materials science and process technology series. Electronic materials and process technology. CRC Press, an imprint of Taylor and Francis, Boca Raton, FL, 2nd ed. edition, 2002.

[26] Coralie Charpentier. *Investigation of deposition conditions and annealing treatments on sputtered ZnO: Al thin films: Material properties and application to microcristalline silicon solar cells*. PhD thesis, Ecole Polytechnique X, 2012.

[27] Dmitrii V. Sidelev, Galina A. Bleykher, Vladislav A. Grudinin, Valery P. Krivobokov, Massimiliano Bestetti, Maxim S. Syrtanov, and Evgenii V. Erofeev. Hot target magnetron sputtering for ferromagnetic films deposition. *Surface & coatings technology*, 334:61–70, 2018.

[28] O Philips'Gloeilampenfabrieken. A method of measuring specific resistivity and hall effect of discs of arbitrary shape. *Philips Res. Rep*, 13(1):1–9, 1958.

[29] DW KOON. Effect of contact size and placement, and of resistive inhomogeneities on vanderpauw measurements. *Review of scientific instruments*, 60(2):271–274, 1989.

[30] Philippa H. McGuinness. *Probing unconventional transport regimes in delafossite metals*. Springer theses. Springer, Cham, Switzerland, 2022.

[31] Yong Jin Kim, Sung-Gyu Kang, Yeonju Oh, Gyu Won Kim, In Ho Cha, Heung Nam Han, and Young Keun Kim. Microstructural evolution and electrical resistivity of nanocrystalline w thin films grown by sputtering. *Materials characterization*, 145:473–478, 2018.

[32] Victorino Franco and Brad Dodrill. *Magnetic Measurement Techniques for Materials Characterization*. Springer International Publishing, Cham, 2021.

[33] L Saravanan, Nanhe Kumar Gupta, Lalit Pandey, I Phebe Kokila, HA Therese, and Sujeet Chaudhary. Observation of uniaxial magnetic anisotropy and out-of-plane coercivity in w/co20fe60b20/w structures with high thermal stability. *Journal of Alloys and Compounds*, 895:162600, 2022.

[34] Zhangliang Xu and Lei Qin. Effects of sputtering parameters and annealing temperatures on magnetic properties of cofeb films. *Journal of Magnetism and Magnetic Materials*, 538:168302, 2021.

Appendix A

Photolithography Recipe and Instructions

1st step: Cleaning and preparing the substrate

1. Submerge the substrate into an acetone bath. Sonication can be used but not for long. A quick 10s sonication does the job for me after soaking the substrate for at least 1-2 min to remove any visible impurities.

2. Wash the substrate with IPA (Isopropanol) immediately after taking the substrate out from acetone bath.

3. Wash the substrate again with DI water after taking the substrate out from IPA.

4. Blow dry the substrate and put it on the hot plate (temperature anywhere above $100°C$). This ensures all remnant solvents to evaporate from the substrate.

2nd step: Spin coating

5. Adjust the following setting on the spin coater:

   (a) Initial spread at 500rmp for 5s, i.e. 1st level: acceleration - 100rmp, time - 5s.

(b) Rapid acceleration of 1304 rpm reaching 5000 rmp and hold it for at least 40s, i.e. 2nd level: acceleration - 1304 rpm, time - 45s.

(c) Decelerate before coming to a halt, i.e. 3rd level: acceleration: - 1000rmp, time - 5s. This ensures the coated sample to smoothly come to rest instead of an abrupt stop.

6. Put the substrate onto the suction plate of the spin coater; center your substrate to the best of your ability! Enable vacuum and ensure that the spin coater says 'Ready!' to proceed further.

7. Dispense LOR 2A using a dropper and quickly press the start button. Spin coating with or without the top lid affect the coating so stick to one option: either leave the lid open all the time or close the lid all the time while spin coating!

8. Prebake the coated sample at $(160 - 210)°C$ for 5min. If using hotplate, ensure that the hot plate is at correct temperature by measuring it with a thermometer! The temperature I am using is $180°C$. Also it is advisable to cover the hot plate with aluminum foil to avoid the contamination of the surface with photoresist.

9. Take the sample out and let it cool down for a while (about 2-3min) and spin coat the sample using S1805. **A single resist layer of S1805 without the base LOR2A layer also works just as fine; therefore, it can be used when bi-layer resist is not needed.**

10. Softbake the sample with bi-layer resist for about 2min (on glass) at $115°C$.

3rd step: Exposing the sample

11. Follow the instruction on how to operate the aligner and expose the coated sample for 2s (if using glass) or 6.5s (if using Si substrate). When patterning big structures such as contact pad, exposure time as high as 12s can be used if the dimension criteria is not very strict. Higher exposure time results in over development but it results in much cleaner structures. Make sure that the sample is dry before putting it on the aligner.

4th step: Development

12. Develop the exposed sample by putting it inside MF-319 developer bath for 30s; it is recommended to agitate the solution during development process by gently shaking (while grabbing) the sample inside the solution using tweezers.
13. Immediately rinse the developed sample for at least 20s using DI water to stop over development process.
14. Blow dry the substrate using air gun to remove traces of solvents from the substrate surface.

5th step: Deposition of the material

15. Deposit the required thickness of material using for eg. Sputter system.

6th step: Lift-off

16. Either PG remover (recommended in data sheet of the photo-resist) or acetone can be used to dissolve the sacrificial photoresist layer during the lift-off process.
17. If using PG remover, you can use two different baths of PG remover for lift-off. You can also heat the remover to an approx. temperature of $60°C$ to increase the solubility of the photoresist.
18. If using acetone, enough acetone has to be used during the lift-off process since the solution quickly evaporates when left uncovered.
19. Agitating the substrate, spraying the solvent on the substrate and letting it soak for ample time during the lift-off process all helps to remove the residues from the substrate surface. Sonication during the lift-off process has been found to damage the fabricated structures so should be avoided.
20. After successful lift-off, the substrate has to be immediately rinsed by IPA followed by DI water bath to remove traces of remover from the substrate. The substrate should then be dried using the air gun to remove residual solvents from the surface.

Appendix B

Simulation Codes

B.1 Sample MIF file used in SOT simulation

```
# MIF 2.1
# Description: Hysteresis loop at room temperature including oersted
    field.

set pi [expr {4*atan(1.0)}]
set mu0 [expr {4*$pi*1e-7}]

# Parameter for the output directory. Essential while using boxsi
   and python script.
Parameter out_folder default
Parameter init_sim 1
Parameter in_omf thermal_CoFeB_4nm_B0_relaxed.omf
Parameter total_current 1; # the magnitude is later multiplied by
   conversion factor and assigned to new variable current
set current [expr {$total_current*1e-6}]; # current in uA.

# Dimensions of SOT metal (Tungsten)
set cond_width 30e-9
set cond_thick 5e-9
set cond_length 150e-9


set current_area [expr { $cond_width * $cond_thick }]; # cross
   section of Hall bar
set Jcurr [expr {$current/$current_area}];  # current density

```

```
23
24 # Seed and time steps parameters
25 Parameter seed 23446;
26 eval RandomSeed $seed
27 set time_steps 2e-14
28 set Temp 298
29
30 # Material Parameter (CoFeB)#
31 Parameter Ms 9.57e5;
32 # Saturation Magnetization (unit:A/m)
33 Parameter A 13e-12;
34 # Exchange Coefficient (Stiffness) (unit:J/m)
35 Parameter Polarization -0.33;
36 # Spin orbit torque efficiency for Tungsten
37 Parameter Lambda 1
38 Parameter alpha 0.01;
39 # Damping parameter
40
41
42 # Initial magnetization
43 set init_mag {{0.5 0.5 0.5}};
44 # Only used for initial relaxation simulation, later replaced by the
       magnetization state of preceding simulation.
45 set cellsize 1.0e-9
46
47
48 # Parameters for oersted field
49 set a [expr { $cond_width/2 }]
50 set b [expr { $cond_thick/2 }]
51 set yscale 1
52 set zscale 1
53 set yshift -50e-9
54 set zshift 0
55 set C1 [expr {$current/(8*$pi*$a*$b)}]
56
57
58 # Setting a formatting string to prepend it to output to prevent the
       output data from being over-written
59 set outname [format "%s/thermal_CoFeB_4nm_with_Oe_J%.0f" $out_folder
       $total_current]
60
61 # Defining different sections of the Hall bar.
```

```
Specify Oxs_BoxAtlas:MainBody_left [subst {
  xrange {0 50e-9}
  yrange {35e-9 65e-9}
  zrange {0 4e-9}
}]

Specify Oxs_BoxAtlas:MainBody_center [subst {
  xrange {50e-9 100e-9}
  yrange {35e-9 65e-9}
  zrange {0 4e-9}
}]

Specify Oxs_BoxAtlas:MainBody_right [subst {
  xrange {100e-9 150e-9}
  yrange {35e-9 65e-9}
  zrange {0 4e-9}
}]

Specify Oxs_BoxAtlas:Up_Volt_arm [subst {
  xrange {70e-9 80e-9}
  yrange {65e-9 100e-9}
  zrange {0 4e-9}
}]

Specify Oxs_BoxAtlas:Down_Volt_arm [subst {
  xrange {70e-9 80e-9}
  yrange {0 35e-9}
  zrange {0 4e-9}
}]

# Gathering mainbody sections
Specify Oxs_MultiAtlas:MainBody [subst {
  atlas MainBody_left
  atlas MainBody_center
  atlas MainBody_right
}]

# Putting all components together
Specify Oxs_MultiAtlas:atlas [subst {
  atlas MainBody
  atlas Up_Volt_arm
  atlas Down_Volt_arm
```

```
}]


# Mesh Specification
Specify Oxs_RectangularMesh:mesh [subst {
  cellsize { [expr {2*$cellsize}] [expr {2*$cellsize}] [expr {2
   *$cellsize}] }
  atlas :atlas
}]


# Anisotropy field (Ha) used to assign uniaxial anisotropy
Specify Oxs_UniaxialAnisotropy:PMA [subst {
  Ha  [expr {11000*1e-4/$mu0}]
  axis {0 0 1}
}]


Specify Oxs_UniformExchange [subst {
   A  $A
}]

# Oersted field from the underlying conductor
proc field_from_wire {xrel yrel zrel} {
  global a
  global b
  global yscale
  global zscale
  global yshift
  global zshift
  global C1
  set T1 [expr {
    0.5*log((pow(($b-($zrel+$zshift)*$zscale),2) + pow(($a-($yrel+
   $yshift)*$yscale),2))/(pow((-$b-($zrel+$zshift)*$zscale),2) + pow
   (($a-($yrel+$yshift)*$yscale),2))) + (($b-($zrel+$zshift)*$zscale
   )/($a-($yrel+$yshift)*$yscale))*atan(($a-($yrel+$yshift)*$yscale)
   /($b-($zrel+$zshift)*$zscale))-((-$b-($zrel+$zshift)*$zscale)/(
   $a-($yrel+$yshift)*$yscale))*atan(($a-($yrel+$yshift)*$yscale)/(
   -$b-($zrel+$zshift)*$zscale))
  }]
  set T2 [expr {
    0.5*log((pow(($b-($zrel+$zshift)*$zscale),2) + pow((-$a-($yrel+
```

```
 $yshift)*$yscale),2))/(pow((-$b-($zrel+$zshift)*$zscale),2) + pow
 ((-$a-($yrel+$yshift)*$yscale),2))) + (($b-($zrel+$zshift)
 *$zscale)/(-$a-($yrel+$yshift)*$yscale))*atan((-$a-($yrel+$yshift
 )*$yscale)/($b-($zrel+$zshift)*$zscale))-((-$b-($zrel+$zshift)
 *$zscale)/(-$a-($yrel+$yshift)*$yscale))*atan((-$a-($yrel+$yshift
 )*$yscale)/(-$b-($zrel+$zshift)*$zscale))
}]
set Hy [expr {
  $C1*(($a-($yrel+$yshift))*$T1 + ($a+($yrel+$yshift))*$T2)
}]

set T3 [expr {
  0.5*log((pow(($b-($zrel+$zshift)*$zscale),2) + pow(($a-($yrel+
 $yshift)*$yscale),2))/(pow(($b-($zrel+$zshift)*$zscale),2) + pow
 ((-$a-($yrel+$yshift)*$yscale),2))) + (($a-($yrel+$yshift)
 *$yscale)/($b-($zrel+$zshift)*$zscale))*atan(($b-($zrel+$zshift)
 *$zscale)/($a-($yrel+$yshift)*$yscale))-((-$a-($yrel+$yshift)
 *$yscale)/($b-($zrel+$zshift)*$zscale))*atan(($b-($zrel+$zshift)
 *$zscale)/(-$a-($yrel+$yshift)*$yscale))
}]
set T4 [expr {
  0.5*log((pow((-$b-($zrel+$zshift)*$zscale),2) + pow(($a-($yrel+
 $yshift)*$yscale),2))/(pow((-$b-($zrel+$zshift)*$zscale),2) + pow
 ((-$a-($yrel+$yshift)*$yscale),2))) + (($a-($yrel+$yshift)
 *$yscale)/(-$b-($zrel+$zshift)*$zscale))*atan((-$b-($zrel+$zshift
 )*$zscale)/($a-($yrel+$yshift)*$yscale))-((-$a-($yrel+$yshift)
 *$yscale)/(-$b-($zrel+$zshift)*$zscale))*atan((-$b-($zrel+$zshift
 )*$zscale)/(-$a-($yrel+$yshift)*$yscale))
}]
set Hz [expr {
  -$C1*(($b-($zrel+$zshift))*$T3 + ($b+($zrel+$zshift))*$T4)
}]

set Hx [expr {0}]

if {$yrel < 35e-9} {
 return [list 0 0 0]
}
if {$yrel > 65e-9} {
 return [list 0 0 0]
}

```

```
  return [list $Hx $Hy $Hz]
}

Specify Oxs_ScriptVectorField:Oe_field {
  script field_from_wire
  script_args {rawpt}
  norm 1
  atlas :atlas
}

Specify Oxs_FixedZeeman:Oersted_final {
  field Oe_field
  multiplier 1
}

# External field is in 1G(1mT = 10G) with converstion factor 1e-4/
    mu0.
Specify Oxs_FixedZeeman:Ext_field [subst {
  field {1000 0 0}
  multiplier [expr {1e-4/$mu0}]
}]

Specify Oxs_Demag {}

# Evolver
# Direction of spin torque given by (comp_1:electric field (due to
    current)) cross_prod (comp_2:surface normal).
Specify Xf_ThermSpinXferEvolve:evolve [subst {
  alpha $alpha
  J {Oxs_ScriptScalarField {
    script {J_dist $Jcurr}
    script_args { rawpt }
    atlas :atlas
  } }
  mp {0 -1 0}
  P $Polarization
  Lambda $Lambda
  temperature $Temp
  uniform_seed $seed
  min_timestep $time_steps
}]

```

```
203
204 Specify Oxs_TimeDriver [subst {
205      basename $outname
206      evolver :evolve
207      mesh :mesh
208      Ms { Oxs_AtlasScalarField {
209      atlas :atlas
210      default_value $Ms
211      values {
212        universe 0.0
213      }}}
214      m0 { Oxs_FileVectorField {
215       atlas :atlas
216       file $in_omf
217      }}
218      stopping_time 5e-9
219   }]
220
221 # Spatial current distribution to prevent current flow in voltage
     arms.
222 proc J_dist { Jcurr xrel yrel zrel } {
223     if {$yrel < 35e-9 || $yrel > 65e-9} {
224    return 0
225   }
226   return $Jcurr
227 }
228
229 # Setting the outputs for visualization
230 Destination my_graph mmGraph
231 Destination my_archive mmArchive
232 Destination my_display mmDisp
233
234 # Sending the data to the visuals and saving them.
235 Schedule DataTable my_graph Step 1
236 Schedule DataTable my_archive Stage 1
237 Schedule Oxs_TimeDriver::Magnetization my_archive Stage 1
238 Schedule Oxs_TimeDriver::Magnetization my_display Step 1
```

B.2 Python script to automate simulations

```
# Script to automatically feed the output of one OOMMF simulation into the
# input of another.

import subprocess
import os
import glob

# A function to find the omf magnetisation vector files in a particular folder.
def get_omf(path):
    omf_path = '%s/*.omf' % (path)
    files = glob.glob(omf_path)
    file_no = len(files) - 1
    omf_file = files[file_no]
    omf_file = os.path.basename(omf_file)
    return omf_file

# A function to set the magnitude of current or field applied to the system.
def set_driver_strength(start_val=-300, end_val=325, lower_val=80, higher_val=120, finer_step=5, coarse_step=50):
    up_flag = 1
    step = coarse_step
    x_list = []
    val = start_val
    num_of_cylces = 1
    offset = 25
    while (val <= end_val):
        if (val == end_val):
            up_flag = 0
        if (up_flag == 1):
            if (val >= lower_val and val < higher_val):
                step = finer_step
            else:
                step = coarse_step
        x_list.append(val)
        val = val + offset + step
    val = val-2*step
    if (num_of_cylces == 1):
```

```
37          while (val >= start_val):
38              if (val == start_val):
39                  up_flag = 1
40              if (up_flag == 0):
41                  if (val > -higher_val and val <= -lower_val):
42                      step = finer_step
43                  else:
44                      step = coarse_step
45              x_list.append(val)
46              val = val - step
47
48      driver_amp = [0]
49      for ele in x_list:
50          driver_amp.append(ele*1)
51
52      print(driver_amp)
53
54      return driver_amp
55
56
57  # Directory/path to the oommf install
58  path_oommf = '../oommf.tcl'
59
60  # MIF file name
61  mif_file = 'thermal_CoFeB_4nm_SOT_including_0e_in_plane_1000_0e.mif'
62
63  # Initial name of the magnetization vector file used in the
        simulation, later updated inside the main loop.
64  initial_omf_file = '06_thermal_CoFeB_4nm_with_0e_J0.omf'
65  in_omf = initial_omf_file
66
67  flag = 0
68  # Flag to control init_sim parameter of MIF file.
69  file_order = 1
70  file_order_step = 1
71  driver = 'current'
72  driver_strength = set_driver_strength()
73  index = 0
74
75  while index<=len(driver_strength):
76      ele = driver_strength[index]
77      str_file_order = f'{file_order:.1f}'
```

```
78
79      if (file_order < 10):
80          str_file_order = '00'+str_file_order
81      elif(file_order < 100):
82          str_file_order = '0'+str_file_order
83
84      # Set the output folder for this iteration
85      out_folder = 'output/%s_%s_%s' % (str_file_order,driver,ele)
86      file_order = file_order + file_order_step
87
88      # If folder doesn't already exist, making the folder.
89      if not os.path.exists(out_folder):
90          os.makedirs(out_folder)
91
92      # Preparing the oommf string to use boxsi.
93      oommf_string = 'tclsh' + ' ' + path_oommf + \
94          ' boxsi -parameters "init_sim %s in_omf %s total_current %s
    out_folder %s\" -- %s' % (
95              flag, in_omf, ele, out_folder, mif_file)
96      print(oommf_string)
97      subprocess.call(oommf_string, shell=True)
98
99      # Updating in_omf for next run.
100     in_omf = out_folder + '/' + get_omf(out_folder)
101     flag = 0
102     index = index + 1
103
104 # Killing all apps at the end of the simulation (OPTIONAL)
105 kill_all = 'tclsh %s killoommf all' % (path_oommf)
106 subprocess.call(kill_all, shell = True)
```

B.3 Python script to process simulation outputs

```
# Extracting and processing the outputs of automated OOMMF
    simulation.
import glob
import matplotlib.pyplot as plt
import numpy as np
import csv
import re
import subprocess

# Function to delete redundant files, useful during reruns.
def delete_file(filename):
    delete_command = 'del '+filename
    subprocess.call(delete_command, shell=True)

# Function to clear existing png(image) files, useful during reruns.
def clear_existing_png():
    files = glob.glob('output/**/*.png', recursive=1)
    for file in files:
        delete_file(file)

# Function to obtain magnetization components from text(.odt) file.
def get_mag_components(filename):
    mx = 404
    my = 404
    mz = 404
    try:
        f = open(filename, 'r')
        count = 0
        for line in f:
            if (count == 12):
                splitted = line.split()
                mx = float(splitted[0])
                my = float(splitted[1])
                mz = float(splitted[2])
            count += 1
        f.close()
    except:
        print("Error while getting mag components!")
    return mx, my, mz

```

```
40 # Function to extract the average components within a particular
       region of the simulation world.
41 def extract_averaged_mag_over_region(filename):
42     try:
43         get_average_string = "tclsh ..\oommf.tcl avf2odt -average
       space -normalize 1 \
44                 -region 25e-9 35e-9 0 75e-9 65e-9 4e-9 infile "+
       filename
45         subprocess.call(get_average_string, shell=True)
46         filename = re.sub(".omf", ".odt", filename)
47         mx, my, mz = get_mag_components(filename)
48         delete_file(filename)
49         return mx, my, mz
50     except:
51         print("Error while extracting averaged mag over region!")
52     return 404, 404, 404
53
54 # Function to convert omf file to ppn file which can later be
       converted to image file.
55 def convert_omf_to_ppn(filename):
56     clear_existing_png()
57     try:
58         oommf_command = "tclsh ..\oommf.tcl avf2ppm -config ..\
       color_config_z.def -f infile " + filename
59         subprocess.call(oommf_command, shell=True)
60         return 1
61     except:
62         print("Error while converting omf to ppn!")
63     return 0
64
65 # Function to extract the magnitude of driver(applied current) used
       in simulations.
66 def extract_driver_val(filename, quantity):
67     field_float = 404
68     try:
69         if(quantity == "field"):
70             x = re.search("(?<=_B).*\d", filename)
71         elif(quantity == "current"):
72             x = re.search("(?<=_J).*\d", filename)
73         field_str = filename[x.start():x.end()]
74         field_float = float(field_str)
75     except:
```

```
76          print("Error while extracting driver value!")
77      return field_float
78
79  # Function to extract specific values from the origin output text(.
    odt) file.
80  def readfile(filename, col_no_1, col_no_2, col_no_3, col_no_4):
81      list_1 = []
82      list_2 = []
83      list_3 = []
84      list_4 = []
85      try:
86          f = open(filename, 'r')
87          for line in f:
88              splitted = line.split()
89  #             print('Number of splitted string in line: '+str(len(
    splitted)))
90
91              if (len(splitted) == col_no_1):
92
93                  list_1.append(splitted[col_no_1-1])
94                  list_2.append(splitted[col_no_2-1])
95                  list_3.append(splitted[col_no_3-1])
96                  list_4.append(splitted[col_no_4-1])
97
98          f.close()
99      except:
100         print("Error while reading odt file. Problem in readfile!")
101     if (len(list_1) == 0):
102         print("Adjust the length of splitted! No data was appended
    to the list!")
103     return list_1, list_2, list_3, list_4
104
105 # Function to put all the required data into a single csv file that
    can be processed later.
106 def write_data_to_file(name, quant, time, driver, mx, my, mz,
    mx_centre, my_centre, mz_centre):
107     try:
108         with open(name+'.csv', 'w', newline='') as f:
109             writer = csv.writer(f)
110             if (quant == "field"):
111                 attrib = ['Time[s]', 'Applied Field[Oe]', 'Mx', 'My'
    ,
```

```
112                             'Mz', 'Mx_centre', 'My_centre', 'Mz_centre
    ']
113             else:
114                 attrib = ['Time[s]', 'Applied Current[uA]', 'Mx', '
    My',
115                             'Mz', 'Mx_centre', 'My_centre', 'Mz_centre
    ']
116             writer.writerow(attrib)
117 
118             for i in range(len(time)):
119                 writer.writerow([time[i], driver[i], mx[i], my[i],
120                                 mz[i], mx_centre[i], my_centre[i],
    mz_centre[i]])
121     except:
122         print("Error in write_data_to_file!")
123 
124 
125 def main():
126     driver_strength = []
127     time = []
128     total_time = 0
129     mx = []
130     my = []
131     mz = []
132     mx_centre = []
133     my_centre = []
134     mz_centre = []
135 
136     # Processing omf files
137     files = glob.glob('output\**\*.omf', recursive=1)
138     for file in files:
139         # Extracting average magnetization over the centre region
140         mx_centre_val, my_centre_val, mz_centre_val =
    extract_averaged_mag_over_region(
141             file)
142         mx_centre.append(mx_centre_val)
143         my_centre.append(my_centre_val)
144         mz_centre.append(mz_centre_val)
145 
146         # Making ppn file to convert them to png later
147         convert_omf_to_ppn(file)
148 
```

```
149     # Processing odt files
150     files = glob.glob('output/**/*.odt', recursive=1)
151     for file in files:
152         # Extracting field value
153         driver_strength.append(extract_driver_val(file, "current"))
154 
155         # Extracting time column(23) and magnetization components (
    mx:19,my:20,mz:21) from the entire region
156         lis1, lis2, lis3, lis4 = readfile(file, 23, 19, 20, 21)
157         index = 0
158         while (index < len(lis1)):
159             try:
160                 time_entry = lis1[index]
161                 total_time += float(time_entry)
162                 time.append(total_time)
163 
164                 mx_entry = lis2[index]
165                 mx.append(float(mx_entry))
166 
167                 my_entry = lis3[index]
168                 my.append(float(my_entry))
169 
170                 mz_entry = lis4[index]
171                 mz.append(float(mz_entry))
172 
173                 index += 1
174 
175             except:
176                 print('Error!')
177 
178     # Writing the appropriate data to the data file
179     write_data_to_file(
180         'CoFeB_4nm_SOT_including_Oe_in_plane_1000_Oe_hysteresis_data
    ', "current", time, driver_strength, mx, my, mz, mx_centre,
    my_centre, mz_centre)
181 
182 
183 main()
```